



The
University
Of
Sheffield.

The relationship between leaf cellular architecture and leaf-level photosynthesis

By: Alice L Baillie

A thesis submitted for the degree of
Doctor of Philosophy

The University of Sheffield
Faculty of Science
Department of Animal and Plant Sciences

September 2017

Acknowledgements

Firstly, thanks go to my supervisor Andrew Fleming for his advice and support throughout my PhD.

This project was funded by the Gatsby Charitable Foundation. I am very grateful for this studentship and the associated opportunities to receive training and to present my work. I would like to thank both the Foundation and the Gatsby Plant Science Advisors for this opportunity.

I have worked particularly closely with Sam Amsbury and Sarah Carroll on certain strands of this project and would like to thank them both for being such great team-mates, but more importantly for providing the sort of inspiring, idea-bouncing friendships that make doing science really fun.

I could not have tackled the physiological side of this project without the help of Marj Lundgren, Matt Wilson and Jess Dunn. I am so grateful to them all for their willingness to answer my endless questions.

I have many other people to thank for offering advice, training, plasmids, seeds, and seeds of ideas. In particular, Andrew Mathers and Craig Sturrock at the Houndsfield facility, University of Nottingham, for training me in image analysis, and the Knox lab for providing resources and advice for our antibody labelling work.

I would like to thank all of my colleagues in the lab for making it such an enjoyable place to work. I have also been grateful for the support and encouragement of so many friends from the lab, the department and beyond.

Huge thanks go to David for both moral and technical support, especially during the writing phase. Thanks also to my brother James for kindly proof reading and providing useful feedback.

Last but most certainly not least I would like to thank my parents for their support, encouragement, proofreading and statistical advice. Above all this, I am also grateful to them for nurturing an enquiring mind and sincere love of plants.

Collaborations & publications

Several of the experiments presented in this thesis contributed to larger, collaborative projects.

Some of the embedding and antibody labelling presented in Chapter 2 was conducted in collaboration with Dr Sam Amsbury and contributed to the following publication.

- Amsbury, S. et al., 2016. Report Stomatal Function Requires Pectin De-methylesterification of the Guard Cell Wall. *Current Biology*, 26, pp.1–8.

The molecular cloning work in Chapter 3 (generation and characterisation of pCa1:PMEI) was conducted in collaboration with Dr Sam Amsbury, with assistance from Masters student Aaron Hoyle. The antibody-labelled images of the *qua2* line in the same chapter were produced by Masters student Alexandros Phocas.

Stomatal aperture measurements in Chapters 3 and 4, and aniline blue staining experiments in Chapter 4, were carried out by Sarah Carroll, with whom these experiments were planned jointly.

Atomic force micrographs presented in Chapter 4 were generated by Professor Andrew Fleming. Data presented in this chapter contributed to the following publication.

- Carter, R. et al., 2017. Stiffening Of Guard Cells Report Stomatal Opening Involves Polar, Not Radial, Stiffening Of Guard Cells. *Current Biology*, 27, pp.1–10.

The results presented in Chapter 5 combine data from some plant lines previously measured by Dr Marjorie Lundgren, Alice Mitchell and Dr Radek Pajor with two additional lines, measured by myself using the same protocol. MicroCT data for all lines were analysed afresh. These data will contribute to a manuscript that is currently in preparation. Visual renderings of microCT data in Chapters 3 and 5 were generated by Dr Andrew Mathers at the Hounsfield Facility, University of Nottingham.

Abstract

Plants must obtain CO₂ from the air for photosynthesis. The rate at which CO₂ can reach the sites of fixation in the chloroplasts is determined by conductance through the stomata and underlying mesophyll airspaces. This thesis addresses fundamental questions about how the stomata and mesophyll develop, and how their structural and mechanical properties influence leaf-level photosynthesis. The plant cell wall determines the cellular architecture of the leaf by regulating cell expansion and by determining the strength of adhesion between cells. The guard cell walls are also of particular interest due to their ability to undergo rapid, repeated, reversible shape changes to regulate stomatal aperture. In this thesis, the spatial distribution of cell wall epitopes in *Arabidopsis thaliana* leaf tissue was characterised by immunolabelling. These data pointed to pectic homogalacturonan (HG) as a potential regulator of mesophyll development. A search for HG mutants revealed one lacking demethylesterified HG but with no striking change in cellular architecture. Others with wild-type immunolabelling, but previously reported alterations in pectin quantity, showed significant increases in intercellular airspace. Photosynthesis was affected in opposite ways in different lines, suggesting a complex relationship between HG quality/quantity, leaf development, and physiology. In the stomatal complex a polar deposit of demethylesterified pectin was identified with potential functional significance. Additionally, callose was implicated in stomatal movement by the discovery that callose-deficient stomata are unable to close in response to high CO₂. Finally, the relationship between stomatal density and mesophyll cellular architecture was investigated, and the data equally supported the hypotheses of direct cell-cell coordination, or gas-exchange-driven coordination via functional stomata. These findings provide novel insights into the role of the cell wall in mesophyll development and in guard cell movement. Furthermore, they contribute to our understanding of the relationships between structure and function in leaf tissues.

Table of Contents

Chapter 1	Introduction.....	1
1.1	Stomatal and mesophyll conductance	1
1.2	Stomatal and mesophyll development.....	3
1.3	The cell wall	5
1.3.1	Cellulose and callose.....	5
1.3.2	Hemicellulose	6
1.3.3	Pectins	6
1.3.4	Proteins and glycoproteins.....	8
1.3.5	Summary.....	8
1.4	Aims and hypotheses.....	8
Chapter 2	Characterising leaf cell wall composition in <i>Arabidopsis thaliana</i>	11
2.1	Introduction.....	11
2.1.1	Timing of mesophyll differentiation	11
2.1.2	Control of mesophyll cell separation.....	11
2.1.3	Cell wall epitope detection with monoclonal antibodies.....	12
2.1.4	Aims	12
2.2	Results	14
2.2.1	Hemicelluloses.....	14
2.2.2	Pectins	20
2.2.3	Glycoproteins.....	25
2.2.4	Epitopes found on multiple cell wall component classes.....	26
2.2.5	Changes in cell wall epitope patterns during development.....	29
2.3	Discussion	32
2.3.1	Cell wall components in Arabidopsis leaves.....	32
2.3.2	Cell wall components with a potential role in airspace formation	33
2.3.3	Conclusions.....	34
Chapter 3	Cell wall pectin and mesophyll cellular architecture.....	35
3.1	Introduction.....	35

3.1.1	<i>In muro</i> pectin modification.....	35
3.1.2	Pectin biosynthesis.....	36
3.1.3	Delivery of pectin and pectin-modifying enzymes to the cell wall	37
3.1.4	Aims.....	38
3.2	Results.....	39
3.2.1	Identification and characterisation of leaf-expressed <i>PME</i> genes	39
3.2.2	Generation and characterisation of mesophyll-targeted <i>PMEI</i> overexpression lines	45
3.2.3	Characterisation of <i>quasimodo</i> pectin biosynthesis mutants.....	52
3.2.4	Characterisation of <i>arp3</i> , a putative pectin localisation mutant	64
3.3	Discussion.....	68
3.3.1	Altering <i>PME</i> activity <i>in muro</i>	68
3.3.2	Investigating the mesophyll cellular architecture of cell wall mutants	69
3.3.3	Do changes in the cell wall lead to changes in physiology via an effect on mesophyll cellular architecture?.....	70
3.3.4	Conclusions and future work	72
Chapter 4	The role of the cell wall in stomatal development and function.....	73
4.1	Introduction	73
4.1.1	Stomatal function.....	73
4.1.2	Stomatal cell walls.....	74
4.1.3	Aims.....	75
4.2	Results.....	76
4.2.1	Identifying cell wall components potentially regulating guard cell adhesion	76
4.2.2	Functional consequences of degrading specific cell wall components	80
4.2.3	The role of callose in stomatal tip walls.....	88
4.3	Discussion.....	94
4.3.1	Demethylesterified pectin has multiple functions in the guard cells	94
4.3.2	Callose is localised to guard cell tip walls and is required for stomatal closure.	95
4.3.3	Modelling approaches to understanding stomatal movement	97

4.3.4	Conclusions and future work.....	97
Chapter 5	Coordinating stomatal and mesophyll development.....	99
5.1	Introduction.....	99
5.1.1	Stomatal patterning.....	99
5.1.2	Coordination of stomatal and mesophyll development.....	100
5.1.3	Aims	100
5.2	Results	102
5.2.1	Stomatal density and index	102
5.2.2	Mesophyll porosity and channel distribution.....	102
5.2.3	Light and CO ₂ response.....	112
5.2.4	Relating physiology to structure.....	120
5.3	Discussion	122
5.3.1	Effect of stomatal density on mesophyll patterning	122
5.3.2	Effect of stomatal function on mesophyll patterning and physiology	123
5.3.3	Determination of mesophyll structure.....	123
5.3.4	Conclusions and future work.....	124
Chapter 6	General Discussion	127
6.1	Airspace in the leaf: from form to function.....	127
6.2	Future work	130
Chapter 7	Materials and Methods	133
7.1	Plant material	133
7.2	Plant growth	133
7.2.1	Growth on agar plates	133
7.2.2	Growth on compost.....	134
7.3	Genotyping	134
7.3.1	Extraction of genomic DNA	134
7.3.2	PCR reaction	135
7.3.3	Agarose gel electrophoresis	135
7.4	Generation of tissue-specific PME1 overexpression lines.....	135

7.4.1	Amplification of PME1 coding sequences.....	135
7.4.2	Cloning	135
7.4.3	Promoter swap.....	137
7.4.4	Transformation of agrobacteria.....	137
7.4.5	Plant transformation.....	137
7.4.6	Generation of homozygous lines	138
7.5	Enzymatic degradation of cell walls of intact tissue	138
7.6	Immunohistochemistry.....	138
7.6.1	Fixing, embedding and sectioning	138
7.6.2	Immunolabelling	139
7.6.3	Chemical and enzymatic pre-treatments.....	139
7.6.4	Imaging.....	139
7.7	Stomatal density and index.....	139
7.8	Aniline blue imaging.....	140
7.9	COS ⁴⁸⁸ probe imaging.....	140
7.10	Response of stomatal aperture to CO ₂	140
7.11	Gas exchange/fluorescence measurements.....	141
7.11.1	<i>qua1, qua2, arp3</i> and Col-0.....	141
7.11.2	Stomatal patterning and covering mutants.....	141
7.12	Micro Computed Tomography.....	142
7.12.1	Image capture	142
7.12.2	Image analysis	142
7.13	Atomic Force Microscopy	144
7.14	Statistical Analyses.....	144
	Bibliography	145
	Appendix 1	157

Table of Figures

Figure 1.1: Anatomy of leaf conductance to CO ₂	2
Figure 1.2: Schematic diagram of pectin classes	7
Figure 2.1: LM25 (anti-xyloglucan).....	16
Figure 2.2: LM15 (anti-xyloglucan).....	17
Figure 2.3: LM21 (anti-mannan)	18
Figure 2.4: LM11 (anti-xylan)	19
Figure 2.5: JIM5 and JIM7 (anti-HG).....	22
Figure 2.6: LM18, LM19 and LM20 (anti-HG).....	23
Figure 2.7: LM5 (anti-RG-I).....	24
Figure 2.8: LM14 (anti-AGP).....	26
Figure 2.9: Developmental changes in HG distribution	30
Figure 2.10 Representation of LM19 and LM20 localisation.....	34
Figure 3.1: Graphical representation Arabidopsis <i>PME</i> gene expression.....	41
Figure 3.2: Growth of <i>pme</i> mutants.....	43
Figure 3.3: <i>pme3</i> immunolabelling with anti-HG mAbs.....	44
Figure 3.4: pCA1:: <i>AtPME1</i> construct map	47
Figure 3.5: Growth of pCA1:: <i>PME1</i> lines	49
Figure 3.6: Immunolabelling of pCA1:: <i>PME1</i> lines	51
Figure 3.7: Col-0, <i>qua1</i> , <i>qua2</i> and <i>arp3</i> growth on compost.....	55
Figure 3.8: Porosity of Col-0, <i>arp3</i> , <i>qua1</i> and <i>qua2</i> leaves.....	57
Figure 3.9: Mesophyll surface area exposed to airspace in Col-0, <i>arp3</i> , <i>qua1</i> and <i>qua2</i> leaves	58
Figure 3.10: CO ₂ and light response curves of Col-0, <i>arp3</i> , <i>qua1</i> and <i>qua2</i>	59
Figure 3.11: Stomatal density and index of Col-0, <i>qua1</i> , <i>qua2</i> and <i>arp3</i> leaves	61
Figure 3.12: <i>qua2</i> anti-HG immunolabelling	62
Figure 3.13: <i>arp3</i> CO ₂ response bioassay	66
Figure 3.14: <i>arp3</i> anti-HG immunolabelling	67
Figure 4.1: Key stomatal dimensions	74
Figure 4.2: Labelling stomata with anti-pectin mAbs	78
Figure 4.3: Labelling stomata with anti-hemicellulose mAbs	79
Figure 4.4: Tip walls contain callose.....	80
Figure 4.5: Response to CO ₂ in enzyme-treated stomata	82
Figure 4.6: Changes in cell wall mechanical properties	83
Figure 4.7: PG-treatment of stomata causes separation at poles.....	84
Figure 4.8: Aniline blue staining of enzyme-treated tissue.....	85
Figure 4.9: Immunolabelling of enzyme-treated tissue	86
Figure 4.10: COS ⁴⁸⁸ detects demethylesterified pectin in stomata	87
Figure 4.11: Callose localisation during leaf development	89

Figure 4.12 Effect of dexamethasone induction on aniline blue staining in <i>GSL8-RNAi</i>	92
Figure 4.13: Response to CO ₂ in induced <i>GSL8-RNAi</i> plants	93
Figure 5.1: Stomatal patterning schematic	101
Figure 5.2: Stomatal density and index	105
Figure 5.3: Porosity	107
Figure 5.4: Mesophyll channel size and channel density	109
Figure 5.5: Exposed mesophyll surface area and leaf thickness	110
Figure 5.6: Response of photosynthetic rate to changes in CO ₂ and light	115
Figure 5.7: Modelled light and CO ₂ compensation points	116
Figure 5.8: Relationship between g_{s400} and stomatal density	118
Figure 5.9: Relationship between g_{s400} and palisade porosity	121

Table of Tables

Table 2-1: Summary of antibodies tested on resin-embedded leaf sections for which no binding was observed.....	27
Table 3-1: <i>PME</i> mutant lines in highly leaf-expressed genes, obtained for immunolabelling.....	40
Table 4-1: Antibodies for which no binding was observed in the transverse and paradermal sections of stomata	77
Table 7-1: Primers used during the cloning process.....	136
Table 7-2: Settings used for microCT scanning of Arabidopsis leaf discs	142

List of Abbreviations

A₍₄₀₀₎: Assimilation (at ambient CO₂)

Ab: Abaxial

ABA: Abscisic Acid

Ad: Adaxial

AFM: Atomic Force Microscopy

AGP: Arabinogalactan Protein

ARP: Actin-related Protein

A_{sat}: Assimilation maximum under CO₂ saturation

CAPS buffer: *N*-cyclohexyl-3-aminopropanesulfonic acid buffer

CCP: CO₂ Compensation Point

CGR: Cotton Golgi-related

C_i: Leaf internal CO₂

Col-0: Colombia-0 accession of *Arabidopsis thaliana*

COS⁴⁸⁸: Chitosan Oligosaccharide 488, an anti-HG probe

Dex: Dexamethasone

DMSO: Dimethyl Sulfoxide

E_a: Aparent modulus

EPF: Epidermal Patterning Factor

EPFL: Epidermal Patterning Factor-like

FITC: Fluorescein

focl1: Fused Outer Cuticular Ledge 1

GalA: Galacturonic Acid

GA_{sat}: Gross assimilation maximum under CO₂ saturation

G_{s (400)}: Stomatal conductance (at ambient CO₂)

GSL: Glucan Synthase-like

G_m: Mesophyll conductance

G_{wall}: Conductance through the Cell Wall

HG: Homogalacturonan

LB medium: Lysogeny Broth

LCP: Light Compensation Point

mAb: Monoclonal Antibody

microCT: High resolution x-ray computed tomography

MES: 2-(*N*-morpholino)ethanesulfonic acid

MS salts: Murashige and Skoog salt mixture

NASC: Nottingham Arabidopsis Stock Centre

Oex: Overexpression

Par_{in}: Photosynthetically active radiation reaching leaf

PAE: Pectin Acetylerase

PBS buffer: Phosphate buffer saline

pCA1: Promoter of Carbonic Anhydrase 1 gene

PCR: Polymerase Chain Reaction

PdBG: Plasmodesmatal-localised β-1,3 glucanase

PEM buffer: Pipes, EGTA, MgCl₂ buffer

(also contains NaOH)

PG: Polygalacturonase

PL: Pectate Lyase

PME: Pectin Methylesterase

PMEI: Pectin Methylesterase Inhibitor

PPFD: Photosynthetic photon flux density

QUA: Quasimodo

RG-I/-II: Rhamnogalacturonan-I/-II

RH: Relative Humidity

RNAi: RNA interference

SAM: Shoot Apical Meristem

SD: Stomatal Density

SOC medium: Super optimised broth with
catabolite repression

STOM: Stomagen

TMM: Too Many Mouths

V_{cm}max: Maximum rate of carboxylation

w/v: Weight/volume

XG: Xyloglcan

Chapter 1 Introduction

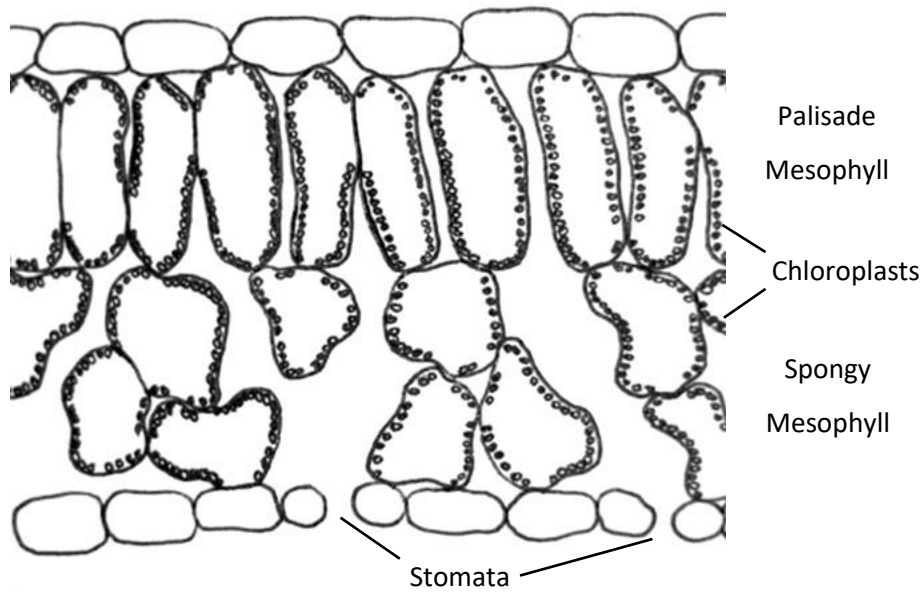
The fundamental relationship between the structure of a leaf and its capacity for photosynthesis is not only a fascinating biological mystery, but one of potential agronomic importance. Increases in crop yields are required to meet global demand for food and fuel, but traits such as partitioning of energy to useable parts of the plant are approaching optimisation. We therefore need to look to other factors limiting yield, such as the biochemical and structural limitations on photosynthetic efficiency, to increase productivity (Zhu et al. 2010). Questions of how to increase plant photosynthesis are complicated by the rapidly changing global environment, making it important to understand how changes in plant traits might affect yield not only under today's ambient conditions but in a higher-CO₂ future. Furthermore, while increases in the rate of photosynthesis offer the potential to translate to an increase in yield, this potential may not be realised depending on how the plant allocates resources.

The body of work described in this thesis aims to advance our understanding of how both the cell wall and the developmental coordination between tissues regulate the 3D pattern of cells and airspaces within leaves. By examining the physiological performance of *Arabidopsis thaliana* plants that vary in their mesophyll cellular architecture, we hope to learn which structural features are most beneficial for efficient photosynthesis. While observations of the specific cell wall components affecting differences in the leaves of the reference plant *Arabidopsis* are unlikely to be applicable to monocotyledonous crop species, the broader conclusions about gas exchange and photosynthesis in leaves may be relevant to a wider range of plants.

1.1 Stomatal and mesophyll conductance

CO₂ faces multiple points of resistance on the journey from the atmosphere to the chloroplast, which altogether result in a ~50% reduction in CO₂ concentration at the sites of photosynthesis in C₃ plants relative to atmospheric levels (**Figure 1.1-A**; Warren, 2008). First the boundary layer of air around the leaf must be crossed, then entry must be gained via a stomatal opening. The resistance posed by the stomata depends on their density and their aperture, both of which are regulated in response to the environment, though on very different timescales. Stomatal density is established during leaf development and modulated by environmental factors including light availability, humidity and CO₂ concentration (Bergmann & Sack 2007). These same factors regulate the apertures of the stomata, which are able to respond rapidly to environmental fluctuations.

A



B

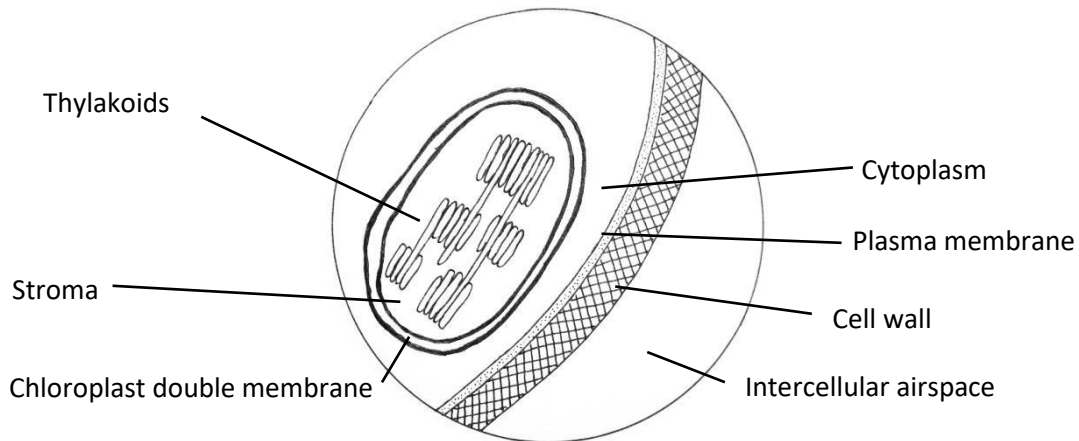


Figure 1.1: Anatomy of leaf conductance to CO₂

(A) Cross-section of a typical dicotyledonous leaf. CO₂ must pass through the stomata and the mesophyll airspaces to reach the site of photosynthesis in the chloroplasts. Stomatal conductance (g_s) and mesophyll conductance (g_m) are partly determined by anatomical features. The mesophyll consists of two cell types: elongated palisade cells, and irregularly shaped spongy cells.

(B) Mesophyll conductance to CO₂ can be divided into multiple sub-conductance components: the intercellular airspaces, the cell wall, the plasma membrane, the cytoplasm, the chloroplast membranes and the stroma.

While the resistance posed by stomata (more commonly referred to as its reciprocal, the stomatal conductance (g_s)) is a popular topic of research, mesophyll conductance (g_m) has received much less attention despite potentially accounting for up to half of photosynthetic limitation under certain conditions (Casson & Hetherington 2010; Griffiths & Helliker 2013). Similarly to g_s , the potential g_m is set during development but some dynamic regulation is also thought to facilitate rapid environmental responses. The structure of the mesophyll tissue and

the extent and pattern of the air channels between the cells, which are established during development, are just some of the physical factors determining the potential g_m . As well as passage of CO_2 through the airways of the leaf, g_m also incorporates conductance through the cell wall (g_{wall}), the plasma membrane, the liquid phase in the cell cytoplasm and the chloroplast membranes and stroma (**Figure 1.1-B**; Warren, 2008). Other physical factors such as the thickness of the cell wall and the proximity of chloroplasts to the plasma membrane will therefore affect g_m . The surface area of mesophyll cells available for CO_2 uptake is a further key structural parameter determining g_m at the leaf level (Evans et al. 2009). Each sub-conductance that accounts for part of g_m is typically expressed per unit area of exposed mesophyll cell wall, and g_{wall} is usually the most limiting of these, though this can vary between species and in relation to environmental conditions (Tomás et al. 2013). Rapid modulation of g_m in response to the environment can be effected by chloroplast movement, by aquaporin-mediated CO_2 diffusion and by the enzymatic activity of carbonic anhydrase enzymes in the cytosol (Terashima et al. 2011; Tholen et al. 2008). It has been suggested that altering g_m rather than g_s might offer a promising route for water-efficient crop improvement (Flexas et al. 2008).

The effect of mesophyll architecture on CO_2 uptake has been the primary focus of this section, but changes in cell packing may also alter the light attenuation properties of the leaf and thereby exert a dual effect on photosynthesis (Terashima et al. 2011; Raven 1996).

1.2 Stomatal and mesophyll development

In contrast to animal cells, which become separated from their siblings by the process of cytokinesis, plant cells divide by the establishment of a new internal cell wall, so cell-cell adhesion is the default state (Smith 2001). However, many plant tissues contain functionally important spaces between cells, and these can arise by a number of mechanisms. Lytic breakdown of cells (lysigeny) is one possibility, and this mechanism is involved in the formation of xylem tissue. Alternatively, spaces can be opened up between live cells by targeted breakdown of the pectic middle lamella layer of the cell wall (schizogeny) or by growth of cell spaces caused by turgor-driven growth of the surrounding cells (expansigeny)(Seago et al. 2005).

In most plant tissues small airspaces can be observed at the intersections between three or more cells, which often appear triangular in cross-section (Knox 1992; Sifton 1945). Some accounts propose that such spaces are established when new cell walls connect to the mother cell walls during cytokinesis (Jeffree et al. 1986). In certain tissues, such as the leaf mesophyll, these airspaces become greatly enlarged, so a mechanism must exist to determine which airspaces open up and which are halted at a small size (Jarvis et al. 2003). Whether an airspace

is expanding or not, the cell walls at its corners are strengthened to prevent uncontrolled cell separation (Jarvis 1998; Parker et al. 2001; Kolloffel & Linssen 1984).

Leaf epidermal tissue is an exception to the tendency for small airspaces at the junctions between cells. The outermost layer of leaf cells provides an important barrier to prevent pathogens from entering the leaf, and to regulate water balance. It is therefore important that epidermal cells adhere tightly to their neighbours. Some connections to the environment are, however, necessary for gas exchange, and the stomata fulfil this function. Stomata comprise a pair of guard cells that are able to change their size and shape in response to environmental cues, regulating the size of the stomatal pore. Stomata arise by the symmetrical division of a guard mother cell (see also Chapter 5), and the (presumably schizogenous) separation of a portion of that new cell boundary to form the pore. This is the only region of cell separation within the epidermis, and must be tightly regulated to prevent the guard cell pairs from separating excessively.

Cell separation in the inner mesophyll tissues of the leaf is very extensive, in contrast to the situation in the epidermis, and seems likely to arise by a combination of schizogeny and expansigeny. The resulting air channels are essential for efficient diffusion of CO₂ from the substomatal cavities to the sites of photosynthesis, which primarily occurs in the upper, palisade mesophyll layer, although stomata are also found on the adaxial leaf surface at slightly lower density. Greater porosity in the lower, spongy mesophyll layer is due to earlier cessation of cell division, greater levels of cell separation, and distinctly anisotropic growth of cells to generate irregular forms (Sifton 1945). Understanding the differentiation of these distinct layers of leaf mesophyll is a complex problem because many levels of regulation are involved.

Leaf development is responsive to environmental inputs such as light level and CO₂ availability, and also requires coordination of growth between different tissue layers (Tsukaya 2005; Teng et al. 2006). Some studies have suggested that epidermal growth regulates the expansion and division of other cells within the leaf (Savaldi-Goldstein et al. 2007). Furthermore, determination of leaf size is surprisingly robust, and mutants in which cell growth or division are affected can still produce leaves of a normal size by matching the other of these two parameters to compensate for the impaired function (Tsukaya 2006). On a finer scale, coordination of particular cell types is also necessary, such as patterning stomata to connect to their underlying airspaces. Such integration of endogenous and environmental cues is bound to be complex, and may involve feedback loops mediated by biomechanics, phytohormones, physiology and metabolism. Mutants with disrupted cytokinin responses, for example, have been found to have reduced levels of intercellular adhesion (Jarvis et al. 2003), as do mutants

in the *RE6* gene, which is thought to be involved in amino acid biosynthesis. The mechanisms by which these factors alter cellular organisation are still uncertain.

The pronounced differences in cellular architecture between the abaxial and adaxial halves of the leaf also suggest that transcriptional control is likely to influence mesophyll patterning. Many transcription factors have been identified that confer ab/adaxial identity. The juxtaposition of cells with these distinct identities is required for the development of a planar leaf structure, so mutants in these genes are severely compromised in their leaf development and therefore do not offer an easy way to manipulate and compare different mesophyll architectures (Braybrook & Kuhlemeier 2010; Efroni et al. 2010; Fleming 2005). Downstream of these transcription factors, the cell cycle directly regulates cellular architecture in plant tissues by modulating cell division and expansion (De Veylder et al. 2007). A role for the cell cycle regulator *RBR* in determining mesophyll structure has previously been reported (Dorca-Fornell et al. 2013). Recent work provided further evidence for cell cycle-based regulation of mesophyll development, but also highlighted the complexity of this relationship (Lehmeier et al. 2017).

Ultimately, the physical target of all of these regulatory processes must be the cell wall, which is discussed in greater detail in the next section.

1.3 The cell wall

The cell wall clearly has a direct effect on the development of mesophyll structure, and on the development and function of the guard cells. New cell walls are a prerequisite for cell division, which determines the number of cells that make up a tissue. The middle lamella layer of the wall is thought to be the main point of adhesion between cells and must therefore be altered to allow cell separation in the mesophyll tissues and at the stomatal pore. Furthermore, the mechanical properties of the cell wall are strongly related to its molecular composition. Changes in the epitopes present in the wall can regulate turgor-driven cell growth, and modulate the ability of guard cells to flex and alter the stomatal aperture in response to environmental stimuli. Localised changes in the walls of a given cell can also cause anisotropic growth, allowing irregular cell shapes, such as those of spongy mesophyll, to be obtained. The major constituents of the cell wall are detailed below.

1.3.1 Cellulose and callose

Cellulose and callose are both structural cell wall polymers that are synthesised at the plasma membrane and are composed of β -1,4-linked and β -1,3-linked glucan respectively (Schneider et al. 2016). Callose is deposited in cell plates as they form, and can be detected in the new cell

walls of dividing tissue. Soon after cytokinesis is complete the callose is replaced by cellulose, which is the predominant load-bearing component of mature cell walls. Callose is also associated with stress responses, and is involved in regulating the aperture of the plasmodesmatal channels that provide connectivity between cells (Tilsner et al. 2016). Cellulose is organised into bundles called microfibrils which form arrays throughout the cell walls and provide mechanical strength. The directional alignment of microfibrils determines the direction of cell growth. Linkages between cellulose microfibrils, which are mediated by other cell wall components (below), must be loosened to permit turgor-driven cell growth (Braybrook & Jonsson 2016; Cosgrove 2014). Expansin proteins and cell wall acidification have both been implicated in this process.

1.3.2 Hemicellulose

The hemicelluloses are a diverse group of polysaccharides that all have β -(1,4)-linked backbones and are synthesised by glycosyltransferases in the golgi membranes (Scheller & Ulvskov 2010). Xyloglucan is the most abundant hemicellulose in dicotyledon primary cell walls, whereas xylan is the predominant non-cellulosic component of secondary walls. Mannans may be found in both primary and secondary walls. Hemicelluloses, along with pectins (below) form the cell wall matrix which interconnects the cellulose microfibrils. It has long been assumed that they achieve stabilisation of cellulose through direct, non-covalent interactions, but recent evidence is beginning to uncover a more complex network arrangement with fewer cellulose-xyloglucan and more xyloglucan-pectin interactions than previously thought (Cosgrove 2014). Several research groups have provided evidence that hemicellulose-deficient mutants in Arabidopsis are dwarfed yet viable, providing further evidence that other wall components, most likely pectins, must perform some of the same essential functions (Braybrook & Jonsson 2016).

1.3.3 Pectins

Pectins are arguably the most complex group of cell wall molecules, varying in their backbone structures and bearing a wide array of different side groups, many of which exhibit considerable structural complexity. Pectin regions are categorised into four main sub-classes: homogalacturonan (HG), rhamnogalacturonan-I (RG-I), rhamnogalacturonan –II (RG-II) and xylogalacturonan (XG)(**Figure 1.2**; Harholt, Suttangkakul, & Vibe Scheller, 2010). Like hemicelluloses, these polymers are synthesised in the golgi, and all but RG-I have a backbone of α -(1,4)-linked galacturonic acid residues. In HG, the simplest and most abundant form of pectin in Arabidopsis, this backbone may be methylesterified and/or acetylated. In XG, the backbone additionally carries xylosyl residues and in RG-II many different side-chains can be found. Both of these are minor cell wall constituents. RG-I differs from the other pectin classes

because the backbone consists of alternating galacturonic acid and rhamnose residues. RG-I bears side-groups of arabinose and/or galactose residues, and accounts for 20-35% of cell wall pectin (Mohnen 2008).

HG is not only the most abundant pectin but the best characterised. The mechanical properties that HG confers upon the cell wall depend on the extent and pattern of methylesterification. HG is delivered to the cell wall in a highly methylesterified form and can be demethylesterified by pectin methyl esterase (PME) enzymes. A certain degree of demethylesterification facilitates cross-linking between pectin chains by calcium ions, which rigidifies the wall, but if sufficiently large stretches of demethylesterified HG are available then the wall becomes susceptible to pectin-degrading enzymes (Palin & Geitmann 2012). Modulation of wall stiffness by the action of PMEs is important for cell growth, for example in the context of emergence of primordia from the apical meristem (Peaucelle et al. 2008). Furthermore, a mechanism involving pectic HG in the middle lamella layer of the cell wall is the most commonly considered explanation for cell-cell adhesion, and has been evidenced by observations of cell separation following degradation of pectin (Daher & Braybrook 2015; Knox 1992).

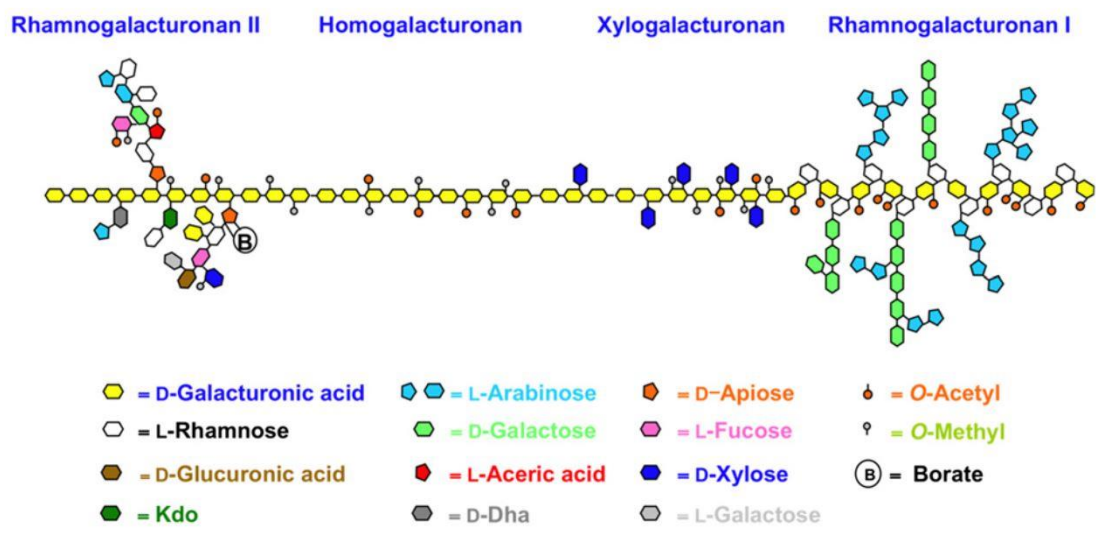


Figure 1.2: Schematic diagram of pectin classes

Pectins are classified into four main classes according to their backbone structure and side-chain composition.

Figure from Harholt, Suttangkakul, & Vibe Scheller (2010)

1.3.4 Proteins and glycoproteins

In addition to the main carbohydrate cell wall constituents described above, cell walls also contain both enzymes and structural proteins, some of which carry carbohydrate attachments (Showalter 1993). The extensins are a particularly notable group due to their role in cell growth, and the arabinogalactan proteins are a large, diverse family of molecules that have sometimes been implicated in cell adhesion, although the mechanism remains to be elucidated (Ellis et al. 2010; Seifert & Roberts 2007).

1.3.5 Summary

In summary, the plant cell wall is a complex structure composed of a very wide variety of carbohydrate and protein components. Furthermore, it is a dynamic structure, constantly being remodelled by enzymes and by biomechanical forces to allow it to fulfil its diverse functions, many of which contribute to plant development.

1.4 Aims and hypotheses

One of the ongoing themes of research in our group is trying to understand the relationship between leaf structure and physiological function. Work to date has primarily involved the manipulation of the cell cycle (Lehmeier et al. 2017) but here we focus instead on the role of the cell wall in the development of both the stomata and the mesophyll, and on the developmental coordination between these tissues. Progress in understanding leaf structure-function relationships has until recently been limited by the lack of suitable techniques for efficiently and accurately characterising the complex, 3D structure of the mesophyll tissue and of the airspaces between mesophyll cells. Traditionally, histological approaches have been used to examine the structure in 2D, but recent work demonstrates that a very large sample size is required to obtain an accurate picture of tissue structure by this method (Theroux-Rancourt et al. 2017). Other early methods included weighing leaves before and after infiltration with water, and making resin casts of the internal airspaces, but neither of these has been very widely used (Smith & Heuer 1981; Mauseth & Fujii 1994). Investigation of the 3D mesophyll structure has recently become more feasible due to advances in imaging equipment and preparation methods, for example improved protocols for deep leaf imaging by confocal microscopy, and the application of high resolution x-ray computed tomography (microCT) to plant tissues (Wuyts et al. 2010; Pajor et al. 2013).

Our approach in this project began with the screening of leaf tissue sections with a collection of monoclonal antibodies (mAbs) to identify cell wall components that might be involved in the formation of the mesophyll and stomata, and in particular those with a likely role in cell adhesion or separation. Based on this information we obtained and generated a range of

mutant lines that we expected to be affected in their mesophyll and/or stomatal development due to cell wall changes. Additionally, we obtained lines that varied in their stomatal patterning or in the functionality of their stomata, which we expected also to be affected in their mesophyll structure. We characterised both the cell wall mutants and the stomatal pattern/function mutants by microCT imaging, which provided detailed information on the amount and distribution of airspace in the leaves, and we paired the collection of these structural measurements with established techniques for analysing leaf-level photosynthesis using the LICOR gas exchange/fluorescence system.

Using these approaches, the following hypotheses were tested:

1. Different cell wall epitopes are associated with adhered and separated walls in the Arabidopsis leaf (Chapter 2)
2. Genetically altering composition of leaf cell walls, particularly with respect to those epitopes specifically associated with adhered or separated walls, will generate lines that differ from the wildtype in their mesophyll cellular architecture (Chapter 3)
3. Genetically altering the cell walls of stomata will alter their development and/or function (Chapter 4)
4. Lines that vary in their stomatal patterning will also vary in their mesophyll cellular architecture (Chapter 5)
5. Lines that vary in their leaf cellular architecture will also vary in their photosynthetic properties (Chapters 3 and 5)

Chapter 2 **Characterising leaf cell wall composition in *Arabidopsis thaliana***

2.1 Introduction

Monoclonal antibodies (mAbs) provide a useful tool for investigating the abundance and distribution of specific molecular structures within the cell walls of plants (Knox 2008). In this chapter we exploit a wide selection of mAbs to characterise the spatial patterning of major cell wall components within the *Arabidopsis* leaf. We focus in particular on identifying components with a localisation pattern that might suggest a role in differential adhesion and separation of cells. Our ultimate aim was to investigate the relationship between leaf cellular structure and physiology by obtaining a panel of cell wall mutants that vary in their mesophyll structure. Identifying cell wall components that might be involved in adhesion between cells was therefore important to assist in the selection of genes to target for manipulation.

2.1.1 Timing of mesophyll differentiation

New leaves initiate on the flanks of the shoot apical meristem (SAM). This outgrowth of new primordia is facilitated by changes in the properties of pectic homogalacturonan (HG), which are effected by enzymes (Peaucelle et al. 2008). For the first 24-48 hours after initiation of a new primordium, all cells are rapidly dividing and are histologically equivalent, but division ceases, starting from the tip, when the leaf has reached about 10% of its final size, and expansion growth takes over (Efroni et al. 2010). One challenge for defining the developmental timing of events such as initiation of airspace formation is that the rate of plant growth and development varies drastically depending on the growth conditions. One way to circumvent this problem is to define developmental events relative to one another, providing that a robust sequence of events can be demonstrated. This might involve transcriptional or anatomical markers (Efroni et al. 2008). For example, Scarpella, Francis, & Berleth (2004) reported that the timing of mesophyll differentiation, as defined by a set of changes in cell shape along with the appearance of airspaces, is strictly coordinated with the termination of procambial domain extension.

2.1.2 Control of mesophyll cell separation

Airspaces in leaves most likely form by a combination of schizogeny (breakdown of the middle lamella) and expansigeny (airspace expansion due to cell growth) (Seago et al. 2005).

Schizogeny is an active process requiring the localised delivery of wall-degrading enzymes to the middle lamella, while expansigeny relies on turgor-driven growth to extend both adhered and separated cell walls, or to physically pull adhered walls apart. It is thought that expansigeny is involved in the initial opening of small airspaces in young tissue, but that reinforcing zones develop to provide strength to the cell wall at airspace corners, thereby limiting the extent of turgor-driven cell separation (Jarvis et al. 2003). It therefore seems likely that adhered walls, separated walls, and reinforcing zones might all be characterised by the localisation of specific cell wall epitopes. Previous studies in stem sections have found such differences, for example the association of some pectic HG epitopes with walls lining airspaces, and the localisation of other subtly different HG epitopes to the reinforcing zones (Verhertbruggen et al. 2009; Willats et al. 2001). However, leaf tissues have been little studied, perhaps due to their complex nature and irregular cell shapes.

2.1.3 Cell wall epitope detection with monoclonal antibodies

Specific cell wall epitopes can be detected using monoclonal antibodies (mAbs). These probes allow quantification of components in cell wall extracts, and can also be applied to thin sections of tissue to observe the spatial distribution of cell wall components. Typically a primary mAb with a known binding specificity is incubated with the sample, and then a secondary mAb, conjugated with a fluorophore, is added to bind to the primary mAb and facilitate visualisation by fluorescence microscopy. Alternatively secondary mAbs conjugated with gold particles can be used to allow imaging by transmission electron microscopy to acquire higher resolution information about epitope localisation. All of the mAbs in this chapter recognise carbohydrate epitopes, but anti-protein mAbs also exist for certain cell wall components, such as the lysine-rich classical arabinogalactan proteins (AGPs) (Yang et al. 2011). While a number of mAbs have previously been used to quantify the cell wall components in *Arabidopsis* leaf cell wall extracts (Zabackis et al. 1995), and a few have been used to label *Arabidopsis* stem sections, the spatial distributions of most mAbs have not been reported in *Arabidopsis* leaf tissues.

2.1.4 Aims

We screened a wide range of mAbs against young and mature resin-embedded Col-0 *Arabidopsis* leaf sections with the aim of identifying epitopes differentially localised in adhered and separated walls. For mAbs with interesting patterns of localisation, more developmental time points were examined, focussing in particular on the earliest stages of leaf development. We hypothesised that adhered regions of cell wall would differ in their epitope composition from walls bordering mesophyll airspace due to differential deposition of material, differential *in muro* modification, or both.

2.2 Results

2.2.1 Hemicelluloses

Hemicelluloses are found in the primary wall and the middle lamella and have traditionally been considered as the primary cross-linkers between cellulose microfibrils (Scheller & Ulvskov 2010; Cosgrove 2014). The presence of hemicellulose epitopes is often partially masked by pectins, which physically block the anti-hemicellulose mAbs from accessing and binding their targets (Marcus et al. 2008). We tested anti-hemicellulose mAbs, both on untreated sections and on sections treated with pectate lyase (PL) to remove the pectin and prevent masking. Sections incubated in the buffer (CAPS) without the enzyme were also labelled as a control. As pectate lyase is only effective in degrading demethylesterified pectin, sections were first treated with Na_2CO_3 to remove methyl groups: samples were labelled after only this first step of the pre-treatment as a further control.

2.2.1.1 Xyloglucan

The LM15, LM24 and LM25 mAbs bind to xyloglucans, which are the most abundant of the hemicelluloses in *Arabidopsis* (Marcus et al. 2008). We observed no binding of LM24 to sections of mature or young leaves. Pre-treated sections of mature leaf also gave no LM24 signal (data not shown). LM25 binding produced a faint signal in the epidermis and vasculature of untreated sections of mature and young leaves (**Figure 2.1**; young leaf data not shown). This epitope was partially unmasked by Na_2CO_3 treatment, and was revealed throughout the walls by PL treatment. A previously published experiment in tobacco stem pith parenchyma sections, pre-treated with PL, found that the LM25 mAb lined intercellular spaces whereas LM24 bound more strongly to adhered walls (Pedersen et al. 2012). However, in the *Arabidopsis* leaf we observed no such association of these epitopes with differential adhesion and separation of cells.

LM15 bound only very weakly to our untreated sections of mature and young leaves (young leaf data not shown), but PL treatment of mature leaf sections revealed a little more binding throughout the walls, especially in the epidermis (**Figure 2.2**). The other pre-treatments made no difference to the signal intensity compared to the untreated sections. This mAb has a different specificity to LM24 and LM25, which may explain the weaker signal that we observed (Pedersen et al. 2012). Similarly to LM24 and LM25, LM15 has previously been associated with key adhesion points in the stem tissues of a number of species, but we observed no specific binding to airspace corners in the *Arabidopsis* mesophyll (Marcus et al. 2008).

2.2.1.2 Mannan

Mannans may be found in both primary and secondary walls of angiosperms and have proposed roles in structure and storage. We tested two anti-mannan mAbs that have previously been shown to bind to the cell walls of Arabidopsis stems (Marcus et al. 2010). In the leaf, LM21 bound to untreated leaf sections in a punctate pattern, and signal was not always associated with cell walls, possibly indicating detection in the endomembrane system. This pattern was consistent between mature and young leaves (**Figure 2.3**; young leaf data not shown). PL pre-treatment revealed LM21 binding throughout the walls, mostly at low intensity but with some very bright areas of signal. The other pre-treatments were comparable to untreated sections. The unmasking by PL was consistent with the strong increase in signal intensity previously observed by Marcus et al. (2010) following PL treatment of stem sections. We did not, however, detect LM22 binding in mature or young leaves, or in any of the pre-treated sections (data not shown).

2.2.1.3 Xylan

Binding of the anti-xylan mAbs LM10 and LM11 was very specific to the vasculature. LM11 is able to recognise a broader range of epitopes, and binding of this mAb was the most consistent, observed in mature and young leaf sections (**Figure 2.4**; young leaf data not shown). LM10 binding varied between replicates at both leaf stages (data not shown). These results are consistent with known xylan abundance only in secondary walls of dicotyledons, and with labelling experiments in Arabidopsis stem, in which both mAbs were found to bind to the vasculature (McCartney et al. 2005).

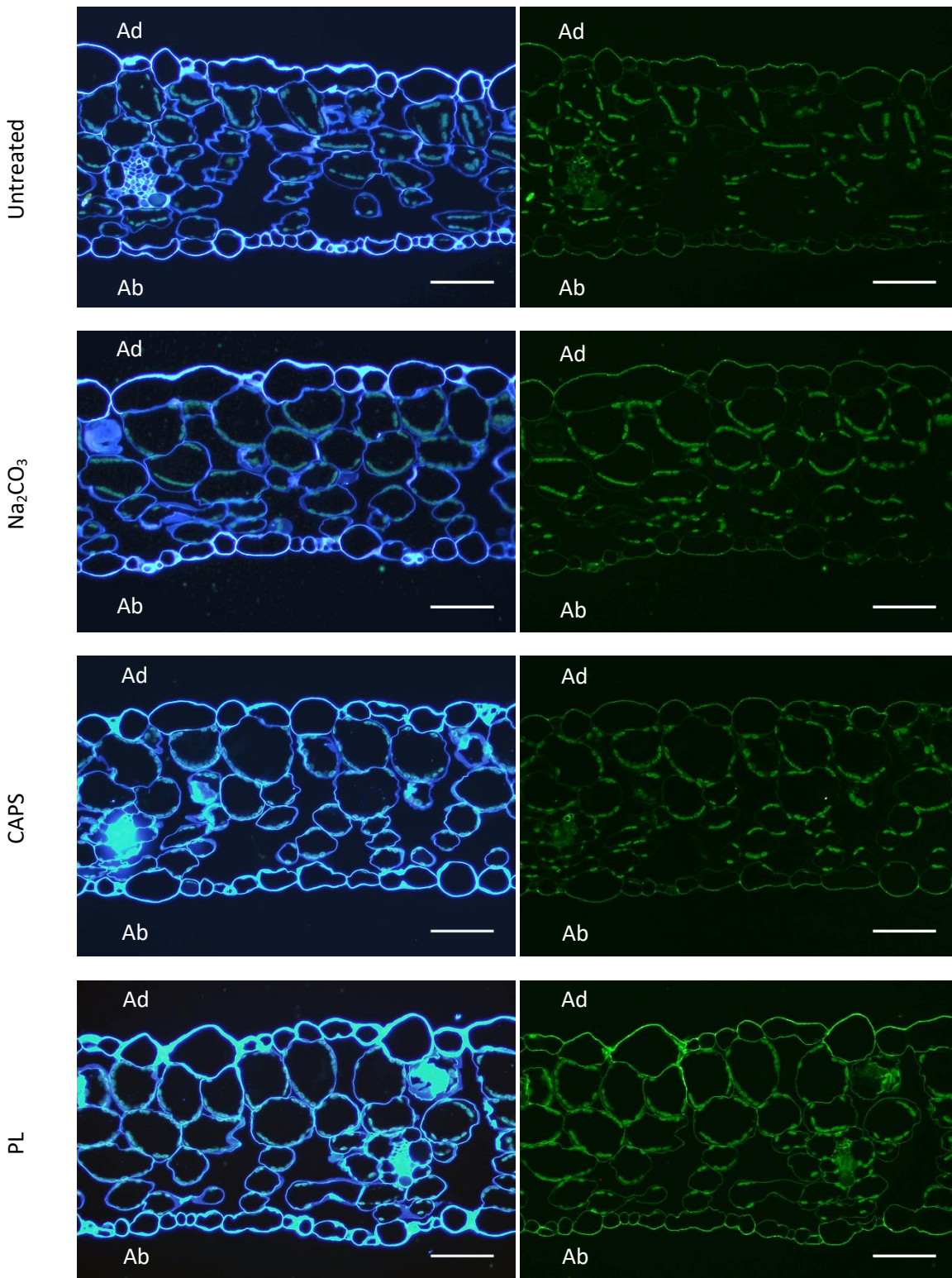


Figure 2.1: LM25 (anti-xyloglucan)

The LM25 mAb recognises a xyloglucan epitope. We observed very faint signal in the epidermis and vasculature of untreated control sections, and slightly more intense signal following Na_2CO_3 pre-treatment. The CAPS buffer caused no change relative to the Na_2CO_3 treatment, but pectate lyase (PL) in CAPS buffer unmasked the LM25 epitope throughout the cell walls. Blue images (left hand side) are calcofluor stained. Green images (right hand side) show the secondary mAb signal in the same region of the section. Controls with no primary mAb showed no secondary mAb signal. Scale bars represent $50\mu\text{m}$. Ab = Abaxial, Ad = Adaxial.

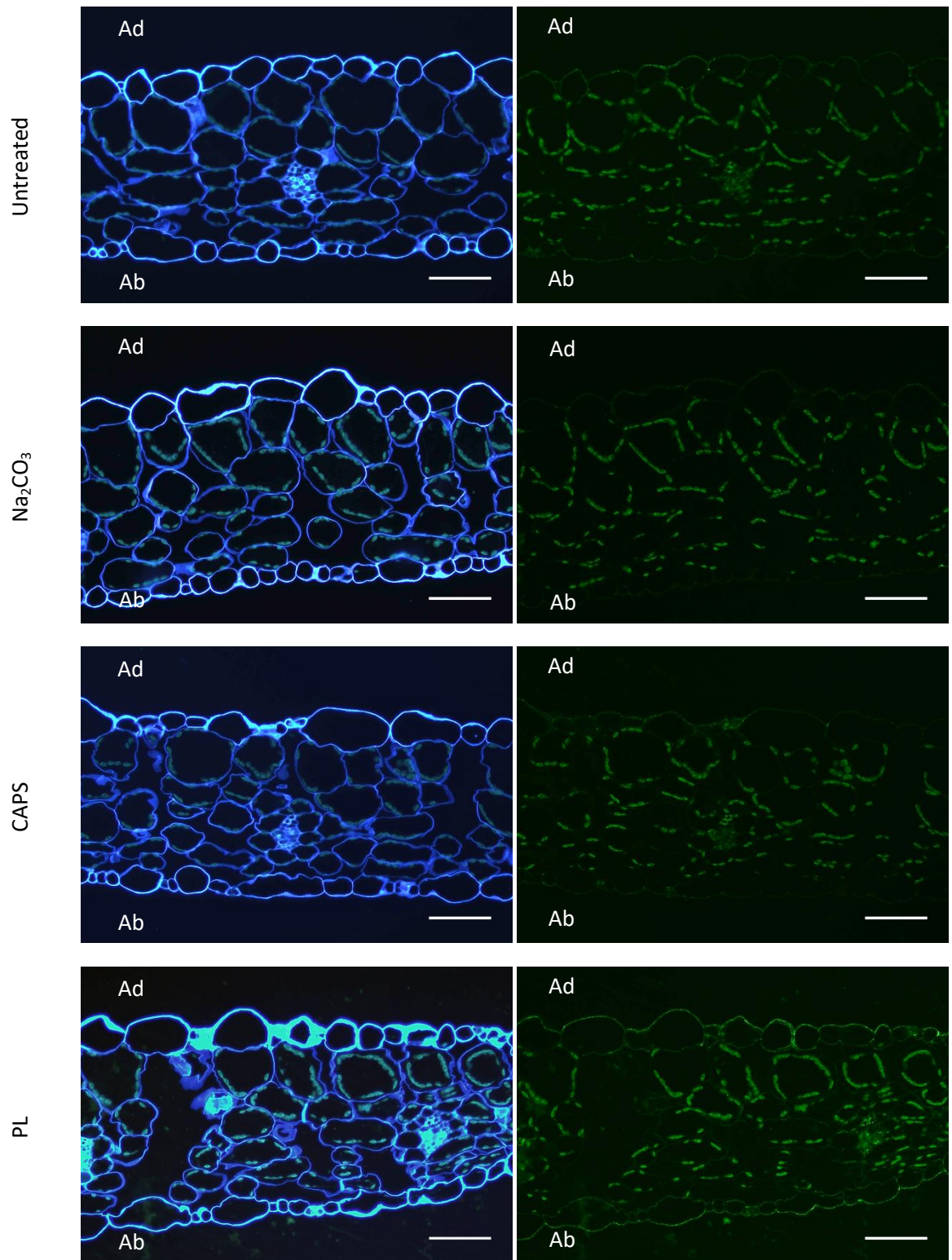


Figure 2.2: LM15 (anti-xyloglucan)

The LM15 mAb recognises a xyloglucan epitope. We observed very faint signal in untreated, Na_2CO_3 and CAPS buffer-treated sections. Pectatate lyase (PL) pre-treatment resulted in a slightly stronger signal, especially in the epidermis.

Blue images (left hand side) are calcofluor stained. Green images (right hand side) show the secondary mAb signal in the same region of the section Controls with no primary mAb showed no secondary mAb signal. Scale bars represent $50\mu\text{m}$. Ab = Abaxial, Ad = Adaxial.

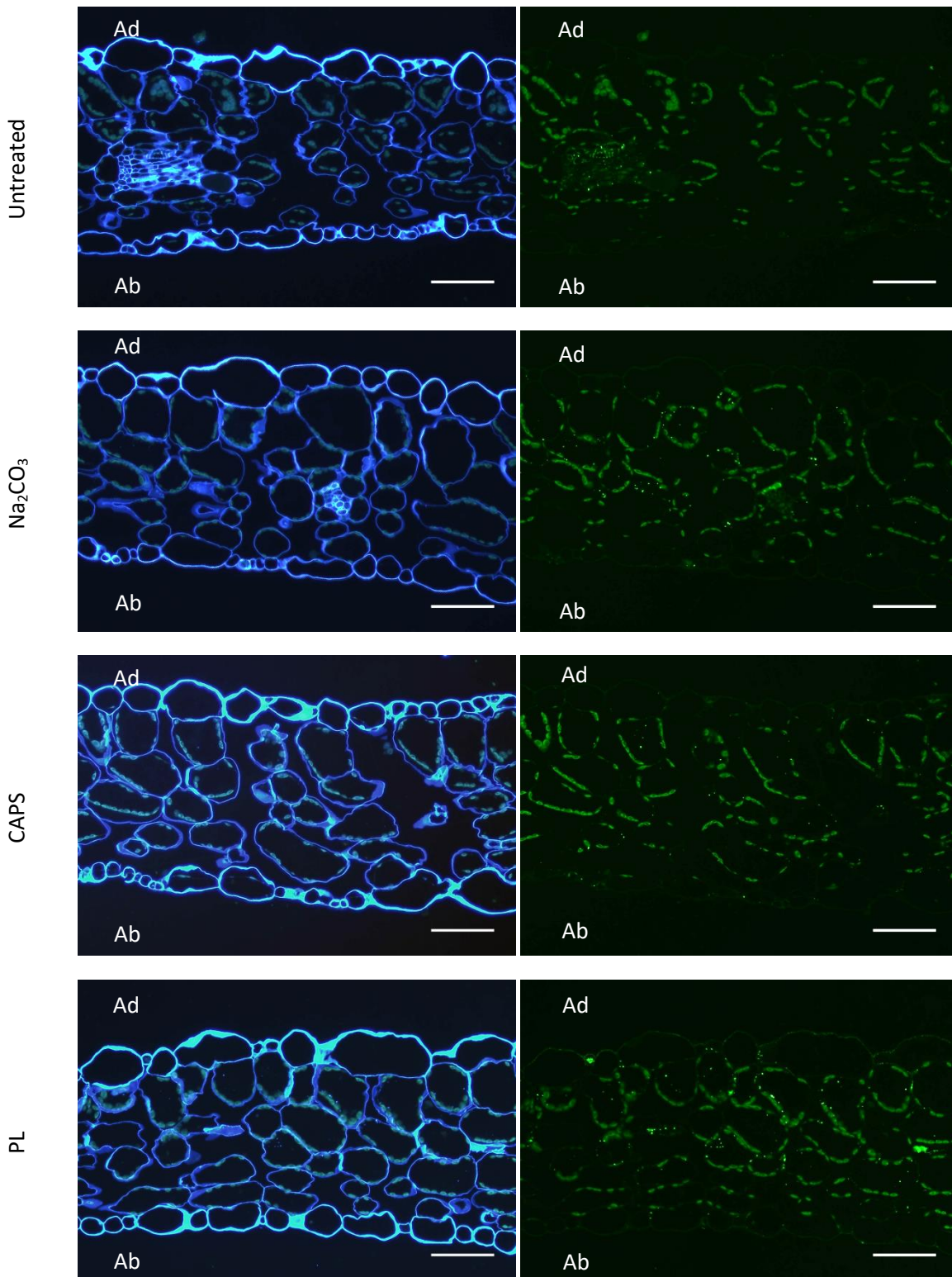


Figure 2.3: LM21 (anti-mannan)

The LM21 mAb binds a mannan epitope. We observed sparse, punctate signal, not exclusively in the cell walls, in untreated, Na_2CO_3 and CAPS-treated sections. Pectate lyase (PL) pre-treatment revealed additional LM21 signal throughout the cell walls.

Blue images (left hand side) are calcofluor stained. Green images (right hand side) show the secondary mAb signal in the same region of the section. Controls with no primary mAb showed no secondary mAb signal. Scale bars represent $50\mu\text{m}$. Ab = Abaxial, Ad = Adaxial.

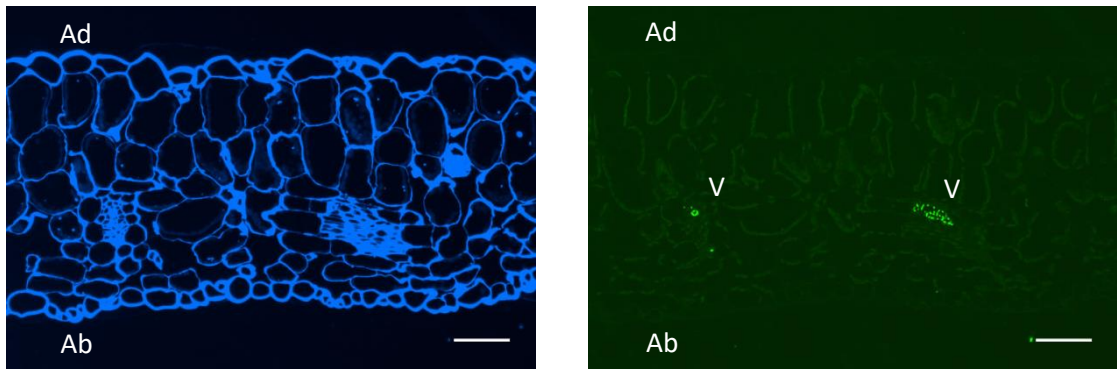


Figure 2.4: LM11 (anti-xylan)

The LM11 mAb binds a xylan epitope. Signal linked to LM11 was observed exclusively in the vasculature.

The blue image (left hand side) is calcofluor stained. The green image (right hand side) shows the secondary mAb signal in the same region of the section. Controls with no primary mAb showed no secondary mAb signal. Scale bars represent 50µm. Ab = Abaxial, Ad = Adaxial, V = Vasculature.

2.2.2 Pectins

As the main component of the middle lamella, and given previous reports of roles in cell adhesion and control of cell expansion, pectins were a strong candidate for a role in mesophyll airspace formation (Daher & Braybrook 2015).

2.2.2.1 Homogalacturonan

Homogalacturonan (HG) accounts for approximately 65% of pectin in most dicotyledons (Mohnen 2008). The HG backbone consists of (1,4)-linked galacturonic acid residues, and can be substituted with acetyl or methylester side-groups. Newly synthesised HG is heavily methylesterified, but these methylester groups can be removed *in muro* by the action of pectin methyl esterase (PME) enzymes. A number of anti-HG mAbs are available that recognise slightly different forms of HG with differing extents and patterns of demethylesterification.

The JIM5 and JIM7 mAbs were raised against carrot tissue and bind HG epitopes with differing degrees of methylesterification (Knox et al. 1990). JIM5 is able to bind epitopes with a lower degree of methylesterification than those recognised by JIM7. We found JIM5 binding was variable between our samples. In most cases punctate signal was observed in cell walls of mature and young leaf sections, and in some cases the epitope appeared to be associated with the vasculature. In contrast JIM7 signal was consistently strong throughout the cell walls of leaves of both ages, with perhaps slightly stronger signal associated with adhered cell walls (**Figure 2.5**).

The JIM5 and JIM7 mAbs have since been largely superseded by more recently developed LM18, LM19 and LM20 (Verhertbruggen et al. 2009). Among these mAbs LM20 requires the greatest degree of methylesterification for binding and LM18 the least, while LM19 binds a somewhat broader range of epitopes than the others. In our mature and young leaf samples the epitopes recognised by all three of these mAbs were apparent to some degree throughout the cell walls (**Figure 2.6**; young leaf data not shown). The brightest LM20 signal was at cell junctions, whereas the brightest LM19 signal was in adhered cell walls. The pattern of LM18 signal was similar to that of LM19 but at lower intensity. This stronger signal intensity in adhered walls is unlikely to be due simply to increased wall thickness since an equivalent increase in calcofluor signal is not observed. These data perhaps suggest a role for demethylesterified HG, detected by LM19, in cell-cell adhesion within the mesophyll. LM20 may be localised to cell junctions due to an active role in cell separation, or conversely, to limit the further separation of cells. Verhertbruggen et al. (2009) labelled tobacco stem pith parenchyma with these three mAbs and reported that both LM19 and LM20 gave the strongest signal in walls bordering airspaces, while LM18 was not detected unless sections

were subjected to alkaline pre-treatment to remove methylester groups, thus artificially generating the LM18 epitope.

We also labelled sections with the 2F4 mAb, which is specific to calcium-crosslinked HG (Liners et al. 1989). Despite previous detection of this epitope by 2F4 in Arabidopsis inflorescence meristems, we observed no binding in leaf sections (Peaucelle et al. 2008; data not shown).

2.2.2.2 Xylogalacturonan

We found no evidence for xylogalacturonan in the Arabidopsis leaf, as reported by the LM8 antibody. LM8 binds to highly xylose-substituted regions of pectin, although the epitope structures that it recognises have not been precisely characterised (Willats et al. 2004). The epitope detected by LM8 has previously been associated with cell separation in a wide range of angiosperm species including in Arabidopsis root caps, but always in the context of cells bound for complete detachment, unlike the leaf mesophyll cells which only partially detach.

2.2.2.3 Rhamnogalacturonan-I

Rhamnogalacturonan I (RG-I) is a more complex polysaccharide than HG, with a backbone of alternating galacturonic acid and rhamnose residues, and variable side chains composed of arabinose and galactose. We observed no binding of LM9, which recognises feruloylated (1,4)- β -D-galactan, or of LM6, LM13 or LM16, which recognise arabinan epitopes (Willats et al. 1998; Clausen et al. 2004; Verhertbruggen et al. 2009; data not shown).

LM5, which binds (1,4)- β -D-galactan, was the only anti-RG-I mAb to bind to mature or young leaf sections, and showed an intriguing binding pattern. Some LM5 signal was observed throughout the cell walls, but strongest signal was in the anticlinal walls especially in young leaves. This pattern was most obvious in the palisade layer due to the more regular cell shapes in this tissue (**Figure 2.7**). Localisation to tangential walls was observed previously in tomato petioles, perhaps suggesting a consistent association between this epitope and new cell divisions (Jones et al. 1997).

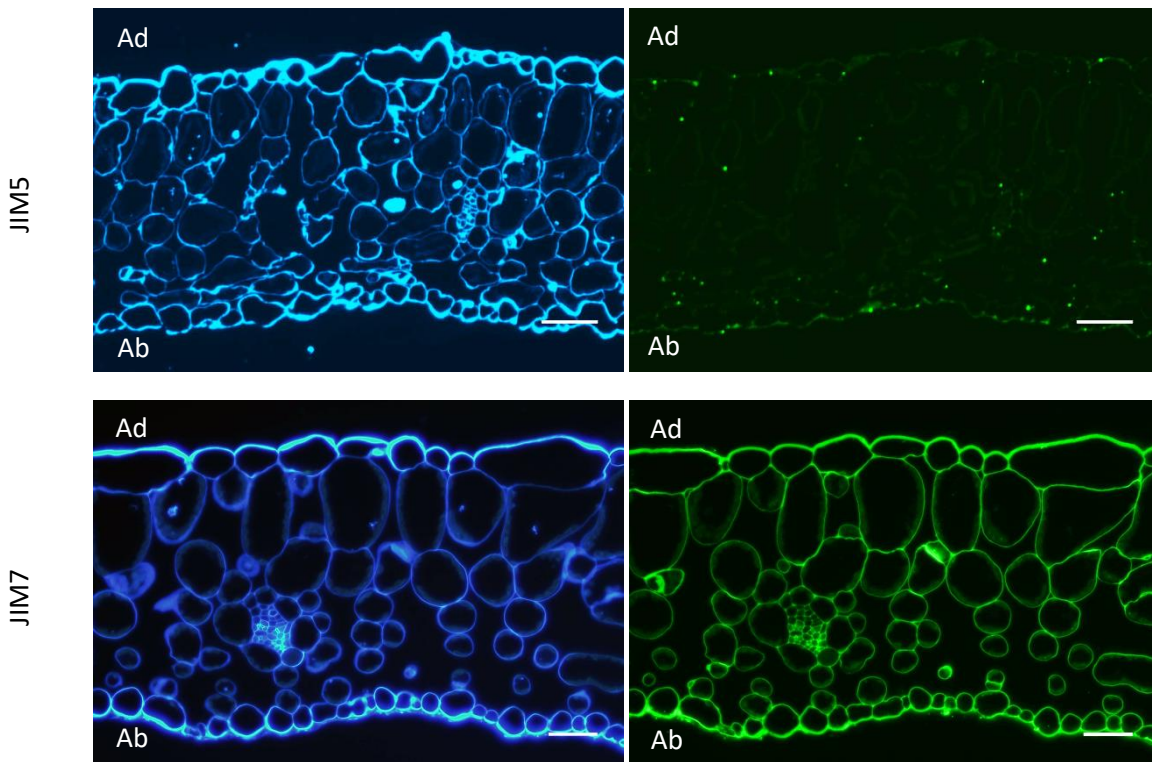


Figure 2.5: JIM5 and JIM7 (anti-HG)

The JIM5 and JIM7 mAbs bind HG epitopes with different degrees of methylesterification. JIM5 binding produced a very sparse, punctate signal, whereas JIM7 binding produced a bright signal throughout the cell walls. Blue images (left hand side) are calcofluor stained. Green images (right hand side) show the secondary mAb signal in the same region of the section. Controls with no primary mAb showed no secondary mAb signal. Scale bars represent 50 μ m. Ab = Abaxial, Ad = Adaxial.

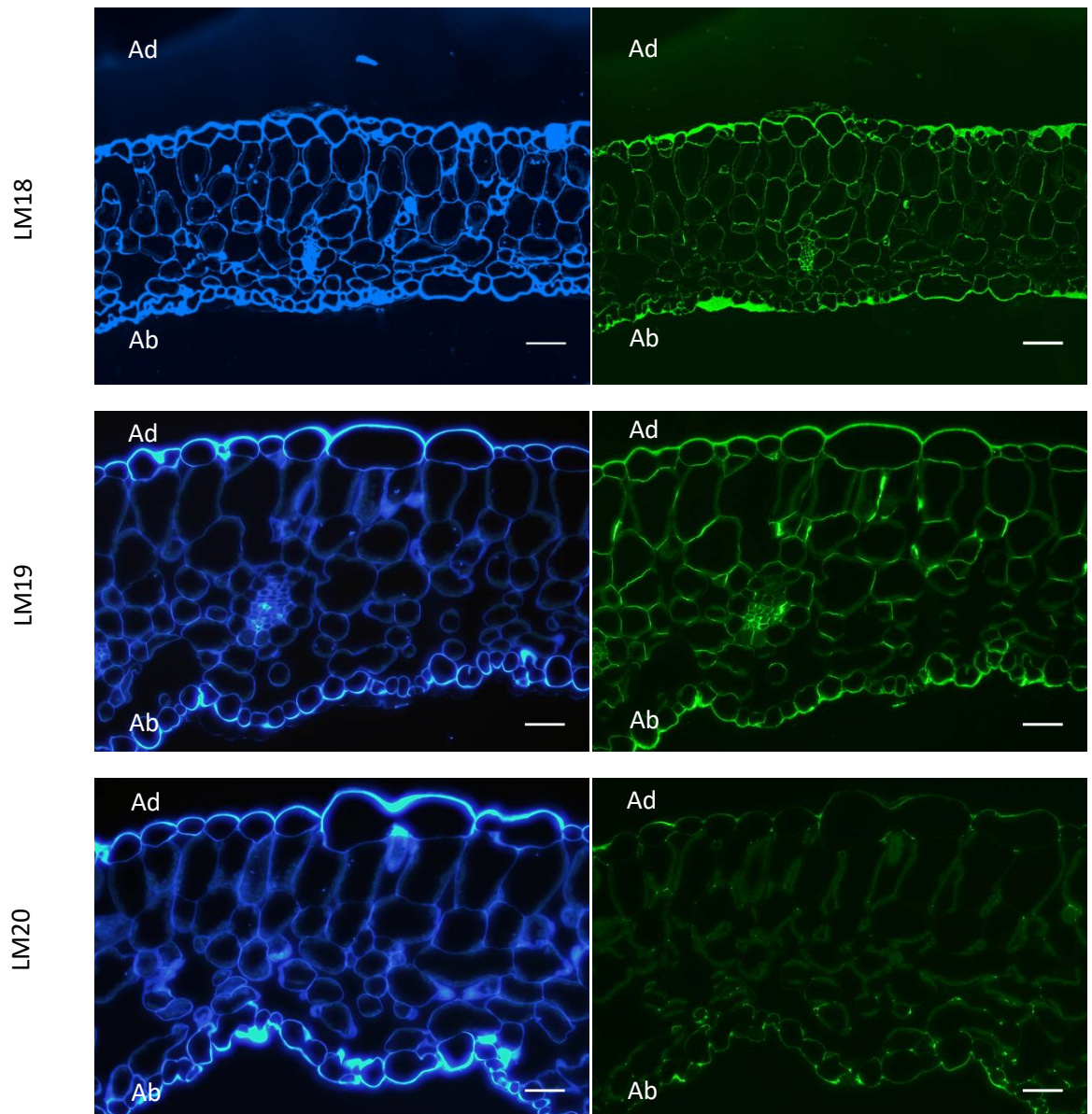


Figure 2.6: LM18, LM19 and LM20 (anti-HG)

The LM18, LM19 and LM20 mAbs bind to HG epitopes with varying degrees of methylesterification. LM18 and LM19 recognise demethylesterified pectin and gave signal throughout the walls with more intense signal in adhered cell walls. LM19 gave more intense signal than LM18. LM20 recognises highly methylesterified pectin and gave the strongest signal at the corners of airspaces. Blue images (left hand side) are calcofluor stained. Green images (right hand side) show the secondary mAb signal in the same region of the section. Controls with no primary mAb showed no secondary mAb signal. Scale bars represent 50 μ m. Ab = Abaxial, Ad = Adaxial.

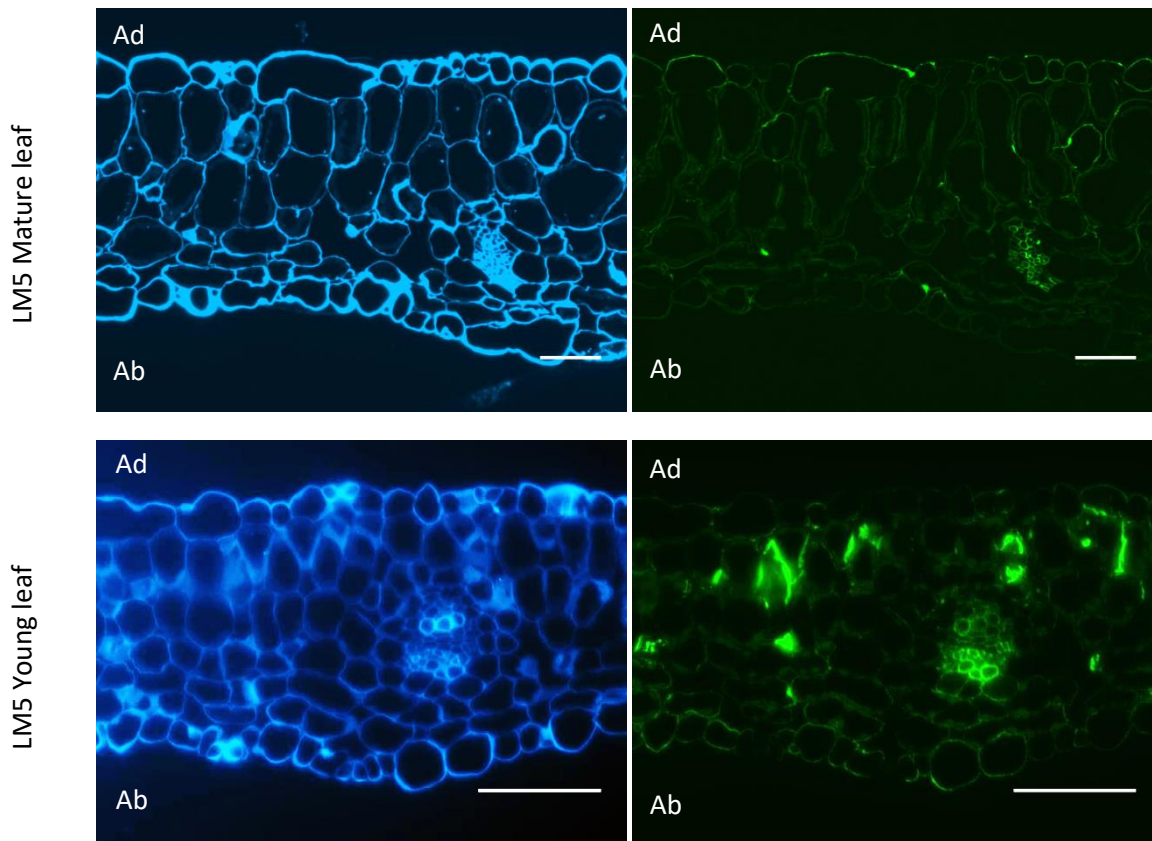


Figure 2.7: LM5 (anti-RG-I)

The LM5 mAb recognises an RG-I epitope. LM5 gave a low level of signal in anticlinal walls of mature leaf sections, and in young leaf sections this binding pattern was more pronounced. Blue images (left hand side) are calcofluor stained. Green images (right hand side) show the secondary mAb signal in the same region of the section. Controls with no primary mAb showed no secondary mAb signal. Scale bars represent 50µm. Ab = Abaxial, Ad = Adaxial.

2.2.3 Glycoproteins

Some arabinogalactan proteins (AGPs) have been previously implicated in cell adhesion (Johnson et al. 2003; Dorca-Fornell et al. 2013). However, we observed no binding for five of the nine anti-AGP mAbs tested (**Table 2-1**), and the pattern of binding of the other four was not obviously related to adhered or separated walls.

LM14 showed the most signal of the anti-AGP mAbs, though this was still sparse, punctate, and often not associated with a cell wall, perhaps indicating detection of the epitope within the endomembrane system. Signal varied somewhat, from sparse punctate binding to more dense patches of signal including some bright areas of cell wall. The epitope was detected in the described pattern in both mature and young leaves. Pre-treatment with PL, as described in 2.2.1, unmasked additional LM14 through more extensive regions of the cell walls of the leaf, with arguably stronger patches of signal in some adhered walls compared to those bordering airspace (**Figure 2.8**). Uniform LM14 binding was previously reported in *Arabidopsis* stem, with a punctate pattern in the cortex (Moller et al. 2008). It is possible that epitope bound by LM14 may also appear on some pectin structures.

Binding of the remaining three anti-AGP mAbs was weak, variable or both (data not shown). JIM16 binding was highly inconsistent between samples: sometimes completely absent, sometimes in the vasculature, and on one occasion also along the outer side of the epidermis. These results are hard to explain but were not followed up due to the absence of binding in the mesophyll. This mAb has been reported not to bind to glutaraldehyde-fixed, resin-embedded samples, so it may also have been unstable following our preparation protocol (Knox et al. 1991). Mac207, which binds some membrane-bound and some soluble AGPs, produced extremely sparse signal patches. The distribution of the signal appeared random, though it was consistently associated with cell walls, and some signal was observed in all mature and young leaf sections examined (Pennell et al. 1989). LM2, which was raised against soluble AGP epitopes, produced a faint signal in the vasculature in some mature and young leaves (Smallwood et al. 1996). Some punctate binding was observed in non-vascular cell walls, but this was highly variable between samples.

Extensin glycoproteins belong to the same superfamily as the AGPs and are involved in cell growth. None of the five mAbs tested displayed any binding to mature or young *Arabidopsis* leaf sections (**Table 2-1**). The epitope recognised by LM1 may be monocotyledon-specific (Smallwood et al. 1995). JIM11, 12, 19 and 20 have previously been used to challenge cryo-sectioned or fresh tissue but it is possible that they were unable to bind to fixed and embedded samples (Smallwood et al. 1994; Smallwood et al. 1996; Wang et al. 1995).

2.2.4 Epitopes found on multiple cell wall component classes

Two of the mAbs that we tested bind epitopes that can be found attached to side-groups on multiple classes of cell wall molecules. The LM12 mAb was raised against a synthetic epitope and binds feruloylated arabinosyl and galactosyl epitopes. This mAb did not give a signal in our mature or young leaf sections. The LM23 mAb was raised against a pectic epitope from apple and binds a xylosyl residue found both in hemicelluloses (xylans) and pectins (xylogalacturonans)(Pedersen et al. 2012). We found no evidence of LM23 binding in young or mature leaves. However, one previous report found that the epitope was unmasked by alkaline pre-treatment, so we may have been unable to detect it since we only labelled untreated sections (Manabe et al. 2011)(data not shown; **Table 2-1**).

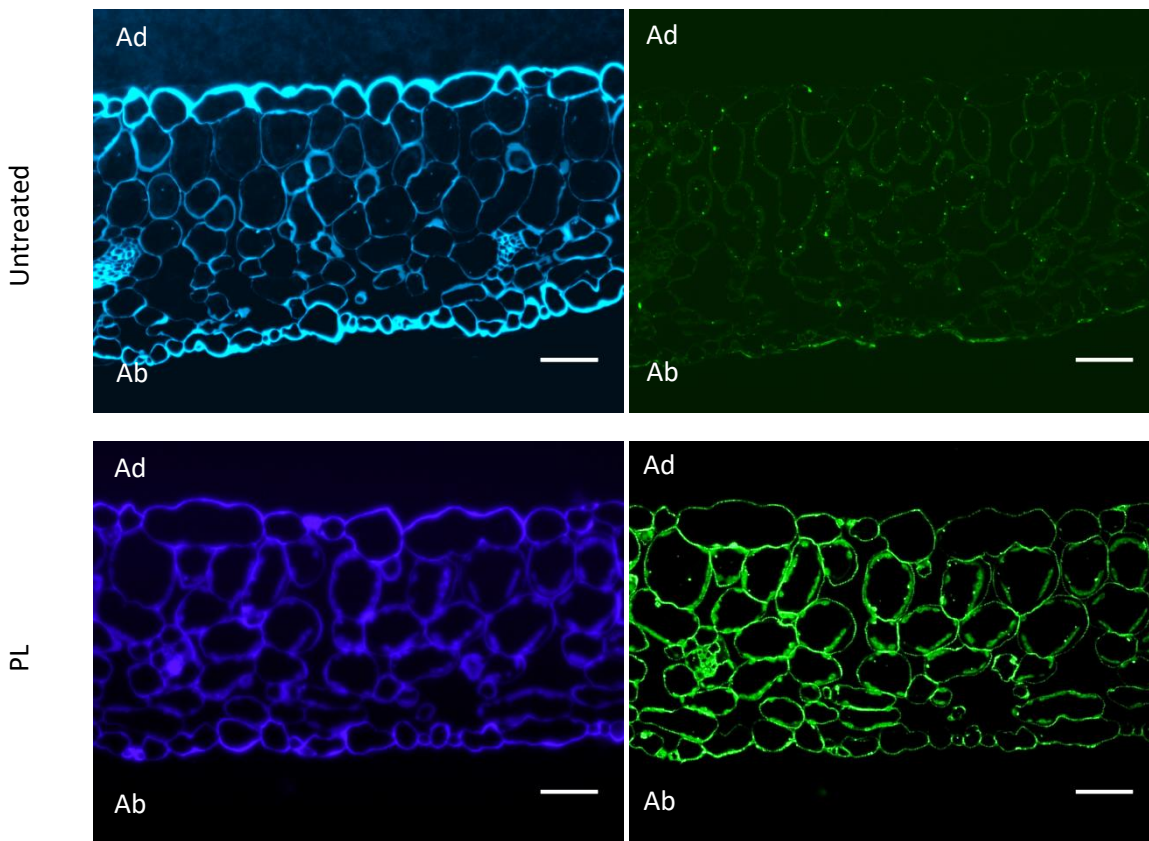


Figure 2.8: LM14 (anti-AGP)

The LM14 mAb recognises an epitope that is most commonly found on AGPs, though may also be found on pectins. LM14 binding produced a sparse, punctate pattern of signal in untreated sections. Pre-treatment of sections with pectate lyase (PL) unmasked the LM14 epitope throughout the cell walls. Blue images (left hand side) are calcofluor stained. Green images (right hand side) show the secondary Ab signal in the same region of the section. Controls with no primary mAb showed no secondary mAb signal. Scale bars represent 50µm. Ab = Abaxial, Ad = Adaxial. (Note: these images were produced by Dr Sam Amsbury.)

Table 2-1: Summary of antibodies tested on resin-embedded leaf sections for which no binding was observed.

Antibody	Binding Specificity
LM24	Xyloglucan
LM22	Mannan
2F4	Calcium cross-linked pectin
LM8	Xylogalacturonan
LM6	(1,5)- α -L-arabinan
LM9	Feruloylated (1,4)- β -D-galactan
LM13	Linearised (1,5)- α -L-arabinan
LM16	Processed arabinan
JIM4	AGP glycan
JIM8	AGP glycan
JIM13	AGP glycan
JIM14	AGP glycan
JIM15	AGP glycan
LM1	Extensin
JIM11	Extensin
JIM12	Extensin
JIM19	Extensin
JIM20	Extensin
LM12	Feruloylated polymers
LM23	Xylan/Xylogalacturonan

2.2.5 Changes in cell wall epitope patterns during development

In most cases binding patterns in the initial screen were the same in young and mature leaves, suggesting that examining even earlier leaf stages might be necessary to reveal the changes that occur in the cell wall to allow mesophyll cells to separate to form airspace. Indeed, although the cells in the young leaf sections that we screened were more densely packed than in the mature leaf sections, there were already some clear intercellular spaces visible. Observations that we made by confocal microscopy suggested that initial separation of cells occurs when the leaves are still too small to embed individually (data not shown).

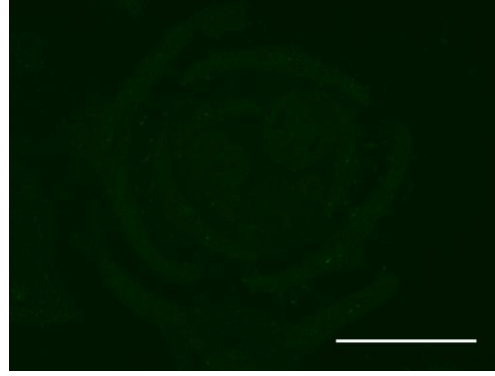
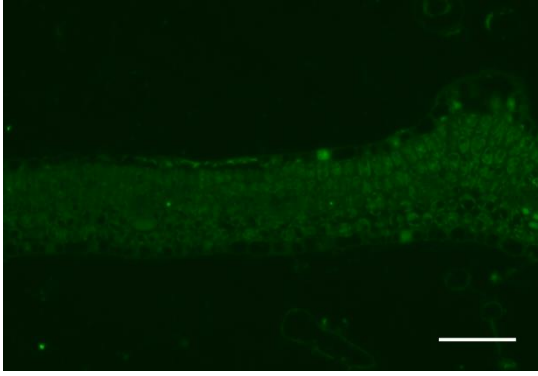
A subset of mAbs that already showed some binding in Arabidopsis leaf mesophyll were selected for further study over a developmental time course which included embedded primordia with the youngest leaves attached. Plants for this study were grown for 14 days on agar plates and all leaves embedded individually. Representative images from the youngest individual leaf stage that we examined (10th leaf) are presented along with images of very young shoot cross-sections (**Figure 2.9**). As mAbs that did not bind either leaf stage in the initial screen were not carried forward, though there is a chance that these epitopes could be detected in younger leaves than we examined.

The anti-HG mAbs that we tested showed some interesting changes early in the development of the leaf. In the mature leaf, the LM20 mAb gives strong signal at airspace corners, suggesting that there is a large amount of highly methylesterified HG there. This was also true in very small leaves that we embedded for the development series. However, when we examined the meristems and very earliest leaves and leaf primordia, we observed much more LM20 signal. On close inspection, localisation to cell junctions was still apparent. Conversely, LM19 signal was less bright in the rosette centres than in the youngest leaves. JIM7 signal was consistent between these two very early stages, and not as strong as in mature tissue.

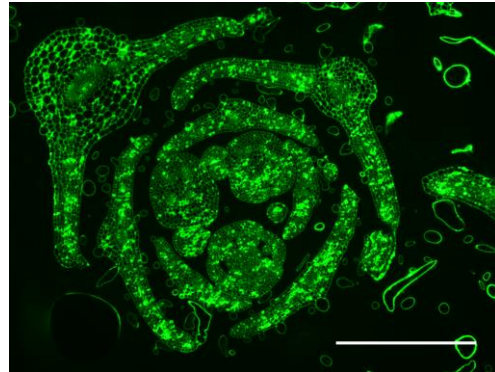
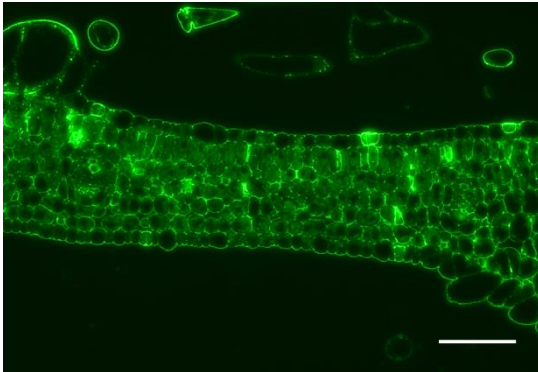
10th leaf at 14 days

Rosette centre at 14 days

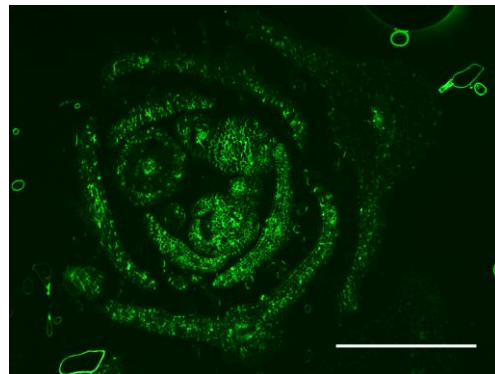
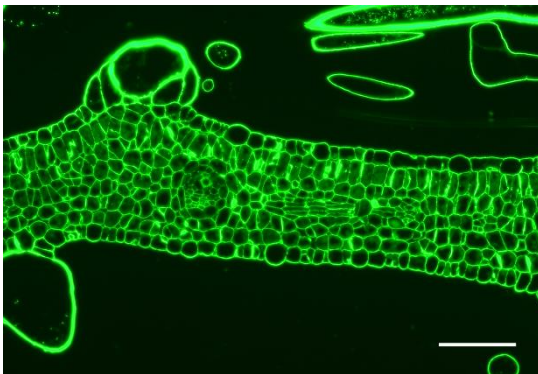
No mAb



JIM7



LM19



LM20

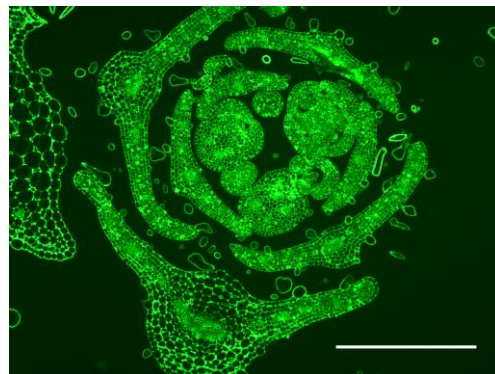
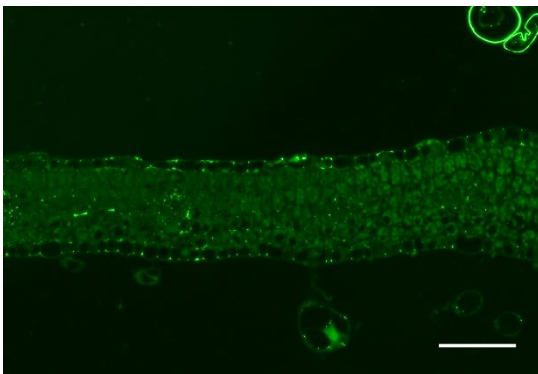


Figure 2.9: Developmental changes in HG distribution

In contrast to mature tissues (**Figure 2.6**), LM20 signal was the strongest in the youngest tissues of the plant shoot (centre of rosette). By the time leaves had reached a sufficient size to embed individually, the epitope composition of the cell walls had already shifted to contain more demethylesterified pectin, recognised by LM19. JIM7 signal was more consistent between these two young tissue stages, but less bright than in mature tissues (**Figure 2.5**). Images show cross-sections through a young leaf (left hand side) and rosette (right hand side) at the stages indicated. Scale bars represent 50µm (left hand side) or 800µm (right hand side).

2.3 Discussion

In this chapter we sought to characterise the composition cell walls of Arabidopsis leaves in terms of the distribution of specific carbohydrate epitopes. We challenged thin tissue sections with a wide range of mAbs and observed where within the leaf structure each component was localised. We hypothesised that some cell wall components would be specifically associated with adhered or separated cell walls. Such adhesion-related components would be logical targets for genetic manipulation, by which means we hoped to generate a panel of cell wall mutants with varying cellular architecture.

2.3.1 Cell wall components in Arabidopsis leaves

We identified a number of hemicellulose, pectin and glycoprotein epitopes that are present in the cell wall of Arabidopsis leaves. The cell wall composition of Arabidopsis leaves had been previously described, but the experiments concerned were carried out on extracted cell wall material and therefore did not provide any spatial information about the localisation of epitopes to different cell types (Zabackis et al. 1995).

Although many of the mAbs that we tested appeared not to bind to Arabidopsis leaf cell walls, where we did observe binding, our results were largely consistent with expected epitope localisations based on the literature. For example we found xyloglucan, the most abundant hemicellulose in dicotyledons, throughout the cell walls (once masking by pectin had been removed), and we found xylan only in the vasculature. We observed a number of HG epitopes, some of which were abundant throughout the cell walls, as one would expect given that HG is the predominant pectin in dicotyledons. We also observed signal from one of the anti-RG-I mAbs, LM5, which bound throughout the walls but gave much stronger signal in anticlinal walls. These data offer novel information about the spatial distribution of certain cell wall epitopes, but our screen certainly cannot be considered exhaustive. We limited our search to a set of mAbs that were readily available and that could all be tested using the same method. Other probes are available including other mAbs that require a different section preparation and/or labelling method, carbohydrate binding modules, and cell wall stains, such as Yariv reagent which detects AGPs (Gilbert et al. 2013; Seifert & Roberts 2007). Furthermore, more detailed information could be gleaned by examining the same set of mAbs at higher spatial resolution by immunogold labelling. This would reveal the cell wall layer with which each epitope is associated. A recent study of the cell wall in Arabidopsis meristems reported signal from both LM13 and LM24, neither of which we tested on such young tissue on account of having observed no binding in mature or young leaves (Yang et al. 2016).

One challenge of interpreting mAb binding pattern data is that many mAbs bind a range of epitopes, and this range has not yet been tightly defined in many cases. Our observations of

the HG-binding mAbs are a prime example of this type of difficulty. When the LM18, LM19 and LM20 mAbs were published, LM19 was reported to be most similar to JIM5 while LM20 bound a similar epitope to JIM7 (Verhertbruggen et al. 2009). It was therefore unexpected when our experiments consistently showed very similar patterns of signal between LM19 and JIM7, and showed LM20 only at airspaces corners, more like the punctate JIM5 signal than the ubiquitous JIM7 signal. These differences can be explained by small differences in the binding affinity of each mAb for various pectin epitopes, but for many mAbs this remains to be tightly defined. Technological advances in the production of carbohydrate microarrays offer promising means to better understand mAb binding profiles in the future (Pedersen et al. 2012; Moller et al. 2008). Accurate interpretation of mAb localisation experiments also requires knowledge of the ways in which the sample preparation method might influence the binding of different mAbs. These issues were addressed in detail in a recent review (Verhertbruggen et al. 2017).

2.3.2 Cell wall components with a potential role in airspace formation

Of the cell wall epitopes that we identified in *Arabidopsis* leaves, the different forms of pectic HG bound by the LM19 and LM20 mAbs appeared to be the only ones to localise to areas of the cell wall that suggested a potential role in cell adhesion (Figure 2.10). While both of these mAbs were able to bind throughout the walls, LM19 gave a slightly stronger signal in adhered walls, and LM20 gave the strongest signal at the corners of airspaces. This perhaps suggests that the HG epitope recognised by LM19 could be involved in adhesion between cells, and that the epitope recognised by LM20 might have a role in limiting the extent of cell separation at the airspace corners, or in actively promoting separation at these points. Furthermore, we observed changes in the abundance of different HG epitopes early in leaf development, which could be involved in the establishment of patterns of cell adhesion or cell expansion.

HG is well known to be a significant constituent of the middle lamella, and a role for HG in cell-cell adhesion has previously been widely suggested and evidenced in other species and tissues (Daher & Braybrook 2015). The existence of specialised areas of cell wall at the corners of airspaces, referred to as 'reinforcing zones', has also previously been proposed, and deposits of highly demethylesterified HG have been localised to these areas in some tissues using the LM7 mAb (Willats et al. 2001). We did not examine the binding pattern of this mAb as it required a different preparation method to those we screened. However, it is intriguing that the LM20 mAb that we found localising to these same zones recognises a highly methylesterified form of HG, in contrast to LM7. One possible explanation could be that newly synthesised pectin, recognised by LM20, is deposited just behind the reinforcing zone. This seems more plausible than a direct role for the LM20 epitope in reinforcement, especially

given that LM20 signal was not observed at all airspace corners. Calcium cross-linking between demethylesterified HG has also been proposed to confer mechanical strength on the reinforcing zone. The 2F4 mAb is specific to calcium cross-linked pectin, but our attempts to label mesophyll sections with this mAb did not give any signal (Liners et al. 1989).

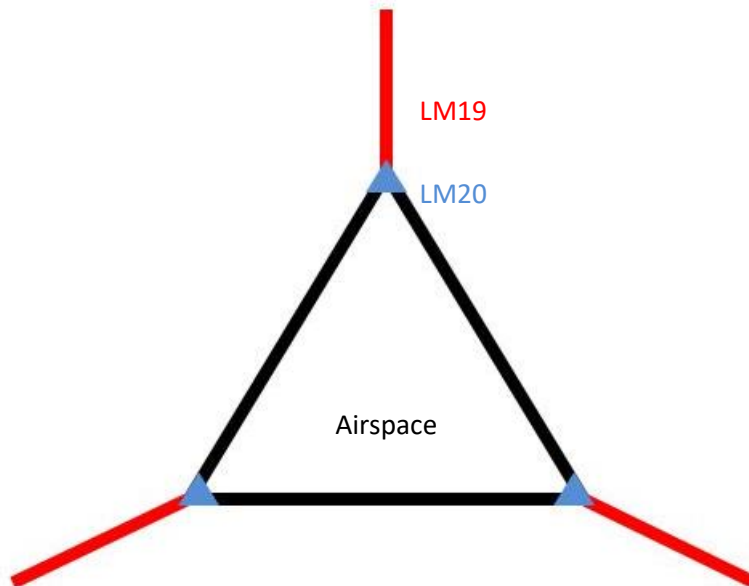


Figure 2.10 Representation of LM19 and LM20 localisation

The central triangle represents a cross-sectional view of an airspace between three cells. The epitope recognised by LM20, which binds to highly methylesterified HG, gives the strongest signal at the airspace corners (indicated in blue). The epitope recognised by LM19, which binds to demethylesterified HG, gives the strongest signal in adhered walls (indicated in red).

Our results suggested that forms of HG with varying degrees of methylesterification might be involved in differential adhesion and separation between cell walls in the mesophyll, and this idea is consistent with published observations in other tissues. This suggested that modifying the extent and/or pattern of HG methylesterification might generate differences in the cellular architecture of the leaf. HG is methylesterified in the golgi apparatus before it is exported to the wall, then demethylesterified *in muro*. In the next chapter we focus on the groups of genes that control these activities and which may therefore cause changes in the cell wall pectin properties if their expression is altered.

2.3.3 Conclusions

Overall our findings were consistent with published accounts of the composition Arabidopsis cells walls, but these data provide a novel insight into the spatial distribution of those components within the leaf tissues. The distributions of forms of HG with different degrees of methylesterification suggested that pectin methylesterification would be a logical target for manipulation to try to generate mutants with varying mesophyll cellular architecture.

Chapter 3 Cell wall pectin and mesophyll cellular architecture

3.1 Introduction

Building the cell wall can be considered as a three-stage process: synthesis of components; targeted delivery of the components to the correct part of the cell wall; and *in muro* modifications, also requiring appropriate delivery of the requisite enzymes (Levesque-tremblay et al. 2015; Daher & Braybrook 2015; Wolf, Mouille, et al. 2009). Our immunolabelling results (Chapter 2) suggested that different forms of pectic homogalacturonan (HG) were associated with adhered and separated cell walls in Arabidopsis leaf mesophyll. We were interested in whether these epitope patterns were essential for development of normal mesophyll structure. Given that the different forms of HG that we observed are generated *in muro* by pectin-modifying enzymes, mutants lacking these activities were a clear priority in our investigation. Certain mutants in pectin biosynthesis and delivery genes have previously been reported to influence the final level of esterified pectin in the cell wall and, in some cases, to reduce cell adhesion, so these were additional candidates for control of leaf cellular architecture.

3.1.1 *In muro* pectin modification

Enzymes including pectin methylesterases (PMEs) and pectin acetylesterases (PAEs) can modify the side-groups of wall-localised pectin, while polygalacturonases (PGs) and pectate lyases (PLs) can cleave the molecular backbone if access is available via a sufficiently long demethylesterified stretch (Sénéchal et al. 2014). PMEs are of particular interest for this study as they influence the levels of the pectin epitopes bound by the LM19 and LM20 mAbs described in the previous chapter. The activity of these enzymes is regulated in part by the antagonistic action of their proteinaceous inhibitors (PMEIs).

The *PME* gene family has approximately 66 members in Arabidopsis and these are sub-divided into *PMEs* (group 1/ type 2) and *pro-PMEs* (group 2/ type 1)(Wang et al. 2013). The group 2 *pro-PMEs* bear an N-terminal 'pre-pro-protein' consisting of a signal peptide and a domain with sequence similarity to PMEIs (Jolie et al. 2010). It has been demonstrated that cleavage of the pro region is required for apoplastic targeting of group 2 PMEs (Wolf, Rausch, et al. 2009), and that it is specifically the transmembrane domain within the signal sequence that determines cell wall localisation (Dorokhov et al. 2006). The PMEI-like domain has been proposed to have auto-inhibitory activity, perhaps preventing premature demethylesterification of pectin in the endomembrane system (Wolf, Mouille, et al. 2009).

Bosch et al. (2005) present some evidence in support of this idea: truncation of the PME1 region impairs plant growth, but can be partially rescued by co-expression of the missing pro-domain. It remains to be discovered by what mechanism intracellular pectin demethylesterification due to a lack of PME auto-inhibition impairs plant growth.

Once PMEs reach the wall their activity can be controlled not only by separate PME1 proteins, but by many other factors, ranging from pH and cation concentrations to the degree and pattern of methylesterification of the substrate (Sénéchal et al. 2014; Jolie et al. 2010). PMEs can demethylesterify pectin in a 'random' or a blockwise fashion; these patterns were once thought to be associated with plant and fungal PMEs respectively, but it is now clear that the situation is more complex (Michelli 2001). The mode and extent of PME action has important consequences for the properties of the pectin network: extensive blockwise demethylesterification can allow access to lytic enzymes, weakening the wall, whereas limited demethylesterification can have the opposite effect, stiffening the wall by facilitating calcium-mediated cross-linking between pectic polymers (Sénéchal et al. 2014; Peaucelle et al. 2012; Ngouémazong et al. 2012). It is also important to note that pectins can play different roles in different layers of the cell wall: an adhesive function is proposed in the middle lamella, whereas changes in primary wall pectin are more often associated with regulation of growth (Palin & Geitmann 2012).

3.1.2 Pectin biosynthesis

Pectins are synthesised in the golgi lumen by the action of at least 67 different enzymes, although relatively few specific actors have been confirmed to date (Anderson 2016; Atmodjo et al. 2013; Mohnen 2008). Homogalacturonan (HG), our pectin of interest, is both the most abundant and the simplest in structural terms. It comprises a backbone of α -(1,4)-linked D-galacturonic acid (GalA) residues with methylester side groups, attached at the C6 position and possible O-acetylation at the O-2 or O-3 positions (**Figure 1.2**; Harholt et al. 2010; Caffall & Mohnen 2009).

Sterling et al. (2006) were the first to provide biochemical demonstration of the activity of an enzyme with a suspected role in pectin biosynthesis in Arabidopsis. *GAUT1* remains the only biochemically confirmed Arabidopsis pectin biosynthesis gene, though other members of the *GAUT* (*GALACTURONOSYLTRANSFERASE*) family have been identified and implicated in pectin biosynthesis (Levesque-tremblay et al. 2015). *GAUT1* is a GalA transferase, involved in building the polygalacturonan backbone. Other family members include *GAUT7*, thought to anchor *GAUT1* into the golgi membrane (Atmodjo et al. 2013), and *GAUT8* (also known as *QUA1*), which has a putative role in pectin backbone synthesis (Bouton et al. 2002).

No PAEs have yet been confirmed in Arabidopsis, but better progress has been made discovering PME s (Anderson 2016). *QUA2* and *QUA3* are members of the 29-gene *QUA* (*QUASIMODO*) family, characterised by their common possession of a specific methyltransferase domain sequence (Sterling et al. 2006). Perhaps unexpectedly, given that *QUA2* is thought to encode a methyltransferase, quantification of pectins extracted from *qua2* (also shown in the allelic *tsd2* mutant) showed that its dwarf phenotype and reduced cell adhesion stemmed from a reduction in total HG rather than any change in the pattern or extent of methylesterification (Mouille et al. 2007; Krupková et al. 2007). In contrast, absence of the *CGR2* and *CGR3* (*COTTON GOLGI-RELATED*) putative methyltransferases has been shown to reduce the level of pectin esterification in the cell wall (Kim et al. 2015). There is much still to be discovered about the specific roles of the many enzymes involved in synthesising even the simpler pectic polymers.

3.1.3 Delivery of pectin and pectin-modifying enzymes to the cell wall

Delivery of pectin and of pectin-modifying enzymes is the least well-studied of the three processes required to build the pectin component of the cell wall. It has been assumed for some time that pectin must be packaged into golgi-derived vesicles and delivered via the actin cytoskeleton, but even this has only recently been partially evidenced (Anderson 2016; Palin & Geitmann 2012; Mohnen 2008). The highly conserved *ARP2/3* (*ACTIN-RELATED PROTEIN 2/3*) actin nucleation complex is critical for correct actin filament organisation and cell shape morphogenesis. It has been proposed to play a role in delivery of cell wall components, though published evidence to support this idea remains scarce (Li et al. 2003; Daher & Braybrook 2015). Dyachok et al. (2008) were able to observe an ultrastructural change in cell wall thickness at some three-way cell junctions in *arp2* mutant roots, and mutations in two other members of the complex both have a reduced cell adhesion phenotype in the hypocotyl, though a causal change in the cell wall was not demonstrated (Mathur et al. 2003). However, aberrant pectin methylesterification levels have been observed in these mutants (Firas Bou Daher, unpublished data).

Localisation of cell wall molecules by their targeted delivery, or that of their modifying enzymes, has been best studied in the context of pollen tube growth (Palin & Geitmann 2012; Bosch & Hepler 2005). Spatial heterogeneity in pectin epitopes associated with differential local wall extensibility has been confirmed in this system, though whether it is caused solely by differential regulation of PME enzyme delivery and/or activity, or whether differential delivery of pectin molecules from the golgi is also involved, remains unknown (Anderson 2016). Studies of pollen tip growth also led to the intriguing suggestion that pectin demethylesterification can be partly regulated by endocytosis of PMEIs, which is another actin-dependent process. Röckel

et al. (2008) identified two interacting, pollen-expressed PMEIs with opposite activities with respect to growth promotion/repression, and showed that only one of them was found in endocytic vesicles, providing a mechanism for fine, local control of PME activity.

3.1.4 Aims

Based on the localisation of the LM19 and LM20 antibodies in Chapter 2, we hypothesised that altering the distribution of HG epitopes with varying levels of demethylesterification would affect the cellular organisation of the leaf by modifying the degree of adhesion between neighbouring cells. Daher & Braybrook (2015) suggest that the similarity in relative pectin esterification levels between certain methyltransferase mutants and wildtype plants provides evidence that, at least in some cases, quantity rather than quality of pectin may be the key regulator of cell adhesion. In this chapter we obtain and generate a range of transgenic *Arabidopsis* lines with known or expected alterations in the quantity and/or quality of pectic HG in the cell wall. We use the aforementioned *qua1*, *qua2* and *arp3* mutants to investigate the relationship between cell wall composition, leaf cellular architecture and leaf-level physiology.

Note: The plant lines described in sections 3.2.3 and 3.2.4 were analysed in one experiment. Data for all three lines are presented as combined figures, but the *qua* mutants are discussed separately from *arp3*.

3.2 Results

3.2.1 Identification and characterisation of leaf-expressed *PME* genes

3.2.1.1 *Gene expression analysis*

Having identified modification of pectin methylesterification as a potential regulator of cell adhesion, we sought to identify genes regulating this function. We examined publicly available microarray data to identify those *PME* genes most likely to have a role in mesophyll airspace formation. The Schmid et al. (2005) microarray includes a number of leaf developmental stages; we examined data from all rosette leaf tissue samples from Col-0 grown on compost under continuous light. To select confirmed and putative *PME* genes for investigation, we compared the Arabidopsis *PME* gene lists from Wang et al. (2013) to the list of genes returned by searching for 'pectin methylesterase' in the TAIR database (accessed November 2016). This generated a working list of 75 genes, 50 of which were common to both sources and nine of which were not on the microarray.

Expression of all *PME* genes was plotted against leaf developmental stage (**Figure 3.1**), which showed a group of 17 genes that were clearly much more highly expressed in leaves than the other *PMEs*. For nine of these most highly expressed genes, up to three mutant lines were obtained from NASC, and their insertion positions checked using SIGNAL and TAIR to select insertions in exons where possible (**Table 3-1**). Plants from NASC were genotyped and, if necessary, selfed to obtain homozygous seed.

Table 3-1: *PME* mutant lines in highly leaf-expressed genes, obtained for immunolabelling.

Gene	Insertion Mutant
AT3G14310 (PME3)	GK-329D07
AT3G10720	SALK_021426
	SALK_122120
	SALK_006529
AT3G49220 (PME34)	SALK_062058
AT4G02330 (PME41)	SALK_008958
AT4G33220 (PME44)	SALK_071362
AT2G26440 (PME12)	SALK_058895
	SALK_117817
AT5G09760	SALK_075984
AT1G53840 (PME1)	SALK_120021
AT1G11580	SALK_067447
	SALK_121787

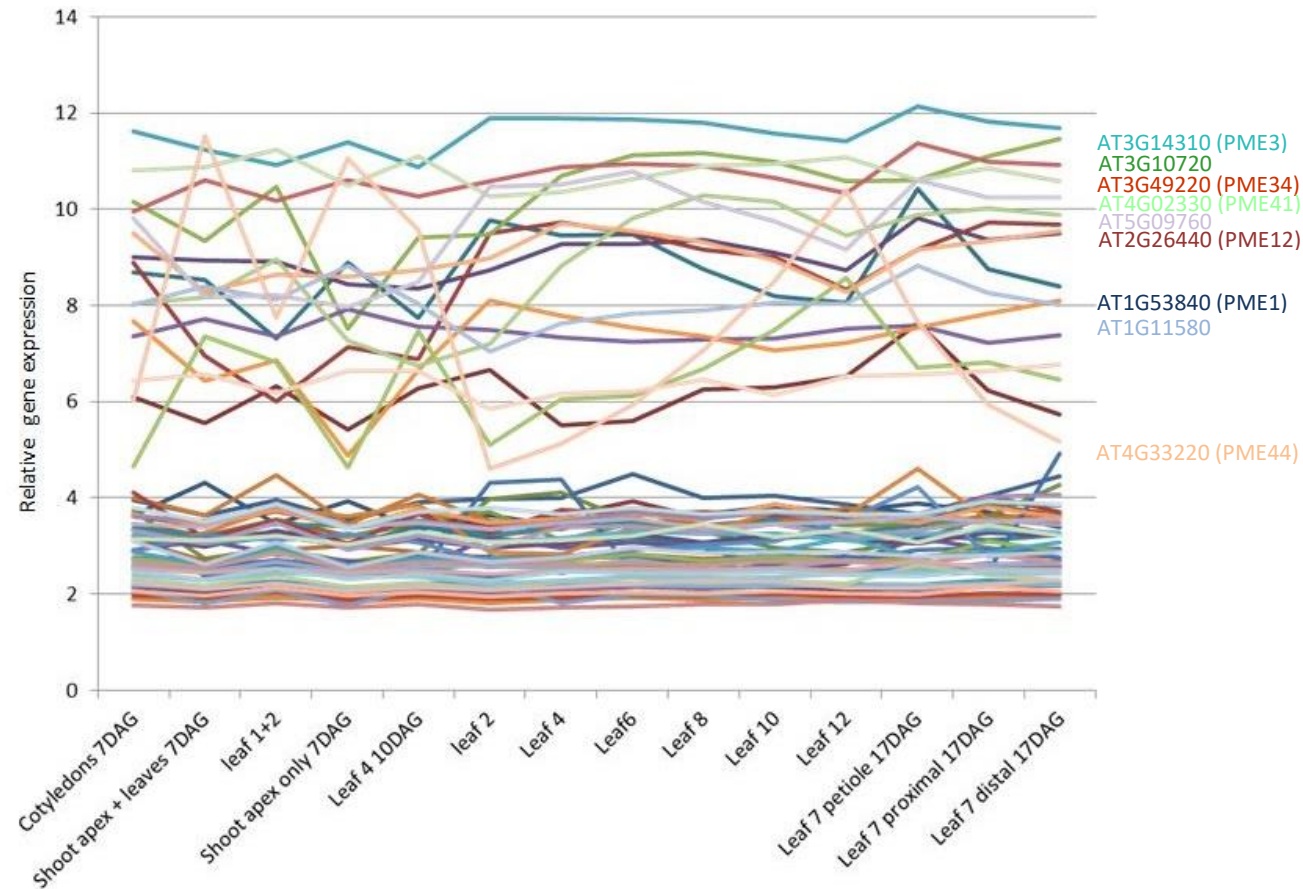


Figure 3.1: Graphical representation Arabidopsis *PME* gene expression

Relative expression levels of *PME* genes at various leaf growth stages (plant age and leaf number) of (confirmed and putative) *PME* genes, according to the Schmid et al. (2005) microarray. Plotted expression values are the mean of three replicates. Most genes show a low level of expression, but a distinct group of 17 genes are moderately to highly expressed in all samples. The genes indicated were selected for characterisation based on highest peak expression values, and availability of knockout lines from NASC (Nottingham Arabidopsis Stock Centre). A full list of genes presented on this graph can be found in Appendix 1.

3.2.1.2 Growth on compost and immunolabelling

Homozygous *pme* mutant plants from NASC were grown on compost and monitored to look for differences in growth and gross phenotype. Most plants looked indistinguishable from Col-0 by eye (**Figure 3.2**). Two plants of SALK_006529 line were a little smaller, but all other plants of that genotype, within and between the three independent SALK lines, were Col-0-like. In this absence of a gross visual phenotype, plants used for immunolabelling analysis were genotyped to re-confirm that they were homozygous as expected.

Samples were taken from five-week-old plants and embedded for immunolabelling with JIM7, LM19 and LM20 antibodies to see whether any change in pectin epitope localisation could be detected. The *pme3* line GK-329D07, a mutant in the most highly leaf-expressed *PME* gene according to the microarray data, showed an absence of the LM19 epitope in the mesophyll, in contrast to the wild type (**Figure 3.3**). However, this was not paired with an increase in the LM20 epitope, suggesting that pectin may still be being modified, but that the resulting epitope is not recognised by LM19. This is in contrast to the *pme6* mutant in which loss of stomatal LM19 is paired with an increase in LM20 (Amsbury et al. 2016). All other lines examined showed no difference in the distribution of the three examined pectin epitopes within the leaf transverse sections (data not shown).

We hypothesised that the pattern of pectin epitopes that we observed in the wildtype was functionally related to the formation of airspace in the leaf, and that alteration of the pectin epitope pattern would be paired with a change in leaf cellular architecture. From the sections used for immunolabelling, there was no very striking difference between the *pme3* mutant and the wildtype. Unfortunately this mutant was not discovered in time for it to be analysed by microCT (see 2.3.2) in the timeframe of this project. Using this approach in the future would allow detection of any changes in porosity and airspace distribution.



Col-0



SALK_021426



GK329-DO7 (*pme3*)



SALK_122120



SALK_062058



SALK_006529



SALK_008958



SALK_058895



SALK_071362



SALK_117817



SALK_067447



SALK_075984



SALK_121787

Figure 3.2: Growth of *pme* mutants

Images of all *pme* knockout lines (as indicated) after five weeks of growth on compost under short day conditions showed no obvious phenotypic differences between lines at the whole plant level.

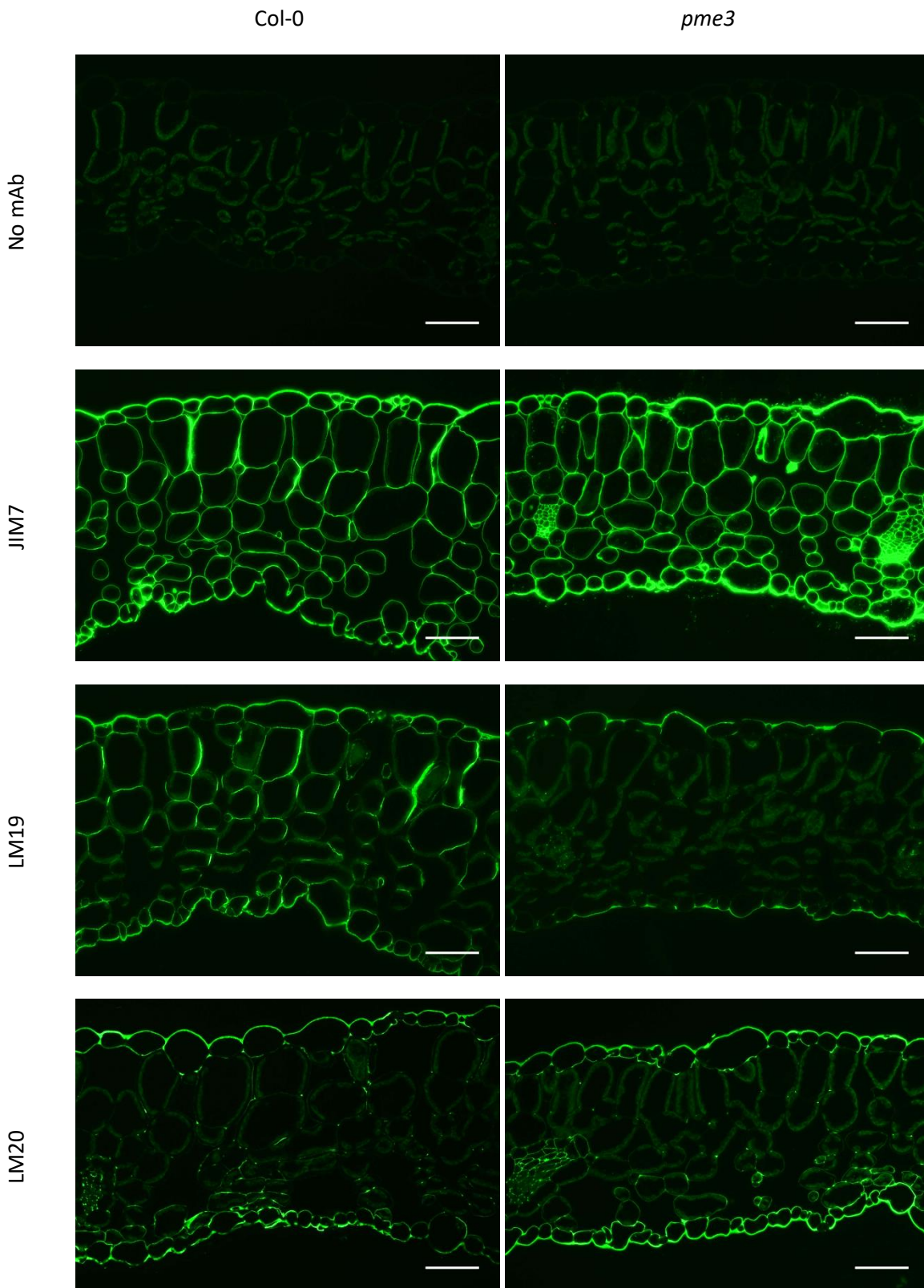


Figure 3.3: *pme3* immunolabelling with anti-HG mAbs

Immunolabelling of the *pme3* knockout mutant (GK-329D07) revealed an absence of LM19 binding in the leaf mesophyll as reported by the LM19 mAb, in contrast to our observations of Col-0 wildtype plants. JIM7 and LM20 produced similar signal patterns to those observed in Col-0. Scale bars represent 50µm.

3.2.2 Generation and characterisation of mesophyll-targeted *PMEI* overexpression lines

3.2.2.1 Generation of transgenic lines

As a complementary approach to obtaining knockout mutants to try to study the effects of reduced PME activity, we generated transgenic lines expressing proteinaceous PME inhibitors (PMEIs) under the mesophyll-specific promoter *pCA1* (CARBONIC ANHYDRASE 1; Gowik et al. 2004) with the aim of reducing the activity of multiple potentially mesophyll-active PMEs simultaneously (**Figure 3.4**). *PMEI* overexpression lines under the 35S promoter have previously been generated for the investigation of PME-dependent pathogen defence (Lionetti et al. 2007), but we were unable to obtain seeds.

Three *PMEI* genes were selected for cloning. *AtPMEI1* and *AtPMEI2*, as used by Lionetti et al. (2007), are native Arabidopsis genes, only naturally expressed in pollen. In case their misexpression could be counteracted *in planta*, we also cloned *AdPMEI1* from kiwifruit (*Actinidia deliciosa*) in the hope of circumventing any endogenous controls in Arabidopsis. PMEI proteins were first identified in the closely related kiwi species *Actinidia chinensis* (Balestrieri et al. 1990; Giovane et al. 2004) and have been predicted to interact with a number of Arabidopsis group 2 PMEs expressed in Arabidopsis vegetative tissues (Paynel et al. 2014). For each of these three *PMEI* genes the full coding sequence was cloned. This included the signal peptide that targets the protein to the membrane. Only the *AtPMEI2* and *AdPMEI1* lines were ready for characterisation within the timeframe of this project. At least three independent T₃ lines, with paired sister line controls, were selected for characterisation of each construct.

3.2.2.2 Growth on compost and immunolabelling

Compost-grown plants were monitored over five weeks of growth. Most mutant lines were indistinguishable from Col-0 or their segregating sister lines at the gross phenotype level, though there was considerable growth variation among the plants in general (**Figure 3.5**). Some lines appeared paler in colour, suggesting a lower density of chloroplasts. This could either be due to reduced cell density, or due to the construct having inserted in an undesirable position in the genome. The latter seems likely given that other independent lines carrying the same constructs did not share this phenotype. Samples for immunolabelling with the anti-pectin mAbs JIM7, LM19 and LM20 were taken from mature leaves of five-week-old plants. Sections of all lines displayed patterns of mAb binding indistinguishable from Col-0 or their segregating sister lines (**Figure 3.6**). This does not preclude the possibility of a quantitative change in pectin esterification in the mutants but, as no clear difference was detectable by immunolabelling, the lines were not characterised further.

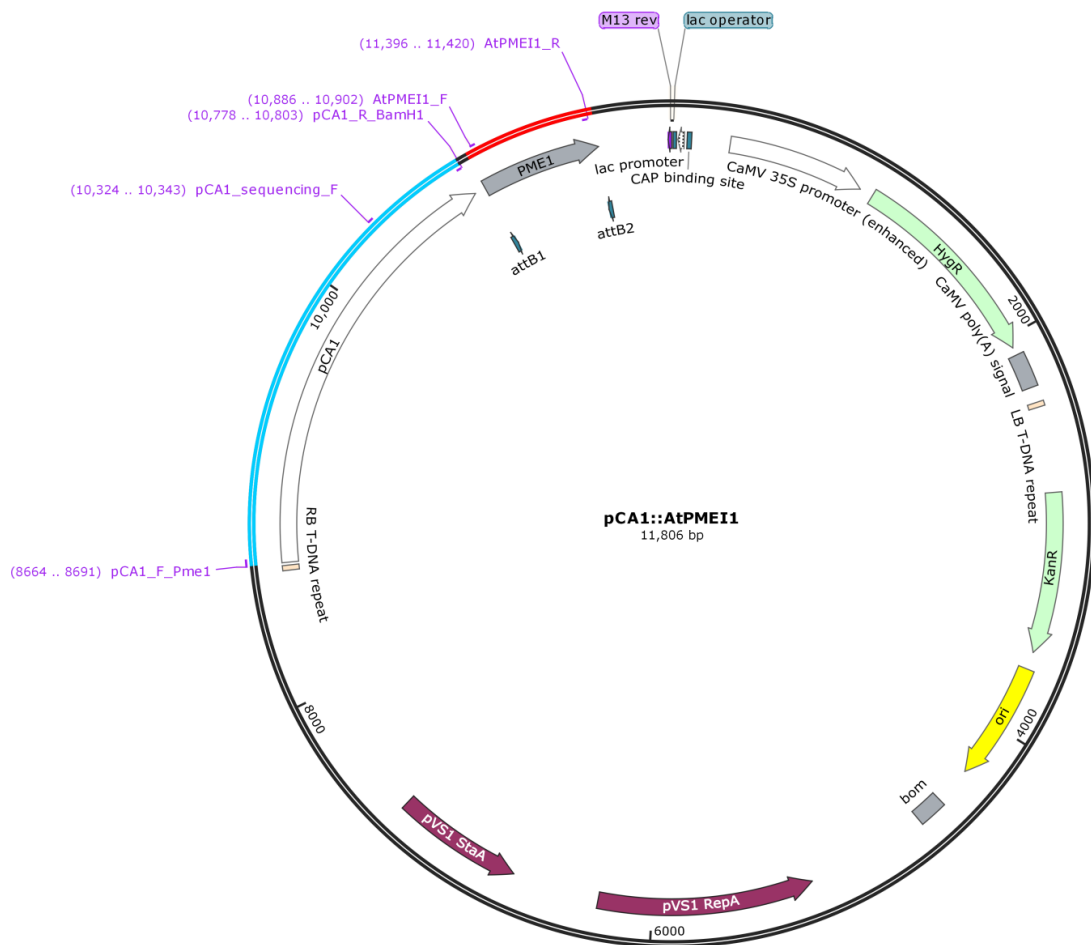


Figure 3.4: pCA1::AtPMEI1 construct map

Example map of a complete expression vector used to generate *PMEI* overexpression lines. Key features of the modified pMDC32 plasmid are marked, including the pCA1 promoter, the inserted gene (in this case *AtPMEI1*), and the hygromycin resistance gene for selection in plants. The primers used to generate the insert and promoter, and those used for colony PCR, sequencing and genotyping, are also indicated. Primer sequences are listed in Materials and Methods.



Col-0



pCA1::*AtPMEI2-A*



pCA1::*AtPMEI2-A-sister*



pCA1::*AtPMEI2-B*



pCA1::*AtPMEI2-B-sister*



pCA1::*AtPMEI2-C*



pCA1::*AtPMEI2-C-sister*



pCA1::AdPMEI1-A



pCA1::AdPMEI1-A-sister



pCA1::AdPMEI1-B



pCA1::AdPMEI1-B-sister



pCA1::AdPMEI1-C



pCA1::AdPMEI1-C-sister



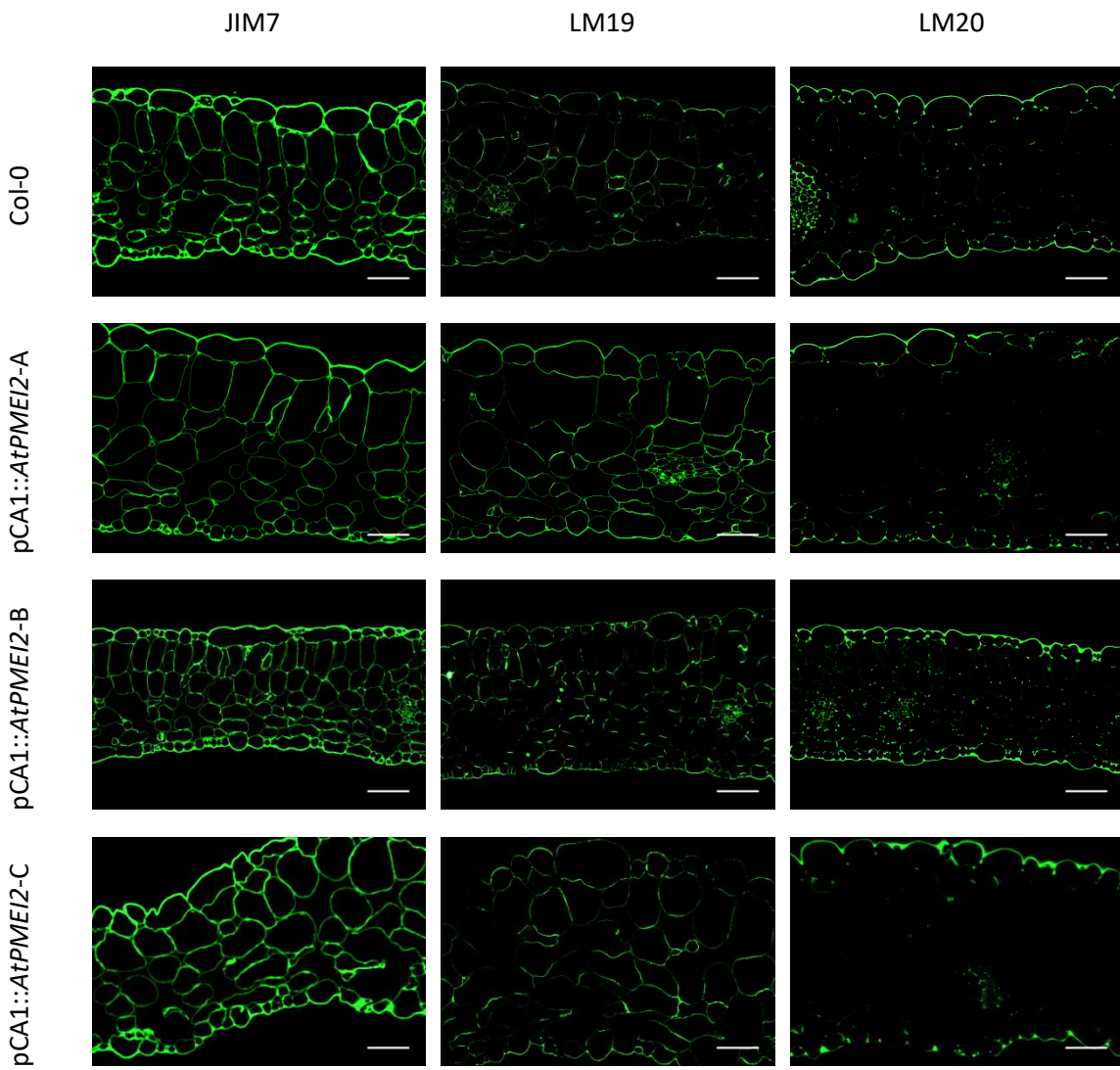
pCA1::AdPMEI1-D



pCA1::AdPMEI1-D-sister

Figure 3.5: Growth of pCA1::PMEI lines

Most of the transgenic lines that we generated to express *PMEI* genes (as indicated, left column) in the mesophyll did not grow abnormally on compost compared to their segregating sister lines (right column) or Col-0. There was some variation in plant size throughout the population, and some lines were noticeably pale, but this was deemed unlikely to be due to a direct effect of the transgene. Pots are 60x60mm.



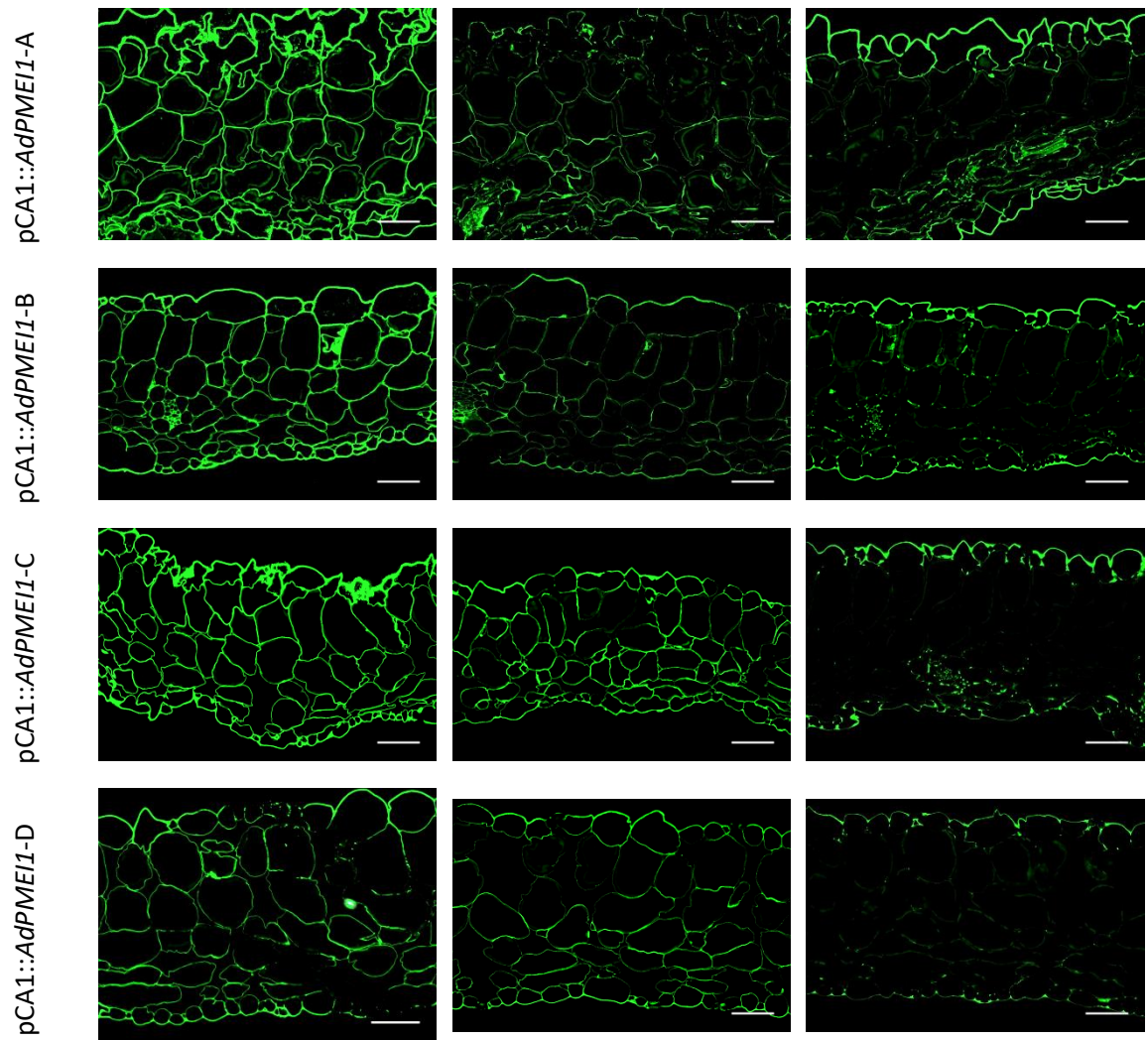


Figure 3.6: Immunolabelling of pCA1::PMEI lines

No clear differences in HG epitope localisation were detected in any of these transgenic lines (constructs as indicated). Segregating sister lines were also immunolabelled and, as expected, showed no difference from Col-0 (data not shown). Scale bars represent 50 μ m.

3.2.3 Characterisation of *quasimodo* pectin biosynthesis mutants

3.2.3.1 Growth on compost

Two lines impaired in pectin biosynthesis and with reportedly aberrant cell adhesion were obtained: *qua1* (Bouton et al. 2002) and *qua2* (Mouille et al. 2007; Frank et al. 2002). Both mutants displayed abnormal growth on compost (**Figure 3.7**). The *qua1* mutant was considerably dwarfed, as previously described, and had much rounder leaves than a wildtype plant, with a paler green colour, suggesting lower chlorophyll content. The *qua2* mutant has also been described as dwarf, though under our growth conditions dwarfing compared to Col-0 varied, with only a subtle size reduction in many cases. It also had relatively longer petioles and a more irregular leaf surface topography.

3.2.3.2 MicroCT imaging

The disrupted mesophyll phenotype of the *quasimodo* lines was confirmed and quantified by microCT imaging (**Figure 3.8-A**). MicroCT (micro computed tomography) is an x-ray based technique that measures sample density, allowing airspaces and cellular material to be easily distinguished, and thereby providing insights into the amount and distribution of airspace within leaves (Pajor et al. 2013). This revealed a significant increase in porosity in both *qua* mutants (**Figure 3.8-B**). Interestingly, this change in porosity was distributed differently in the two mutants. While both showed some increase in palisade porosity, only *qua1* was significantly more porous than Col-0 in this tissue (**Figure 3.8-D**). In the spongy mesophyll *qua1* was barely more porous than Col-0, whereas *qua2* was significantly more porous than both other lines (**Figure 3.8-E**). The porosity increase in *qua2* manifested itself as a shift to fewer, larger air channels, while *qua1* had fewer channels still, but a very similar channel size to Col-0 (**Figure 3.8-F,G**). There was a small, significant difference in thickness between the two *qua* lines (**Figure 3.8-C**), which could be one factor in the enhanced rates of photosynthesis in *qua2* (below).

The exposed surface area of mesophyll cells to the intercellular space is considered an important factor regulating the potential for CO₂ uptake, but this factor was largely unaffected by the changes in cellular organisation in the *qua* mutants, with the only statistically significant difference from Col-0 being a slight elevation in the *qua1* overall and palisade mesophyll surface area (**Figure 3.9-A,B**). There were no significant differences in spongy mesophyll exposed surface area between any of the lines (**Figure 3.9-C**).

3.2.3.3 Gas exchange analysis and stomatal characteristics

The structural imaging was paired with gas exchange analysis to examine the physiological performance of these plants. The fragile nature of the *qua1* mutant made it challenging to

apply the leaf clamp without damage to the plant. *qua1* was less able than Col-0 to assimilate CO₂ across a range of CO₂ concentrations (**Figure 3.10-A**) or under high light (**Figure 3.10-B**). Despite elevated stomatal density (**Figure 3.11-A**), *qua1* stomatal conductance (g_s) was a little lower than wildtype (though also more variable), except at high C_i (leaf internal CO₂ concentration), perhaps suggesting a smaller dynamic range for stomatal movement (data not shown). Higher stomatal density was not simply due to the dwarf mutant having smaller cells, as the stomatal index was also elevated (**Figure 3.11-B**). It is unclear how the cell wall defects reported in *qua1* would cause a change in stomatal patterning; perhaps it could be a compensatory developmental response to try to overcome compromised gas exchange.

In contrast, the *qua2* mutant consistently outperformed Col-0 under all CO₂ conditions (elevated V_{cmax}, the maximum rate of carboxylation, and A_{satr}, the maximum assimilation under saturating CO₂; **Figure 3.10-A**), and matched the Col-0 response to changes in incident light (**Figure 3.10-B**). The measured g_s of the *qua2* mutant was the same as Col-0 under all conditions tested (data not shown), and stomatal density was also the same as Col-0 (**Figure 3.11-A**), suggesting that the improvement in assimilation was not related to any stomatal change. Stomatal index was slightly elevated, indicating an increase in stomata relative to other epidermal cells, but this would not be expected to alter photosynthesis on a per-area basis (**Figure 3.11-B**).

We were unable to obtain reliable data on *qua1* stomatal CO₂ response using the bioassay method due to the difficulty in peeling strips of epidermis from these fragile leaves. Attempts at *qua2* bioassays have provided quite variable results, but do not suggest a strikingly aberrant stomatal opening or closing response (data not shown).

3.2.3.4 Immunolabelling

We took an immunolabelling approach to see if any qualitative change in pectin epitope distribution could be detected in the *qua2* pectin biosynthesis mutant. We found no visible change in the binding pattern of the anti-pectin mAbs that we examined (**Figure 3.12**). This is consistent with published data that found a reduction in HG quantity rather than in the pattern or degree of methylesterification in extracted wall material (Mouille et al. 2007; Bouton et al. 2002).



Col-0



arp3



qua1

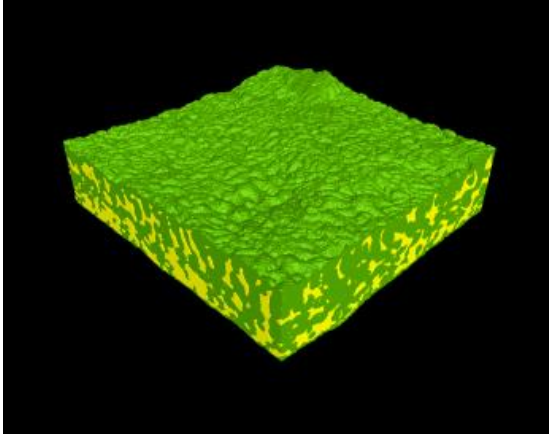


qua2

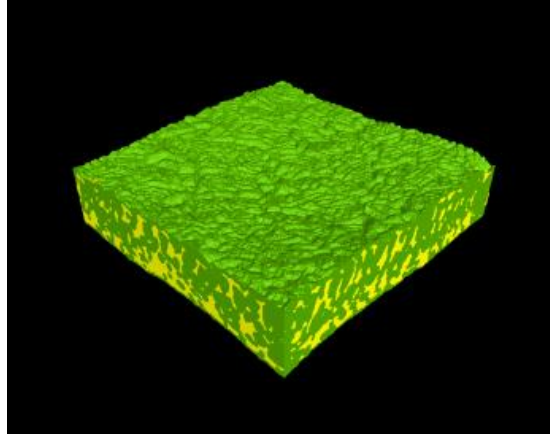
Figure 3.7: Col-0, *qua1*, *qua2* and *arp3* growth on compost

The *qua* mutants have been described as dwarf. This phenotype was most obvious in *qua1*, whereas under our growth conditions dwarfing of *qua2* was more variable, and never as extreme as *qua1*. The *arp3* mutant grew to a similar size to Col-0 but had broader leaves. Measurements (CO_2 and light response curves followed by microCT scans) were taken on the largest leaves at 35-42 days after germination. These images were captured 42 days after germination. Pots are 60x60mm.

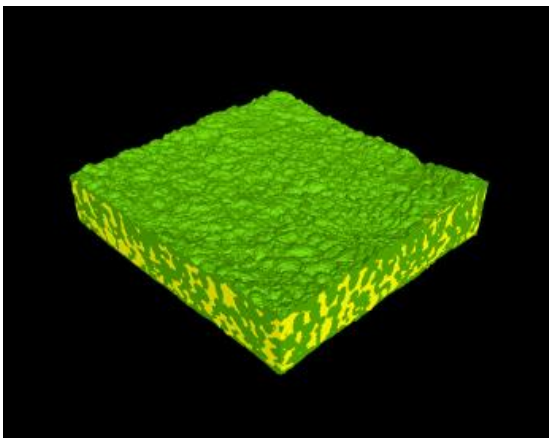
A



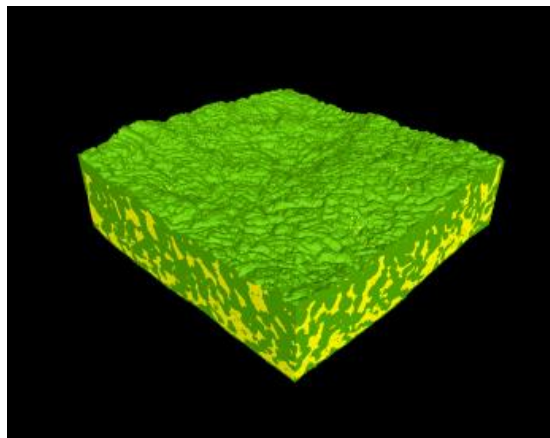
Col-0



arp3

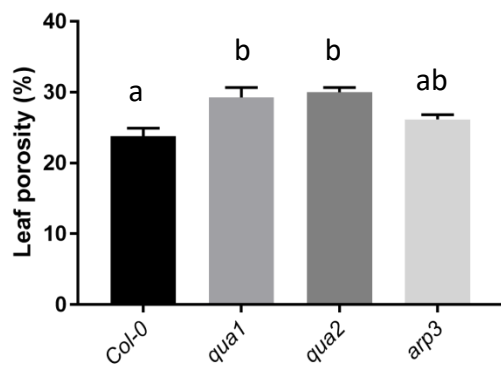


qua1

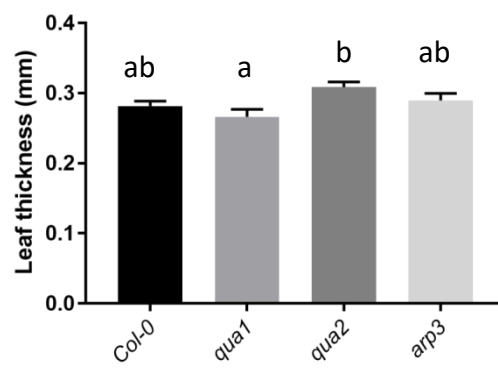


qua2

B



C



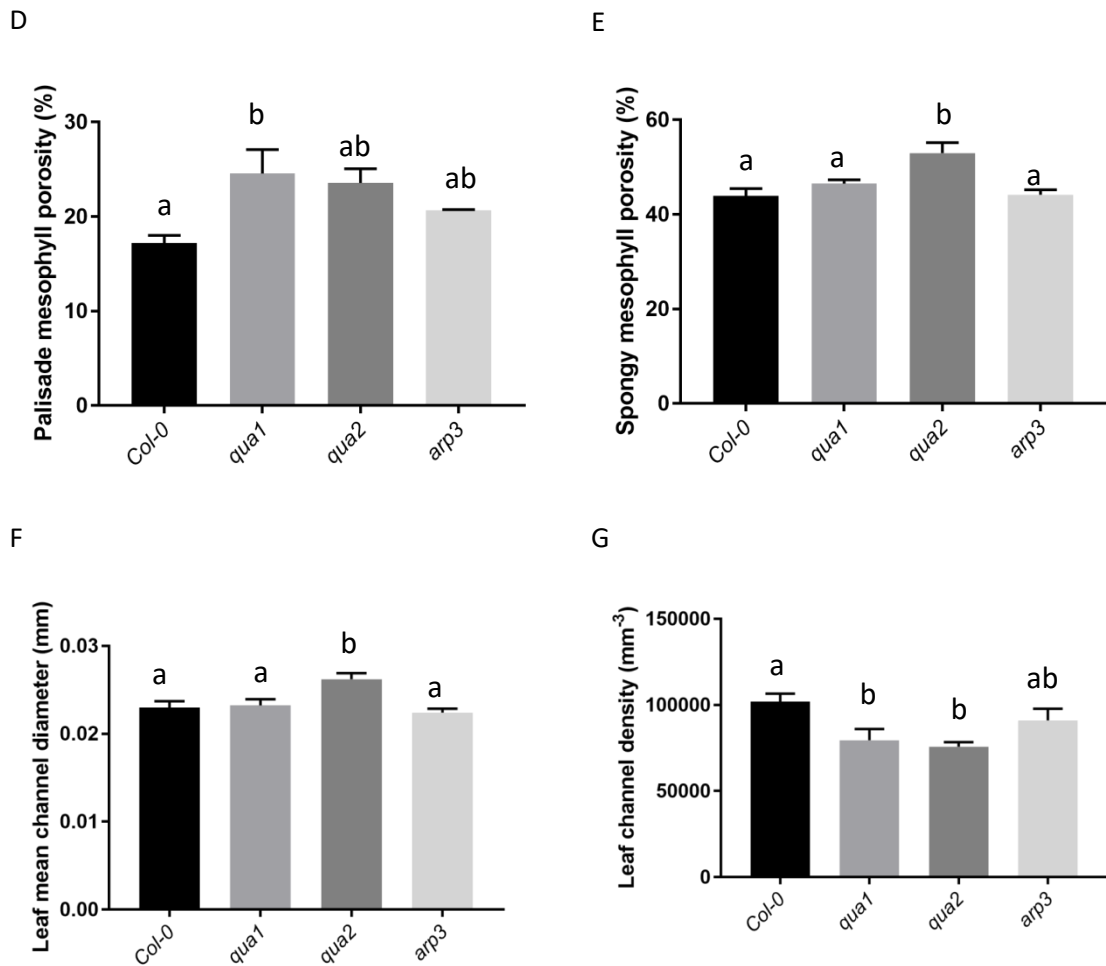


Figure 3.8: Porosity of Col-0, *arp3*, *qua1* and *qua2* leaves

(A) Representative 3D renderings of microCT image data for each plant line. Samples represent the regions used for quantitative analysis (1.1mm²). (Note: these renderings were generated by Dr Andrew Mathers at the Hounsfield Facility, University of Nottingham).

(B) Leaf porosity, the proportion of the leaf volume occupied by airspace, differed significantly between lines (One-way ANOVA, $F_{(3,14)}=7.34$, $P=0.003$).

(C) There were only slight differences in leaf thickness between lines, with a small, significant difference between *qua1* and *qua2* (One-way ANOVA, $F_{(3,14)}=4.36$, $P=0.023$).

(D) *qua1* had significantly higher palisade mesophyll porosity than Col-0, with other lines intermediate (One-way ANOVA, $F_{(3,14)}=4.10$, $P=0.028$).

(E) *qua2* had significantly higher spongy mesophyll porosity than all other lines (One-way ANOVA, $F_{(3,14)}=7.02$, $P=0.004$).

(F) The average *qua2* air channel diameter was greater than that of all other lines (One-way ANOVA, $F_{(3,14)}=6.03$, $P=0.007$).

(G) The pattern of differences in the density of air channels in the leaf was the opposite of the pattern in channel size, with a significant difference between each *qua* mutant and Col-0 (One-way ANOVA, $F_{(3,14)}=5.77$, $P=0.009$).

These data are derived from microCT images from 1.1mm² leaf regions. All error bars represent the standard error of the mean. N=5 except for *arp3* where N=3. Letters indicate groups of lines that are not significantly different from one another according to the post-hoc Tukey test ($p<0.05$).

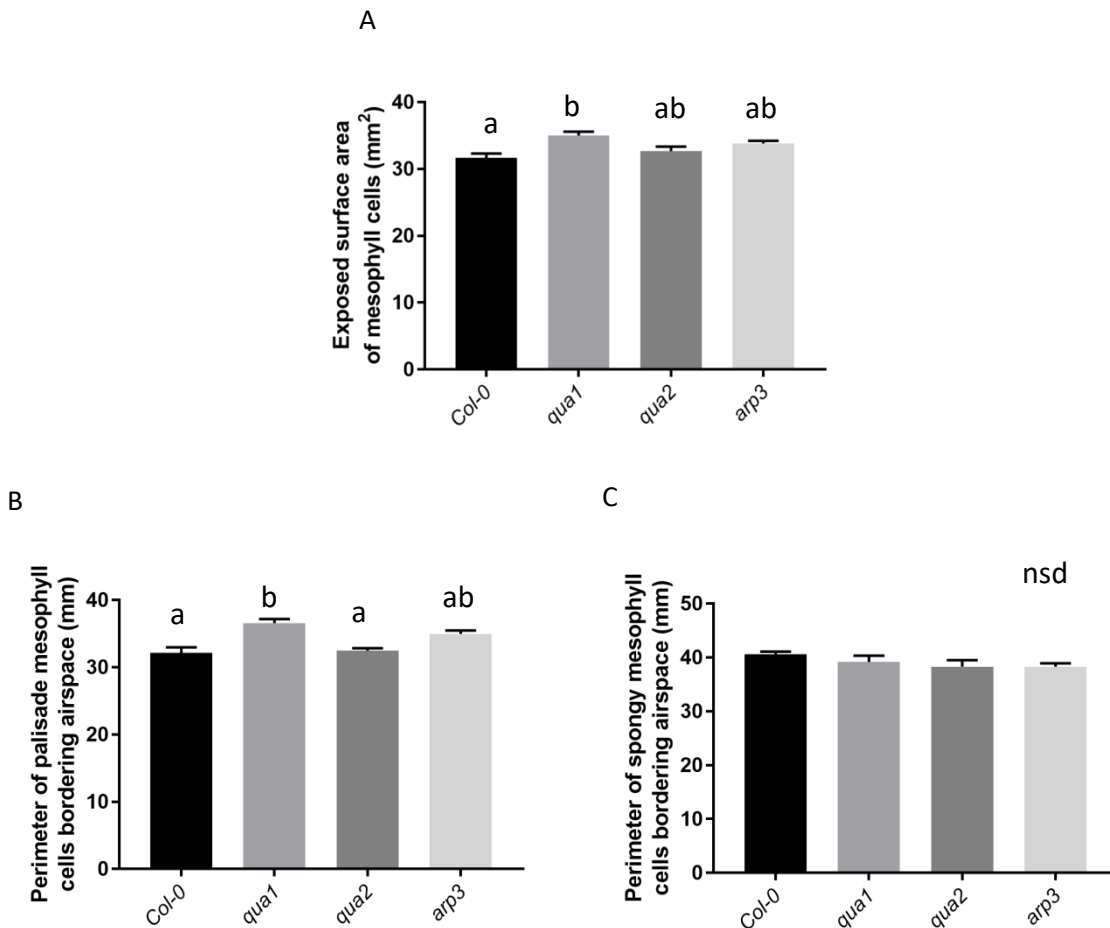


Figure 3.9: Mesophyll surface area exposed to airspace in Col-0, *arp3*, *qua1* and *qua2* leaves

(A) *qua1* had a significantly greater exposed mesophyll cell surface area than Col-0, with the other lines intermediate between these (One-way ANOVA, $F_{(3,14)}=5.91$, $P=0.008$).

For separate palisade and spongy layer analyses, the total perimeter of airspace in single representative slices was compared.

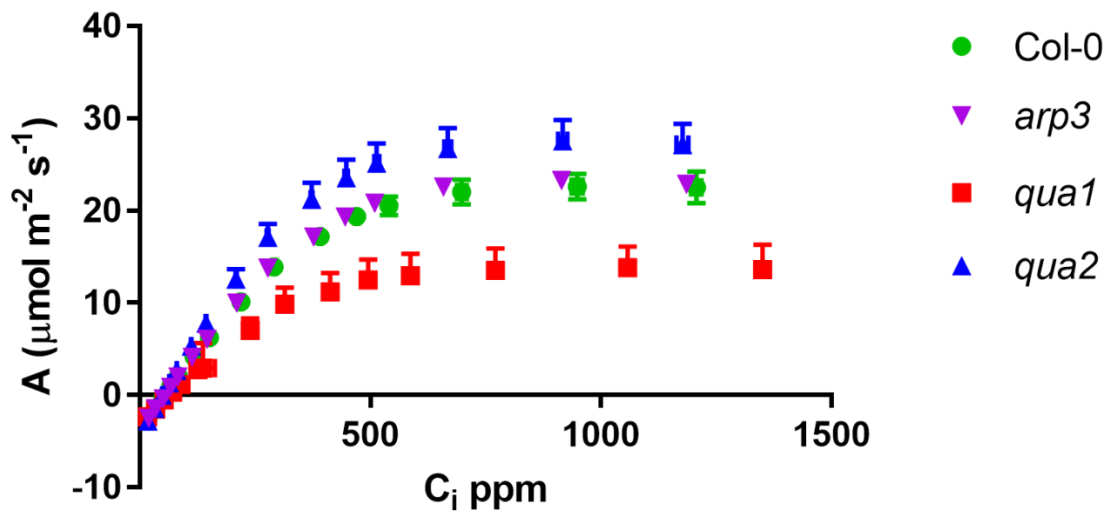
(B) The perimeter of channels in the *qua1* palisade tissue was significantly greater than that in Col-0 and *qua2* (One-way ANOVA, $F_{(3,14)}=11.85$, $P=0.0004$).

(C) There were no significant differences in exposed surface area in the spongy mesophyll (One-way ANOVA, $F_{(3,14)}=1.21$, $P=0.343$).

These data are derived from microCT images from 1.1mm² leaf regions. All error bars represent the standard error of the mean. N=5 except for *arp3* where N=3

Letters indicate groups of lines that are not significantly different from one another according to the post-hoc Tukey test ($p<0.05$).

A



B

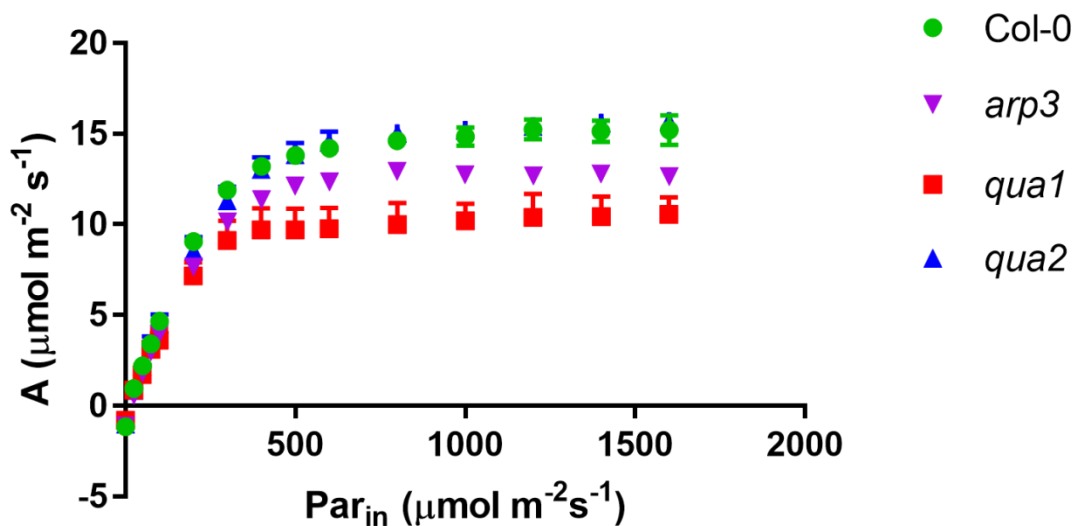


Figure 3.10: CO₂ and light response curves of Col-0, *arp3*, *qua1* and *qua2*

(A) The *qua1* plants had a reduced rate of photosynthesis at all values of C_i, and conversely *qua2* had increased photosynthetic rates. *arp3* responded to changes in CO₂ concentration similarly to Col-0. For CO₂ response curves N=4 for Col-0 and *arp3*, and N=5 for both *qua* mutants.

(B) *qua1* had reduced maximum photosynthetic rate under saturating light. *arp3* plateaued at a lower photosynthetic rate than Col-0, but not as low as *qua1*. *qua2* behaved very similarly to wildtype. For light curves, N=2 except for *qua1* where N=3.

All error bars represent the standard error of the mean.

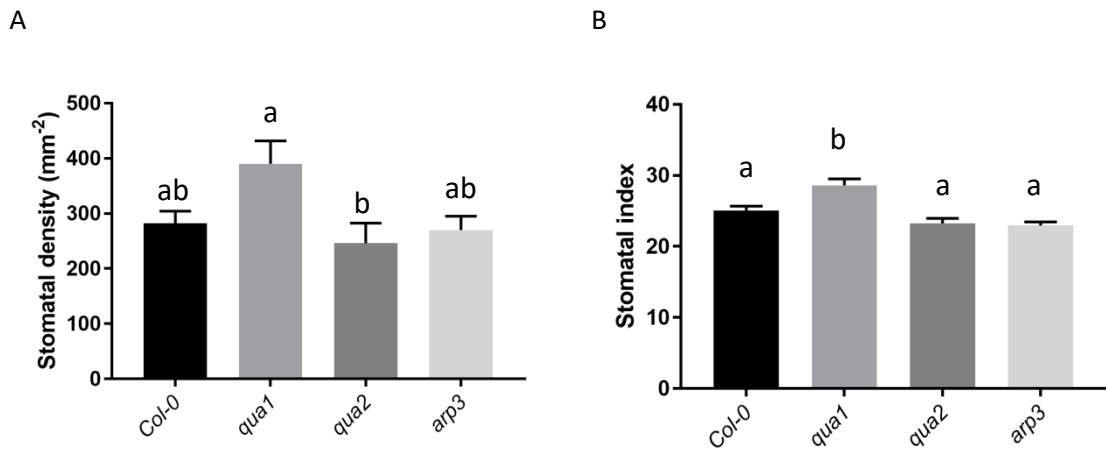


Figure 3.11: Stomatal density and index of Col-0, *qua1*, *qua 2* and *arp3* leaves

(A) Stomatal density differed between lines (One-way ANOVA, $F_{(3,20)}=3.91$, $P=0.024$), though only the *qua1* and *qua2* lines showed a significant difference in the post-hoc test ($p<0.05$).

(B) Stomatal index showed more significant variation between lines than stomatal density (One-way ANOVA, $F_{(3,20)}=13.56$, $P<0.0001$). The post-hoc test showed that *qua1* was significantly different to each of the other lines ($p<0.05$).

$N=6$ for all lines. Stomatal and epidermal cell counts were conducted on the abaxial leaf surface only. All error bars represent the standard error of the mean. Letters indicate groups of lines that are not significantly different from one another according to the post-hoc Tukey test ($p<0.05$).

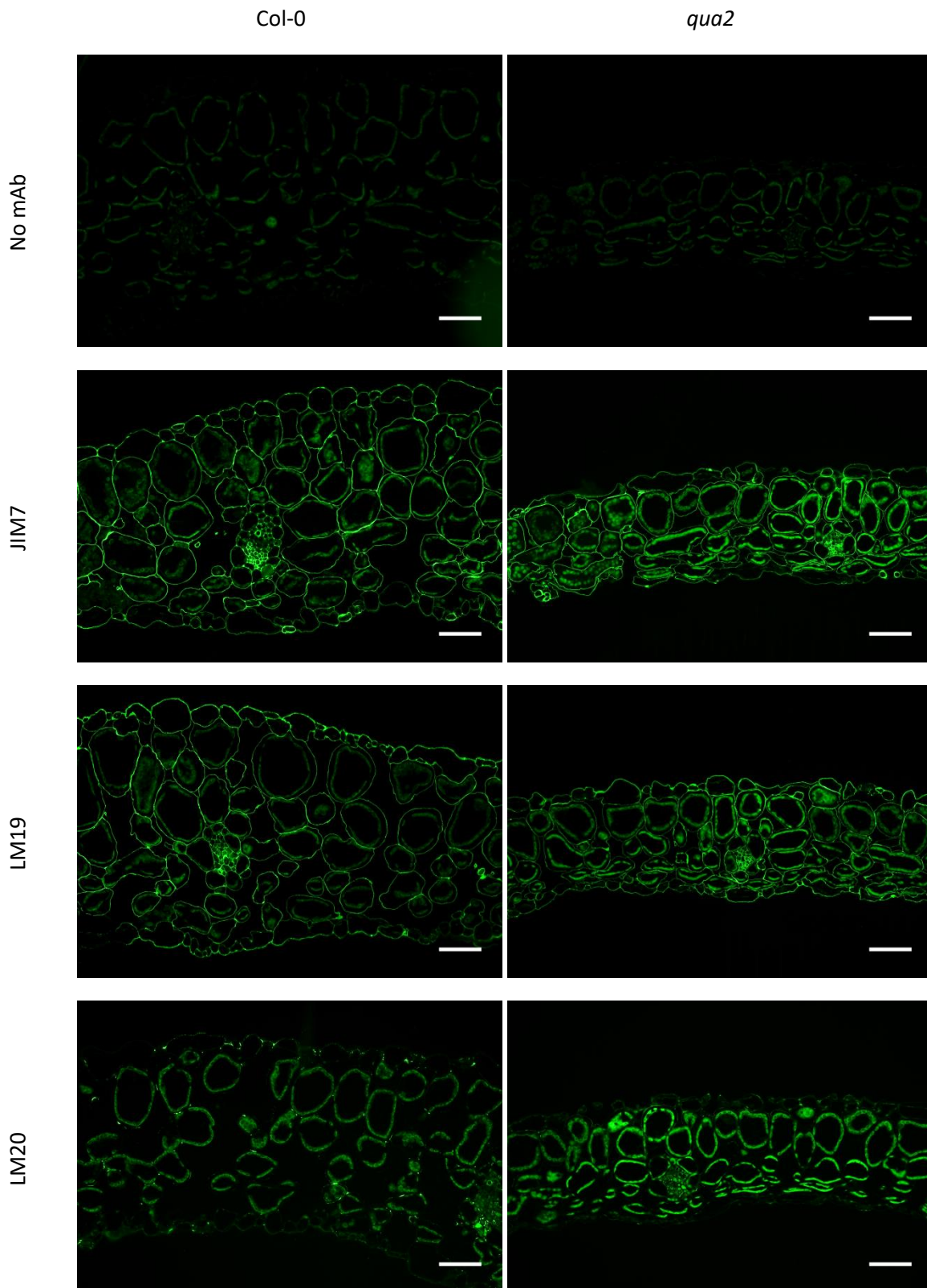


Figure 3.12: *qua2* anti-HG immunolabelling

Immunolabelling of the *qua2* mutant with JIM7, LM19 and LM20 anti-HG mAbs revealed no clear differences compared to Col-0 plants, although in this experiment both the *qua2* mutant and the Col-0 control showed less binding of LM20 compared to previous observations of Col-0. The samples appear different thicknesses, in contrast to the comparison by microCT. This could be due to leaves of less comparable sizes being selected for embedding, given the notable variation in *qua2* growth. Scale bars represent 50µm. (Note: immunolabelling of the *qua2* mutant was carried out by Alexandros Phokas).

3.2.4 Characterisation of *arp3*, a putative pectin localisation mutant

3.2.4.1 Growth on compost and microCT imaging

We obtained a mutant line in the *ARP3* gene, which we grew for five weeks on compost. The *arp3* plants grew to a similar overall size to Col-0, but had a greater leaf width to length ratio under our growth conditions (**Figure 3.7**). MicroCT scanning revealed that this mutant did not differ significantly from wildtype overall, or in its spongy or palisade layer, in any of the parameters measured (**Figure 3.8**, **Figure 3.9**).

3.2.4.2 Gas exchange analysis and stomatal characteristics

Our gas exchange analysis showed that *arp3* mutants responded to changes in CO₂ concentration similarly to Col-0 (**Figure 3.10-A**) but appeared unable to utilise high levels of light as fully (**Figure 3.10-B**). Examining the changes in stomatal conductance over the course of the light curve revealed that the *arp3* mutant had lower stomatal conductance at high light compared to wildtype (data not shown). Over the course of the A- C_i curve, *arp3* conductance was slightly lower than Col-0, with both converging at the very highest CO₂ concentrations (data not shown). Critically, the *arp3* stomatal conductance at ambient CO₂ (the condition under which the light curve was performed) was reduced, suggesting that the lower light-saturated assimilation value observed was due to CO₂ limitation. This suggests that *arp3* stomata respond differently to CO₂ concentration changes compared to Col-0.

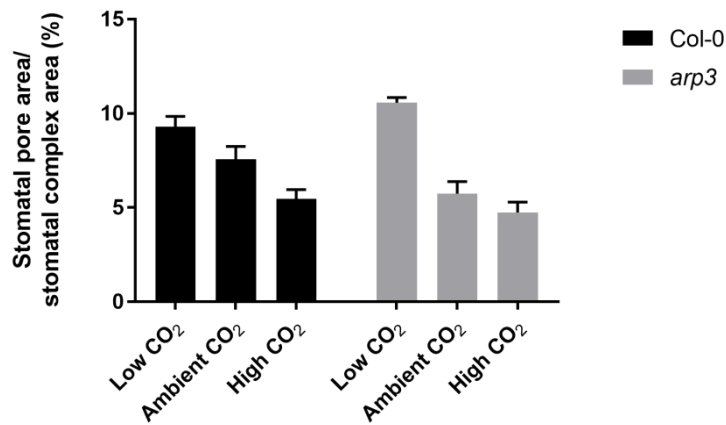
We further investigated the *arp3* stomatal CO₂ response phenotype by performing a bioassay on epidermal peels (**Figure 3.13-A**). These data supported the idea that the reduced stomatal conductance at ambient CO₂ observed in the LICOR experiment could be due to a reduced stomatal aperture under these conditions, although the observed difference was not statistically significant. The *arp3* stomata also seemed to have a greater maximum aperture under low CO₂ conditions; indeed the only statistically significant difference in the data set was between *arp3* stomata under ambient and low CO₂ treatments. This experiment needs to be repeated with a greater sample size to statistically confirm the patterns observed. Even before measuring the dimensions of the stomata, the shape change in this mutant was strikingly different to Col-0, with many stomata appearing extremely bowed outwards when induced to open by low CO₂ levels (**Figure 3.13-B**).

Stomatal density and index checks revealed no significant difference in *arp3* density or index compared to Col-0 (**Figure 3.11-A,B**).

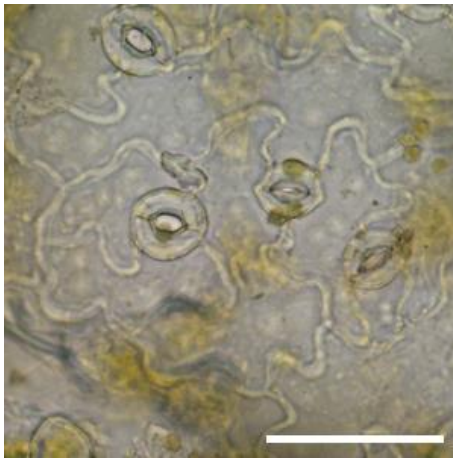
3.2.4.3 Immunolabelling

We investigated the effect of the *arp3* mutation on pectin epitope patterns using an immunolabelling approach. The data suggested that the *arp3* mutant may have less of the LM20 epitope (highly methylesterified HG), usually observed at reinforcing zones at mesophyll airspace corners, compared to Col-0 (**Figure 3.14**). Previous data from stem tissue suggested that the levels of demethylesterified pectin are reduced (Firas Bou Daher, unpublished data), but we did not see a clear change in LM19 or JIM7 binding in these leaf sections. Some large areas of signal were detected with all three anti-HG mAbs at the epidermis, perhaps suggesting a defect in cuticle formation, or possibly related to the previously reported misshapen (less lobed) epidermal cell phenotype (Li et al. 2003).

A



B



Col-0

*arp3***Figure 3.13: *arp3* CO₂ response bioassay**

(A) The stomata of the *arp3* mutant were less open than those of Col-0 under ambient CO₂, and attained a greater maximum opening under low CO₂. Statistical tests confirmed a significant effect of CO₂ treatment and a significant interaction between CO₂ treatment and genotype, but did not detect the differences between the lines (Two-way ANOVA: Genotype $F_{(1)}=1.01$ $P=0.324$; CO₂ treatment $F_{(2)}=31.93$, $P<0.001$; Interaction $F_{(2)}=3.83$, $P=0.033$). Planned post-hoc Tukey tests confirmed a significant difference between *arp3* low and ambient CO₂ treatments only ($P<0.001$).

(B) Representative images of Col-0 and *arp3* stomata in epidermal peels exposed to the low CO₂ treatment in the bioassay. The stomata of *arp3* had a distinctive, bulging shape. Scale bars represent 50 μ m. (Note: these bioassays were carried out by Sarah Carroll)

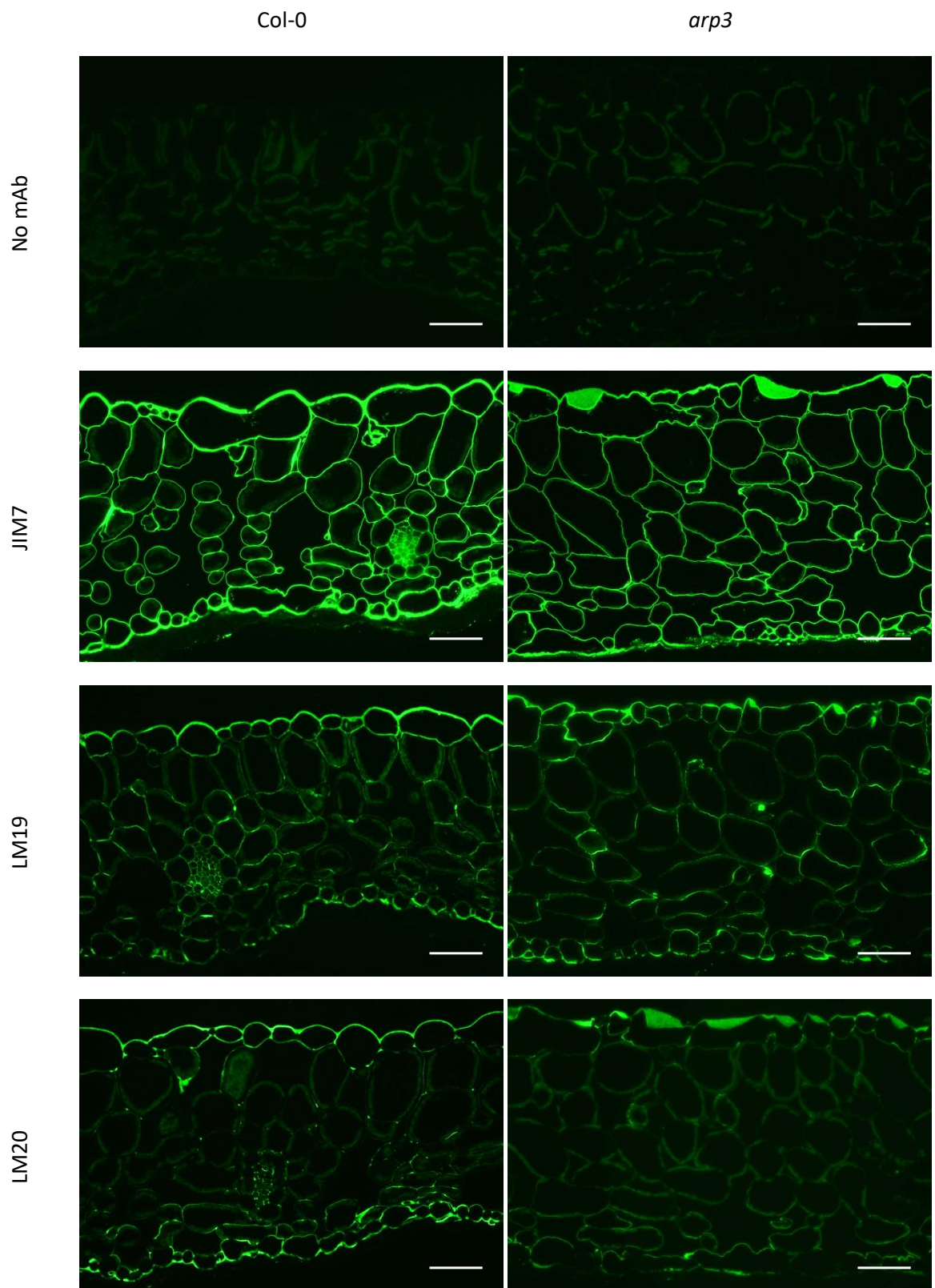


Figure 3.14: *arp3* anti-HG immunolabelling

Immunolabelling suggested that the HG distribution of the *arp3* mutant is similar to that of Col-0, although less LM20 signal was detected in this mutant. *arp3* appears to have some large pectin deposits at the epidermis that are not observed in Col-0. Scale bars represent 50µm.

3.3 Discussion

In this chapter we aimed to find and characterise mutants with altered pectin methylesterification levels or a change in total pectin. We hypothesised that altered expression of genes encoding these activities would lead to alterations in leaf cellular architecture, and that this in turn would affect the physiology of the leaves.

3.3.1 Altering PME activity *in muro*

We took a dual approach to try to downregulate pectin demethylesterification *in muro*, generating *PMEI* overexpression lines and investigating insertional mutants in *PME* genes. We used an immunolabelling-based screening approach to identify mutants of interest.

The *PMEI* lines that we generated under the pCA1 promoter had no effect on the localisation of pectin epitopes as reported by the JIM7, LM19 and LM20 mAbs. This could be due to failure of the lines to reduce PME activity, or could simply indicate that any increase in methyl pectin was not of sufficient magnitude to cause a detectable change in epitope pattern. As other more promising mutants were emerging for analysis, expression checks were not pursued at the RNA or protein level, though previous successful expression of the two *AtPMEI* coding sequences under the 35S promoter suggest that any differences in our lines may be due to the pCa1 promoter acting less strongly. Furthermore, the 35S::*PMEI* lines previously reported showed only a 16% elevation in pectin methylesterification in extracted cell wall material and no obvious effects on gross phenotype other than an increase in root length; it is possible that these mutants would also show no striking change in the localisation pattern of pectin epitopes (Lionetti et al. 2007).

While high expression of a gene is not necessarily indicative of high activity, we were successful in discovering a dramatic decrease in LM19 epitope level in the *pme3* mesophyll on this basis. *PME3* interacts with the *PMEI1* and *PMEI2* proteins overexpressed in our transgenic lines, providing further evidence that the transgenic *PMEI* overexpression lines that we generated have a far-from-comprehensive effect on reducing PME activity as they do not recapitulate the *pme3* LM19-labelling phenotype (Lionetti et al. 2007). Reduced demethylesterified pectin content (reported by Pam1 antibody signal) has been observed in *pme3* wall extract, and this was related to a reduction in cell adhesion which improved the efficiency of mesophyll protoplasting (Lionetti et al. 2014). Raiola et al. (2011) measured a 40% increase in pectin methylesterification in *pme3* wall extracts, and also showed an increase in both Pam1 and JIM5 antibody binding in immunodot assays. It would be informative to see whether JIM5 and Pam1 labelling of *pme3* leaf sections showed a spatial element, in addition to the reported change in abundance of these epitopes, relative to Col-0. A further study using Pam1 as a proxy for pectin methylesterification in wall extracts showed that Pam1 levels in

pme3 wall extracts were well within observed natural variation among *Arabidopsis* accessions, although *qua2*, also included in the study, showed Pam1 levels below even the most extreme natural variants (Francocci et al. 2013). Some of the natural variants identified by Francocci et al. (2013) might make useful additions to our mutant collection for investigating the effect of the cell wall on leaf cellular architecture, although it might be difficult to disentangle any pectin methylesterification effects from other possible varied aspects of their phenotypes. Overall these data suggests that future investigation of the *pme3* cellular architecture may reveal reduced adhesion and thus altered airspace in the leaf.

While our immunolabelling approach did not show changes in the distribution of different pectin epitopes in *qua2* mutant walls, alterations in the quantity of pectin in the *qua* mutants are well established in the literature, and there is some unpublished evidence of cell wall differences in the *arp3* mutant (Firas Bou Daher, unpublished data), though more detailed characterisation of these changes would be valuable. Our immunolabelling of *arp3* leaves suggested a reduction in highly methylesterified HG, which localises to airspace corners in Col-0 plants. This result was in contrast (though not necessarily contradictory) to the previous, unpublished observations, which suggested an effect of the *arp3* mutation on demethylesterified HG levels.

A suite of mutants that vary in either their pectin quality (e.g. *pme3*) or pectin quantity (e.g. the *quas*) provides a useful tool for investigating the relative importance of these two factors. Existing evidence in the literature suggests that either can be critical, independently of the other, depending on the context. For example Bethke et al. (2014), report that changes in pectin quality in *pme41* mutant plants are detrimental to pathogen defence, whereas changes in total pectin had no effect on resistance. In contrast, Daher & Braybrook (2015) point to the *qua2* reduced cell adhesion phenotype as an example of the importance of overall pectin level.

3.3.2 Investigating the mesophyll cellular architecture of cell wall mutants

While the structure of the *pme3* mutant has not yet been analysed by microCT, the *qua* mutants and *arp3* were investigated in detail.

We did not find evidence for reduced mesophyll cell adhesion in the *arp3* mutant. Cell detachment has been reported in the hypocotyl of mutants in ARP2/3 complex genes (Mathur et al. 2003), but other tissues studied have normal cell adhesion in these mutants. No aberrant cell separation has been reported in the *arp3* leaf epidermis, but it does display distorted trichomes and reduced lobing of epidermal pavement cells. Although we showed that the mesophyll structure is not unusual with respect to its airspace distribution, it would be interesting to examine mesophyll cell shapes to see if they too are more regular in their 3D

outline. MicroCT imaging is unable to distinguish individual cell outlines, so a confocal microscopy approach would be a more appropriate method for testing this idea.

The two pectin biosynthesis mutants, *qua1* and *qua2*, both showed an increased porosity relative to Col-0, consistent with published evidence that they have reduced cell adhesion. *qua2* showed the more extreme porosity increase, which may relate to the greater HG reduction in this line (50% HG reduction in *qua2* (Mouille et al. 2007); 25% HG reduction in *qua1* (Orfila et al. 2005)). Mouille et al. (2007) note that the phenotypes of *qua1* and *qua2* are similar in a number of respects including dwarf stature, reduced cell adhesion and reduced GalA (galacturonic acid) content, although the enzymes that they encode have different activities in the pectin biosynthesis pathway. While we selected these mutants for characterisation based on both their altered pectin and their reduced cell adhesion phenotypes, it remains unclear whether one of these factors directly causes the other, or whether other pectin-based changes in cell wall properties are responsible for the differences in cellular architecture that we observed. Daher & Braybrook (2015) suggest that these mutants are affected in the pectin of the middle lamella, directly interfering with adhesion, but Verger et al. (2016) recently provided evidence that the situation is more complex: in a double mutant of *qua2* and *esmd1* (an *o*-fucosyl-transferase), normal cell adhesion was restored but HG remained at the reduced level typical of *qua2*. Altered flexibility and extensibility of the primary wall (Ralet et al. 2008) and even altered cell division patterns (Frank et al. 2002) could additionally or alternatively play a role in setting leaf architecture.

3.3.3 Do changes in the cell wall lead to changes in physiology via an effect on mesophyll cellular architecture?

Given the lack of an aberrant cellular architecture phenotype in the *arp3* mutant, we did not necessarily expect to find differences in its physiological performance, and indeed the CO₂ response curve showed no difference from Col-0. However, a reduction in the maximum assimilation rate under high light at ambient CO₂ led us to observe that the *arp3* stomata behave differently from those of Col-0, both in that they are less open under ambient CO₂, and they open wider at low CO₂ concentrations. The importance of the actin cytoskeleton in stomatal movement has long been recognised (Volkman & Baluska 1999; Kim et al. 1995) and more recent work has demonstrated a specific role for the ARP2/3 complex (Li et al. 2013; Jiang et al. 2012). Previous assays of stomatal movement in *arp2* and *arp3* mutants have used light or ABA (abscisic acid) to stimulate shape change, whereas we were able to demonstrate a response to CO₂ both in epidermal peels and in live plants. Furthermore, these studies focus on aberrant vacuolar fusion behaviour in the mutants (Gao et al. 2009), and potential cell wall effects have not been investigated. Our observation that the *arp3* stomata are able to open

wider seems likely to relate to a difference in the cell wall, possibly via altered pectin composition.

The *qua1* and *qua2* mutants both showed significant differences in their physiology, although the increase in porosity in these mutants could not be the driver of physiological change in both cases since the mutations had opposite effects on photosynthesis relative to Col-0. There are many possible explanations for the compromised performance of *qua1*. Some of these are visually obvious, such as the dwarf stature of the plants, the fragile nature of the leaves when handled, and the pale leaf colour. The literature reveals others, such as disrupted vascular tissue due to a decrease in xylan synthase activity (Orfila et al. 2005). Given the range of reported and observed defects in *qua1*, the poor physiological performance of this mutant is unsurprising.

The *qua2* mutant is the more interesting of the two in the context of our study because the reason for its enhanced ability to assimilate CO₂ is not immediately obvious. Other recent work from our lab successfully demonstrated a link between cell cycle gene misexpression, leaf cellular architecture and leaf-level photosynthesis (Lehmeier et al. 2017). One line was identified in which reduced porosity led to improved photosynthesis through a combination of increased density of photosynthetic tissue and increased mesophyll conductance to CO₂ (g_m). In contrast, *qua2* has increased leaf porosity but an increase in assimilation; is this physiological change due to the changes we observed in cellular architecture, or despite them? The *qua2* line showed no significant difference in the surface area of mesophyll cells available for CO₂ uptake, so given that this factor is unchanged, perhaps the larger airspaces improve gas exchange by assisting the bulk flow of gasses through the leaf. Other untested possibilities include an improvement in light attenuation properties, though this would be surprising in a more porous leaf, or a change in the amount of chlorophyll and/or rubisco. A further intriguing possibility is that the changes in pectin structure reduce the resistance of the cell wall to CO₂ diffusion (g_{wall}) (Evans et al. 2009). We have not yet compared the biomass or seed yield of the *qua2* plant to Col-0, but this would be an interesting line of enquiry; presumably the higher pectin content in the wildtype, and linked cost to assimilation, is driven by the dwarf phenotype, conferring a greater reduction in productivity and thereby fitness at the whole plant level.

To date only one study has been published linking changes in cell wall pectin to alterations in cellular architecture and photosynthesis. Weraduwege et al. (2016) characterised previously described mutants that misexpressed *CRG* (cotton-related golgi) genes (Kim et al. 2015). An increased degree of pectin methylesterification (*CGROX2* overexpression) was found to correlate with increased airspace, decreased cell density, and increased biomass, and vice

versa. Both lines had lower levels of photosynthesis than Col-0 on an area basis, but expression on a volume basis may have made for a more useful comparison as the knockout mutant was much thinner, and this effect was therefore difficult to disentangle from the reported increase in g_m . Like *QUA2*, the *CRG* genes are predicted to encode methyltransferases, but in contrast to *qua2*, this leads to a detectable change in the degree of pectin methylesterification in the mutant cell walls. This once again raises the question of the relative importance of the amount of pectin versus quality of the pectin in terms of its pattern and/or degree of methyl esterification. Since mutants in both of these gene groups affect leaf cellular architecture and photosynthesis, we can conclude that both the quality and quantity of pectin in the leaf are important for normal mesophyll development.

3.3.4 Conclusions and future work

The work described in this chapter provides new insights into the cellular structure and function of the widely studied *qua2* mutant. These data provide a valuable addition to the small but growing body of knowledge relating cell wall properties to leaf physiology via changes in cellular architecture, and demonstrate that, in addition to the importance of the degree of pectin methylesterification (Weraduwage et al. 2016), the quantity of HG also affects leaf structure and function. Further experiments are required to explain the enhanced assimilation in *qua2* mutant leaves. While the *arp3* actin nucleation mutant was not unusual in its mesophyll structure, our results did suggest a previously overlooked role for the cell wall in its aberrant stomatal CO₂ response phenotype. Specific changes in the guard cell wall composition are yet to be defined for this mutant, but if proven would provide a novel aspect to ongoing research relating guard cell wall structure to stomatal function. Finally, we confirm that the previously described reduction in demethylesterified pectin in *pme3* mutant wall extracts corresponds to a complete loss of the epitope recognised by the LM19 mAb in the leaf mesophyll. Characterisation of this mutant using the same approach that we adopted for the other mutants described in this chapter will help to further our understanding of the interaction between pectin in the cell wall, mesophyll structure, and leaf-level physiology.

Chapter 4 The role of the cell wall in stomatal development and function

4.1 Introduction

Stomata are pores on the surface of plant organs, most notably on the leaves, that allow gasses to move between the external environment and the intercellular airspaces. The development and the dynamic movement of stomata allow regulation of gas exchange on different timescales: the density of stomata is determined during leaf development in response to the environment (see Chapter 5), and shorter-term environmental response is achieved through modulation of the stomatal aperture. Each stomate comprises a pair of guard cells, derived from the division of one guard mother cell. The middle portion of the dividing wall thickens and separates to create the pore (Zhao & Sack 1999)(**Figure 4.1**). Guard cells must have special cell wall structural properties to achieve local separation of the cell wall at the pore while maintaining contact at the guard cell tips, and to facilitate repeated movements. In this chapter we seek to identify components of the cell wall that may be involved in the differentiation of guard cells, and in maintaining adhesion between the guard cell pair in the long term.

4.1.1 Stomatal function

Adjustment of stomatal aperture allows optimisation of stomatal conductance, balancing the uptake of CO₂ for photosynthesis with the loss of water by transpiration. Stomata are able to respond to a wide range of environmental cues to achieve this, including temperature, humidity, light quality and quantity, and atmospheric CO₂. Stomatal conductance is also influenced by the circadian rhythm of the plant and other endogenous signals, including Ca²⁺ signalling and the concentration of the growth hormone ABA (abscisic acid) (Assmann & Jegla 2016). Stomatal movement is driven by modulation of the turgor pressure within the guard cells. Changes in guard cell water potential, caused by redistribution of cations, lead to water influx or efflux, which respectively increase or decrease the cell volume, thereby distorting the shape (Franks et al. 2001).

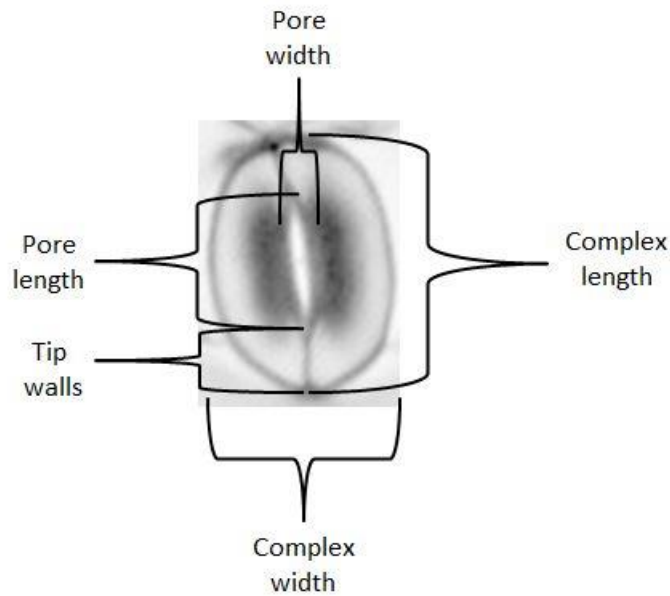


Figure 4.1: Key stomatal dimensions

Changes in stomatal pore area are calculated from measurements of the length and width of the pore (see Materials and Methods). This is normalised for differences in stomatal size by dividing by the stomatal complex area, which is calculated in the same way. We refer to the adhered guard cell walls on either side of the pore as the tip walls.

4.1.2 Stomatal cell walls

Once a cell has been determined as a guard mother cell (see Chapter 5 for stomatal patterning) it must divide and differentiate to form a pair of specialised guard cells. Development of a functional stomatal pore relies on highly controlled cell separation. The middle lamella between the two guard cells must be largely broken down, but at the tip walls it must remain intact. Despite the clear importance of this stage of stomatal development, nothing is known about the components of the cell wall that facilitate the change.

Other aspects of the stomatal cell wall have received a little more attention, particularly those involved in the dynamic stomatal shape changes that allow rapid and sensitive environmental response. The importance of the radial arrangement of cellulose microfibrils has long been recognised, and the pectic polymers arabinan and homogalacturonan (HG) have also both been implicated in stomatal movement by modulation of cell wall flexibility (Jones et al. 2003; Amsbury et al. 2016). Guard cell walls are asymmetrically thickened, with the thicker inner wall around the pore. This has long been thought to contribute to forcing the guard cells to bow outwards when turgor pressure increases, but recent modelling work challenges this assumption (Carter et al. 2017). Furthermore, the waxy, hydrophobic cuticle on the leaf

surface protrudes over the stomatal pore, forming a structure called the cuticular ledge. This may be involved in preventing pathogens and/or water droplets from entering through the stomata, and in 'sealing' the stomata when they are fully closed to prevent water loss (Li et al. 2007).

One unusual feature of stomatal cells is that they are not connected to non-stomatal cells by plasmodesmata. These channels cross most plant cell walls to provide symplastic continuity between cells. The two guard cells are thought to be symplastically connected by plasmodesmata in the tip walls, which may be important for balanced, symmetrical stomatal shape change, but the stomata are symplastically isolated from other neighbouring cells (Willmer & Sexton 1979).

4.1.3 Aims

In this chapter we seek to identify cell wall components that may play a role in determining the appropriate pattern of adhesion and separation between the stomatal guard cells. Using enzyme treatments and genetic approaches, we investigate the effects of removal of specific cell wall components on stomatal CO₂ response and mechanical properties.

4.2 Results

4.2.1 Identifying cell wall components potentially regulating guard cell adhesion

Previous work in our research group focussed on identifying cell wall components with a role in guard cell flexibility. As in the mesophyll cell wall project (see Chapter 2), this investigation began with an immunological screen of transverse sections of Arabidopsis leaf tissue using a panel of monoclonal antibodies (mAbs) (Amsbury et al. 2016). Stomata are easy to locate in the transverse view, and the thickened inner wall around the pore is clearly visible. However, from this viewing angle it is almost impossible to locate the adhered tip walls (**Figure 4.1**) and to compare them with the separated walls around the pore. We repeated a sub-set of the immunological screen on paradermal sections of stomata as only the binding of anti-HG mAbs JIM7, LM19 and LM20 had previously been examined in this orientation.

Similarly to the original screen, we found that many of the antibodies tested did not bind to any region of the stomatal cell wall (**Table 4-1**). As we previously reported (Amsbury et al. 2016), JIM7 bound throughout the guard cell and epidermal pavement cell walls, while LM20 was excluded from stomata and LM19 was localised to the ends and tip walls but absent from the walls of the pore aperture (**Figure 4.2**). Other anti-pectin mAbs also bound, for example we observed faint LM18 signal in a similar pattern to LM19 in some stomata (data not shown). Both of these mAbs bind subtly different epitopes of demethylesterified HG. The LM6 anti-arabinan mAb gave a very weak signal in all cell walls of the stomata but not in other epidermal cells (data not shown).

Very little hemicellulose was detected in untreated sections, just sparse, faint signal from both LM21 (anti-mannan) and LM25 (anti-xyloglucan), not associated with any particular cell type or region (**Figure 4.3**). The anti-hemicellulose mAbs were tested further on sections pre-treated with NaCO₃ followed either by no further treatment, CAPS buffer treatment or pectate lyase (PL) in CAPS buffer. The NaCO₃ treatment causes demethylesterification of pectin, confirmed by a reduction in the JIM7 signal. It also revealed a low level of LM15 (anti-xyloglucan) signal in some young stomata, and weak LM25 binding throughout the walls. The de-esterification by NaCO₃ allows the PL enzyme to access and degrade pectin, further unmasking the hemicellulose element of the wall. The CAPS buffer treatment showed no difference to NaCO₃ treatment alone, other than a further reduction in JIM7 signal intensity. PL treatment greatly increased the LM25 signal and slightly increased the signal from LM15 and LM24 (anti-xyloglucan). However, none of these antibodies bound in a pattern that suggested any role in adhesion or separation along the boundary between guard cell pairs.

One mAb that was not included in the original screen of transverse sections was an anti-callose antibody. Previous reports have implicated radial callose arrays in stomatal movement in some species (Peterson et al. 1975; Apostolakos et al. 2010), but instead we found that some stomata had an abundance of callose in the adhered tip wall (**Figure 4.4**). (Note: initial labelling with the anti-callose mAb was carried out on sections of the Ler Arabidopsis ecotype).

Overall these immunolabelling results suggested that demethylesterified HG and callose were both specifically localised to areas of the stomatal tip wall and were therefore candidates for a role in adhesion between the guard cell pair.

Table 4-1: Antibodies for which no binding was observed in the transverse and paradermal sections of stomata

Antibody	Binding specificity	No guard cell signal confirmed (transverse)	No signal observed (paradermal)
2F4	Calcium cross-lined HG	Y	Y
LM5	(1,4)- β -D-galactan	Y	Y
LM8	Xylogalacturonan	Only after PL treatment	Y (PL treatment not tested)
LM9	Feruloylated-(1,4)-manno-oligosaccharides	Y	Y
LM10	Xylan	Y	Y
LM11	Xylan	Y	Y
LM13	Linear (1,5)- α -L-arabinan	Y	Y
LM16	RG-I associated processed arabinan	Y	Y
LM12	Feruloylated polymers	Some signal observed	Y
LM22	Mannan	Y	Y
LM14	Arabinogalactan proteins	Some signal observed	Y
JIM16	Arabinogalactan proteins	Y	Y

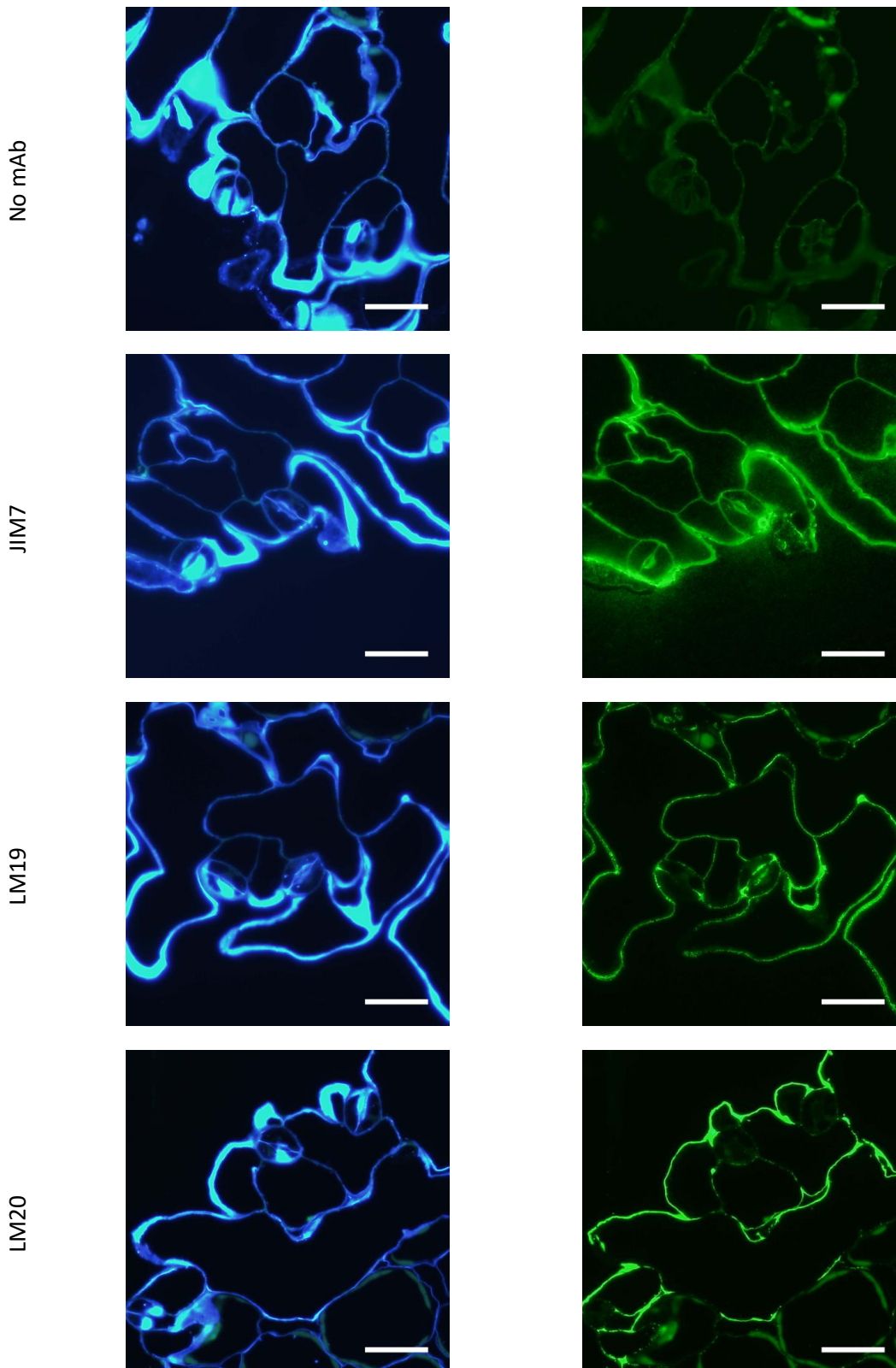


Figure 4.2: Labelling stomata with anti-pectin mAbs

The JIM7, LM19 and LM20 mAbs bind to epidermal sections as we previously reported (Amsbury et al. 2016). JIM7 and LM19 bind to demethylesterified pectin in the stomata whereas LM20 is excluded from the stomata, suggesting a lack of highly esterified pectin. Blue images (left hand side) are calcofluor stained. Green images (right hand side) show the secondary Ab signal in the same region of the section. Scale bars represent 20 μ m.

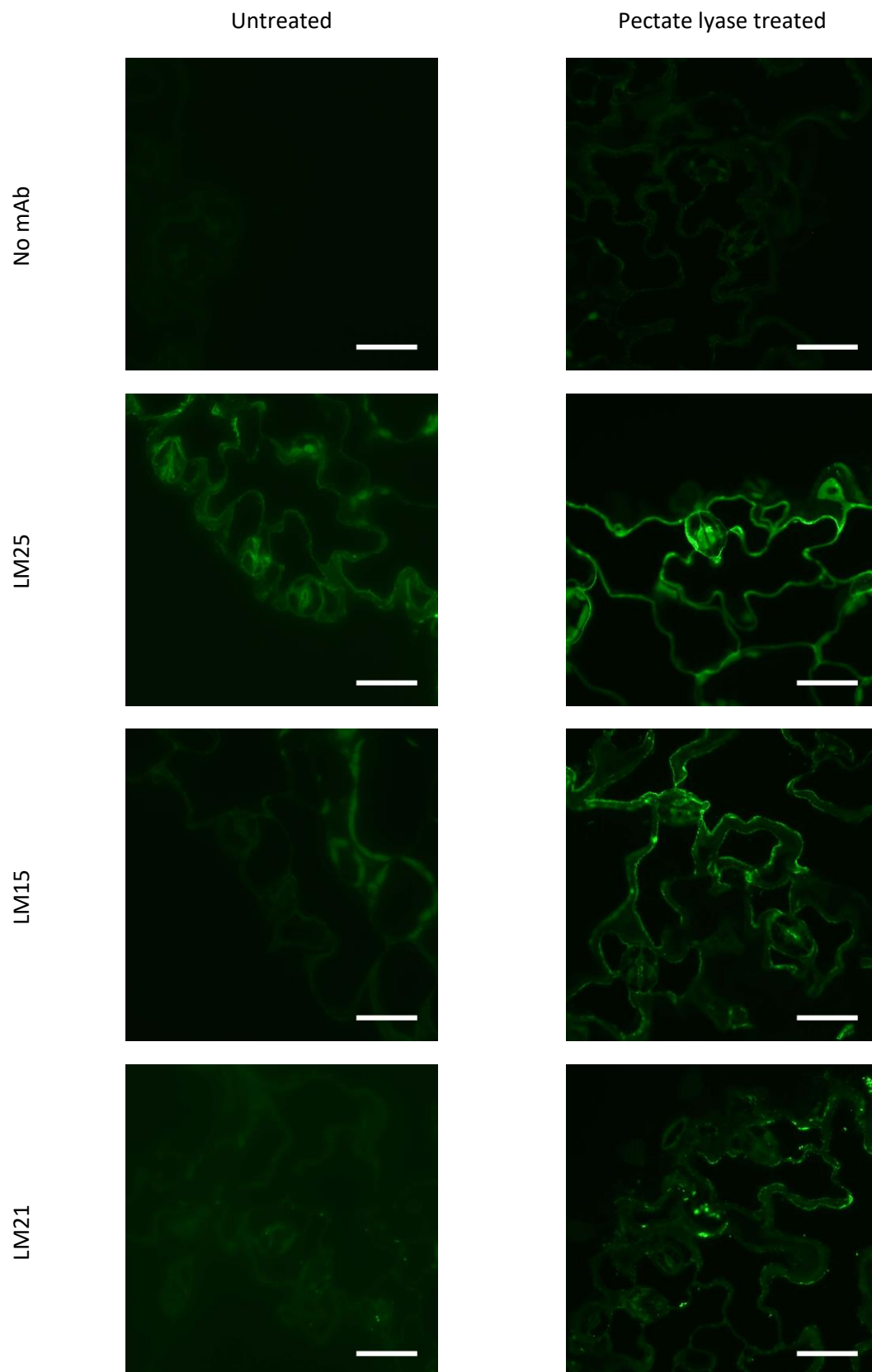


Figure 4.3: Labelling stomata with anti-hemicellulose mAbs

In untreated sections (left hand side) little hemicellulose could be detected except some xyloglucan, indicated by the faint LM25 signal. On PL-treated sections (right hand side), the LM25, LM15 and LM21 epitopes were unmasked. Scale bars represent 20 μ m.

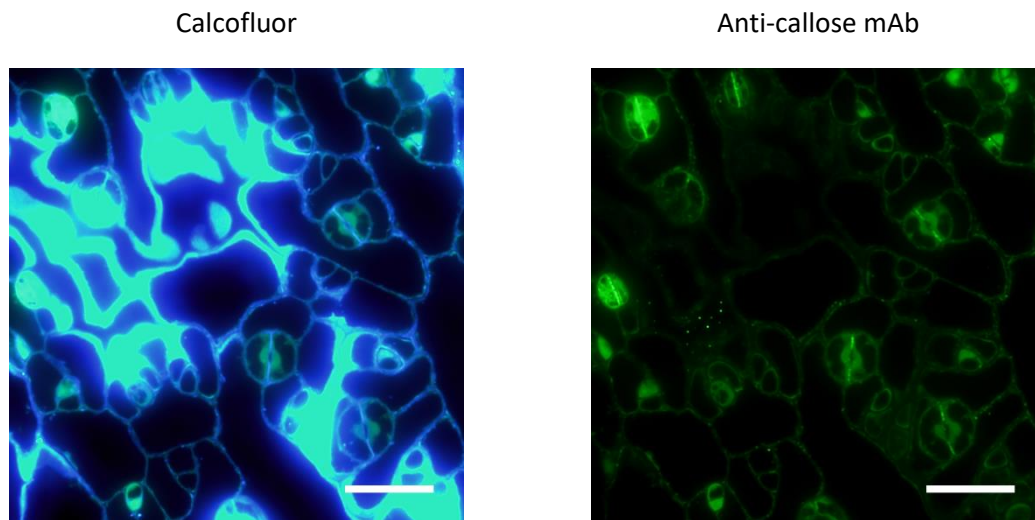


Figure 4.4: Tip walls contain callose

Stomata were labelled with an anti-callose mAb, which gave a strong signal at the tip wall of many stomata and in the new walls of dividing guard mother cells. These sections are from the Ler ecotype of *Arabidopsis* rather than the usual Col-0, but we would not expect this to affect the result, and confirmed tip wall callose localisation in Col-0 with aniline blue stain (**Figure 4.11**). The blue image (left hand side) is calcofluor stained. The green image (right hand side) shows the secondary Ab signal in the same region of the section. Scale bars represent 20 μ m.

4.2.2 Functional consequences of degrading specific cell wall components

4.2.2.1 Stomatal response to CO₂

To investigate the functional significance of stomatal pectin and callose we conducted a bioassay, measuring stomatal response to CO₂ in epidermal peels from enzyme-digested leaves of four-week old, compost-grown Col-0 *Arabidopsis* plants (**Figure 4.5-A**). Leaf samples were treated for four hours with polygalacturonase (PG) or β -(1,3)-D-glucanase to remove pectin or callose respectively from the cell walls. Control samples were treated with cellulase as a general cell wall degrading treatment, or with the buffer in which the enzymes were diluted.

Buffer-treated controls exhibited the same behaviour that we had previously observed in untreated Col-0 stomata, significantly increasing or decreasing their stomatal aperture under low or high CO₂ respectively. The cellulase-treated samples were still able to show the same pattern of response to CO₂, but the stomata were more closed than the buffer control at each CO₂ level, possibly due to reduced ability of the damaged walls to withstand and recover from changes in turgor pressure. PG-treated samples showed a very small pore area under all conditions although, interestingly, a small opening response was still observed under low CO₂. The closing response seemed to be entirely lost, but stomata were already essentially closed under ambient conditions. β -(1,3)-D-glucanase-treated stomatal apertures were the same as

buffer-treated samples at low and ambient CO₂, but the closing response was abolished by callose degradation.

We investigated the shape changes in the enzyme-treated stomata in greater depth to determine whether different regions of the stomatal wall were affected by the different treatments (**Figure 4.5-B-D**). Changes in pore length and width accounted for a very similar proportion of the total change in pore area in buffer-treated and cellulase-treated stomata. However, both PG and β -(1,3)-D-glucanase-treated stomata appeared unable to reduce their pore length or width under high CO₂.

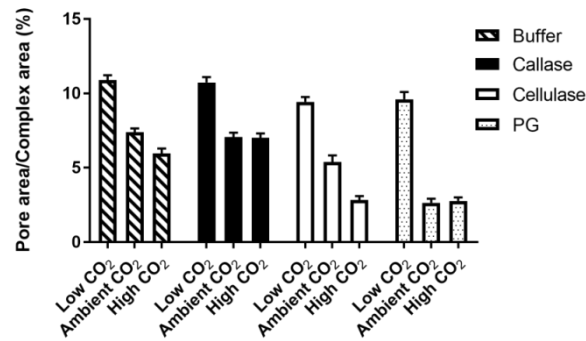
The change in pore width between CO₂ treatments caused a consistent, knock-on change of very similar magnitude in the width of the stomatal complex as a whole. In contrast, none of the treatments caused any significant difference in the total length of the stomatal complex, regardless of changes in pore length. This may suggest a change in the length of the adhered tip wall, though whether this is a 'real' expansion/contraction of this portion of the wall, or whether a change is apparent due to the separation/appression of detached cell walls, requires further investigation.

In summary, normal stomatal aperture change is a result of changes in the length and width of the pore, accompanied by a change in complex width but without altering complex length. All changes observed in control treatments under high CO₂ were abolished in the PG and β -(1,3)-D-glucanase-treated stomata. In addition, both β -(1,3)-D-glucanase-treated and PG-treated stomata exhibited less open pores under all CO₂ conditions compared to the buffer-treated control. Finally, an interesting observation on enzyme-treated samples was a slight separation of cells at the tips of some PG-treated stomata, perhaps suggesting a loss of adhesion associated with the reduction in pectin (**Figure 4.7**). This requires further investigation.

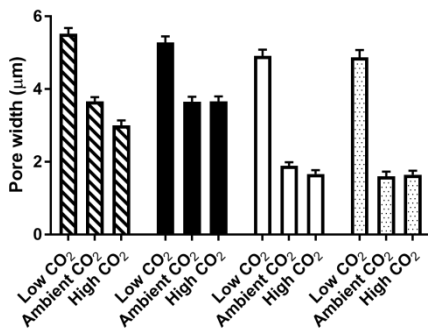
4.2.2.2 Changing the mechanical properties of the guard cells

To investigate the effect of the enzyme treatments on the mechanical properties of the stomata, leaf explants subjected to the same enzyme treatments were probed by atomic force microscopy (AFM; **Figure 4.6**). This experiment has not yet been conducted on β -(1,3)-D-glucanase-treated samples. In buffer-treated controls, we observed a point of stiffness at the poles of the stomata. This was also visible in untreated stomata, and became more pronounced as stomata matured. Cellulase treatment did not alter the pattern of stiffness in the stomata, and only slightly reduced the peak stiffness value, suggesting that this enzyme has an equal impact across the tissue. The polar points of maximum stiffness were abolished in PG-treated samples, but this change was accompanied by a great reduction in stiffness throughout guard cell and epidermal cell walls, confirming far-reaching effects of pectin removal across the epidermis.

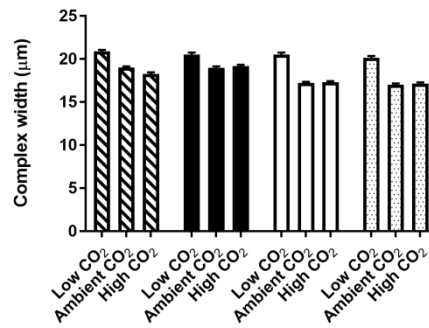
A



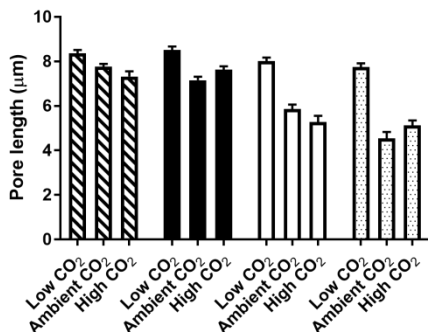
B



C



D



E

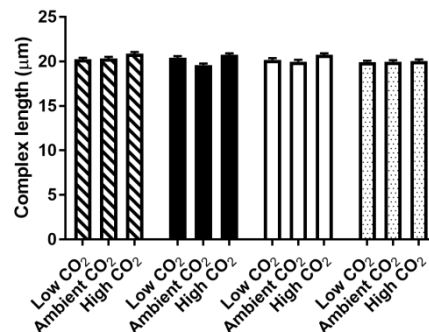
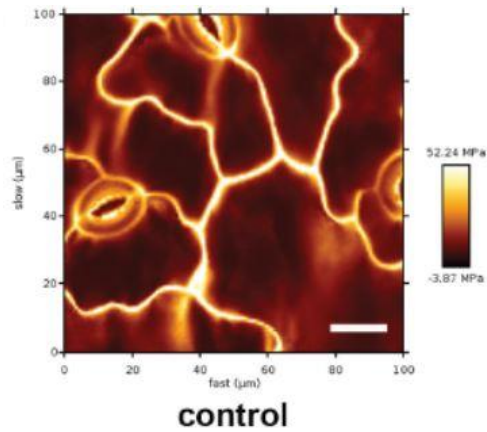


Figure 4.5: Response to CO₂ in enzyme-treated stomata

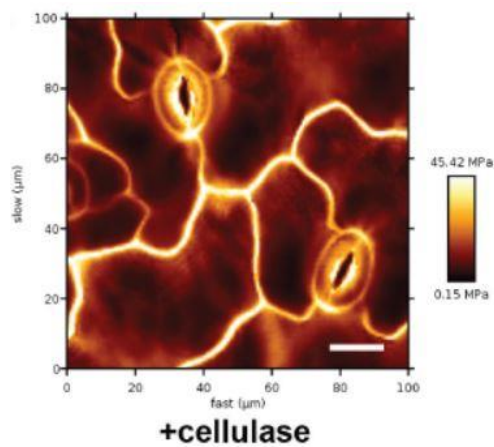
(A) Enzyme treatment of tissue altered the stomatal responses to CO₂. B-(1,3)-D-glucanase-treated stomata were unable to close in response to high CO₂. Cellulase-treated stomata responded normally to CO₂ but were less open at each CO₂ treatment than the buffer-treated control. Polygalacturonase (PG)-treated stomata were able to open but were essentially closed at ambient CO₂. (Two-way ANOVA: Pre-treatment $F_{(3)}=20.97$ $P<0.001$; CO₂ treatment $F_{(2)}=89.98$, $P<0.001$; Interaction $F_{(6)}=2.81$, $P=0.017$. Planned comparisons by Tukey HSD tests confirmed significant opening in all treatments but significant closing in cellulase-treated stomata only. Reduced aperture at ambient CO₂ after PG treatment was also significant).

(B-E) Changes in stomatal aperture in (A) were explained by changes in both pore length and pore width. The complex width changed with the stomatal aperture, but complex length was static under all treatments. (Note: these bioassays were carried out by Sarah Carroll)

A



B



C

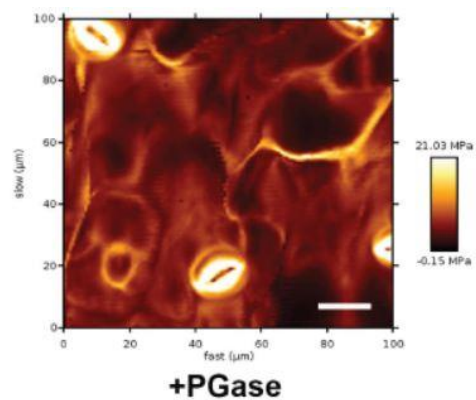


Figure 4.6: Changes in cell wall mechanical properties

(A) Imaging epidermal tissue by AFM (Atomic Force Microscopy) shows that stomata are stiffened around the pore and at the poles.

(B) Treatment of epidermal explants with cellulase reduces stiffness consistently across the tissue, so the pattern of relative stiffness is unchanged.

(C) Tissue treated with polygalacturonase (PG) exhibited a greater loss of stiffness than cellulase-treated tissue. The relative stiffness pattern was also altered. A greater loss of stiffness occurred at periclinal walls and at the stomatal poles than around the stomatal pore.

Scale bars represent 10μm. (Note: AFM was carried out by Professor Andrew Fleming)

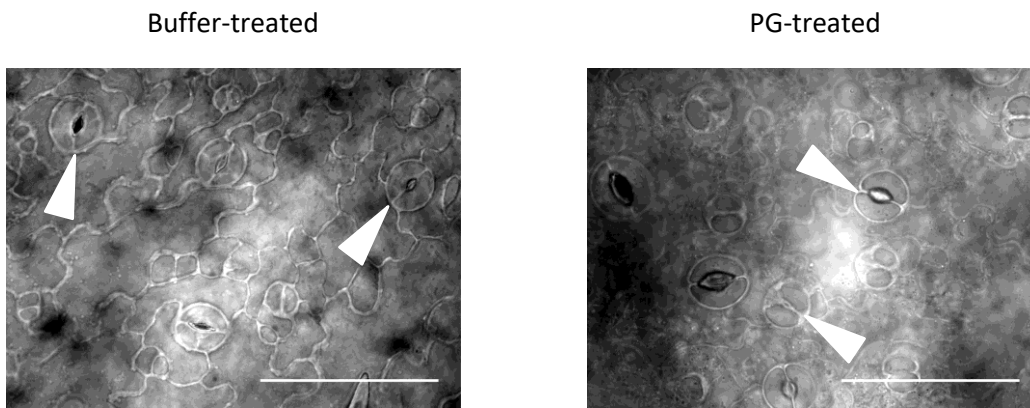


Figure 4.7: PG-treatment of stomata causes separation at poles

Leaf explants (fresh tissue) treated with polygalacturonase (PG) had a high frequency of stomata with apparent separation at the poles of the complex (indicated by arrows). Such separation of cells was not observed in buffer-treated controls, or in cellulase or β -(1,3)-D-glucanase-treated samples (data not shown). Arrows indicate the poles of exemplar stomatal complexes. Scale bars represent 50 μ m. (Note: these images were produced by Sarah Carroll)

4.2.2.3 Effects of wall-degrading enzymes on epitope localisation

We fixed, embedded and immunolabelled leaf tissue, prepared as for the bioassays and AFM, to confirm that the enzyme pre-treatments were reducing the levels of specific cell wall components as expected.

PG treatment removed the vast majority of pectin from epidermal and stomatal cell walls, but left a ring of HG around the stomatal boundary, with prominent dots at the poles. This HG localisation was detected by both JIM7 and LM19 (**Figure 4.9**). The LM20 epitope was also lost from epidermal cell walls, though it was never present in stomata of untreated controls. In addition to the anti-HG antibodies we obtained a probe, COS⁴⁸⁸ (Chitosan Oligosaccharide 488), which binds to an HG epitope with a very low degree of methylesterification (**Figure 4.10**). Mravec et al. (2014) exploited the strong, specific, reciprocal binding between chitosan (product of chitin deacetylation) and demethylesterified HG to produce this probe. COS⁴⁸⁸ consists of an oligosaccharide conjugated to a flurophore, and its resulting small size facilitates effective tissue penetration and high resolution imaging. When applied to intact leaf tissue that was untreated or buffer-treated, the probe signal appeared highly localised to the stomatal pole, reflecting the point of greatest stiffness identified in the AFM imaging. Furthermore, PG pre-treatment of equivalent samples abolished binding completely, suggesting that this probe might bind more specifically to an HG epitope of interest. However, we also tried applying the probe to fixed and resin-embedded sections of leaf tissue subjected to the same set of treatments and found that these results matched the patterns of JIM7 labelling. This suggests that the differences we initially observed with the COS⁴⁸⁸ probe were due to the use of intact tissue and lower than expected tissue penetration of COS⁴⁸⁸, rather

than to a difference in probe specificity relative to the available antibodies. It is intriguing that these polar deposits of demethylesterified HG are somehow inaccessible to the PG enzyme, in contrast to HG in other areas of the cell wall. They also match the HG pattern in the stomata of the *pme6* mutant. The genetic basis of this polar pectin demethylesterification was not pursued within the scope of this project, but the challenges of addressing this question are explored further in the discussion of this chapter.

Immunolabelling of callose in the buffer-treated sections was not successful, and a further test showed only patchy labelling in untreated Col-0 compared to the Ler sections in which we initially observed binding. However, it seems very unlikely that there is an authentic difference in callose between these two accessions, and more probable that variable results in anti-callose mAb binding were due to the very thin sections used: thicker sections are recommended for use with this probe. As this would require embedding samples in a different matrix, we used aniline blue staining as a more rapid way to examine the effectiveness of the anti-callose mAb. This showed a reduction in the amount of callose present in β -(1,3)-D-glucanase-treated leaf samples compared to the buffer control and to the other enzyme treatments, though some callose was still detected (**Figure 4.8**).

We did not attempt to quantify the reduction in cellulose in cellulase-treated samples. In immunolabelling experiments, calcofluor still bound to cellulase-treated samples, indicating incomplete removal of cellulose. However, the differences observed in the bioassay results do suggest that the cellulase treatment did alter the cell wall properties.

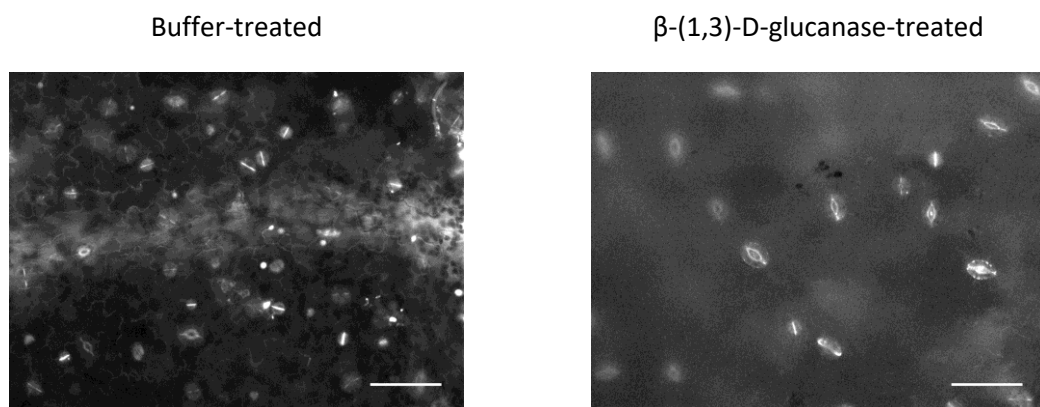


Figure 4.8: Aniline blue staining of enzyme-treated tissue

Fresh leaf tissue explants were subjected to a 4h incubation with enzyme or buffer, as for the CO₂ response bioassay, then stained overnight with aniline blue to test whether the β -(1,3)-D-glucanase treatment was effective. However, we were still able to observe callose in the tip walls of the β -(1,3)-D-glucanase-treated stomata. Samples treated with PG and cellulase were also tested to confirm that these treatments were not affecting callose distribution (data not shown). Scale bars represent 50 μ m. (Note: these images were produced by Sarah Carroll)

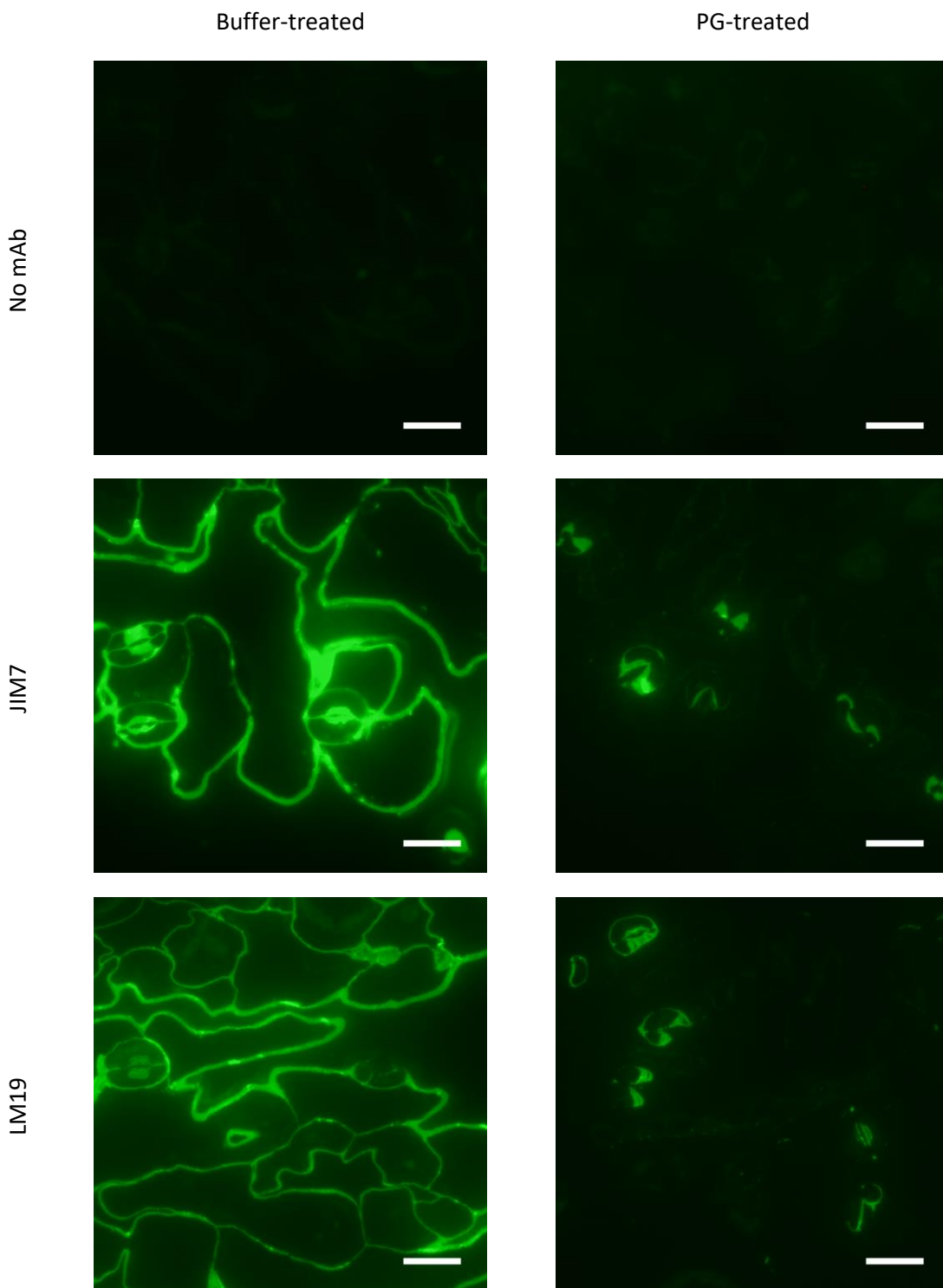


Figure 4.9: Immunolabelling of enzyme-treated tissue

Enzyme-treated explants were labelled with the anti-HG mAbs JIM7 and LM19 to check whether the PG treatment was removing pectin effectively. The results showed that some demethylesterified pectin was still present in the guard cells after treatment, although no signal was observed in other epidermal cell walls.

Samples treated with cellulase and β -(1,3)-D-glucanase were also tested to confirm that these were not affecting cell wall pectins (data not shown).

Scale bars represent 20 μ m.

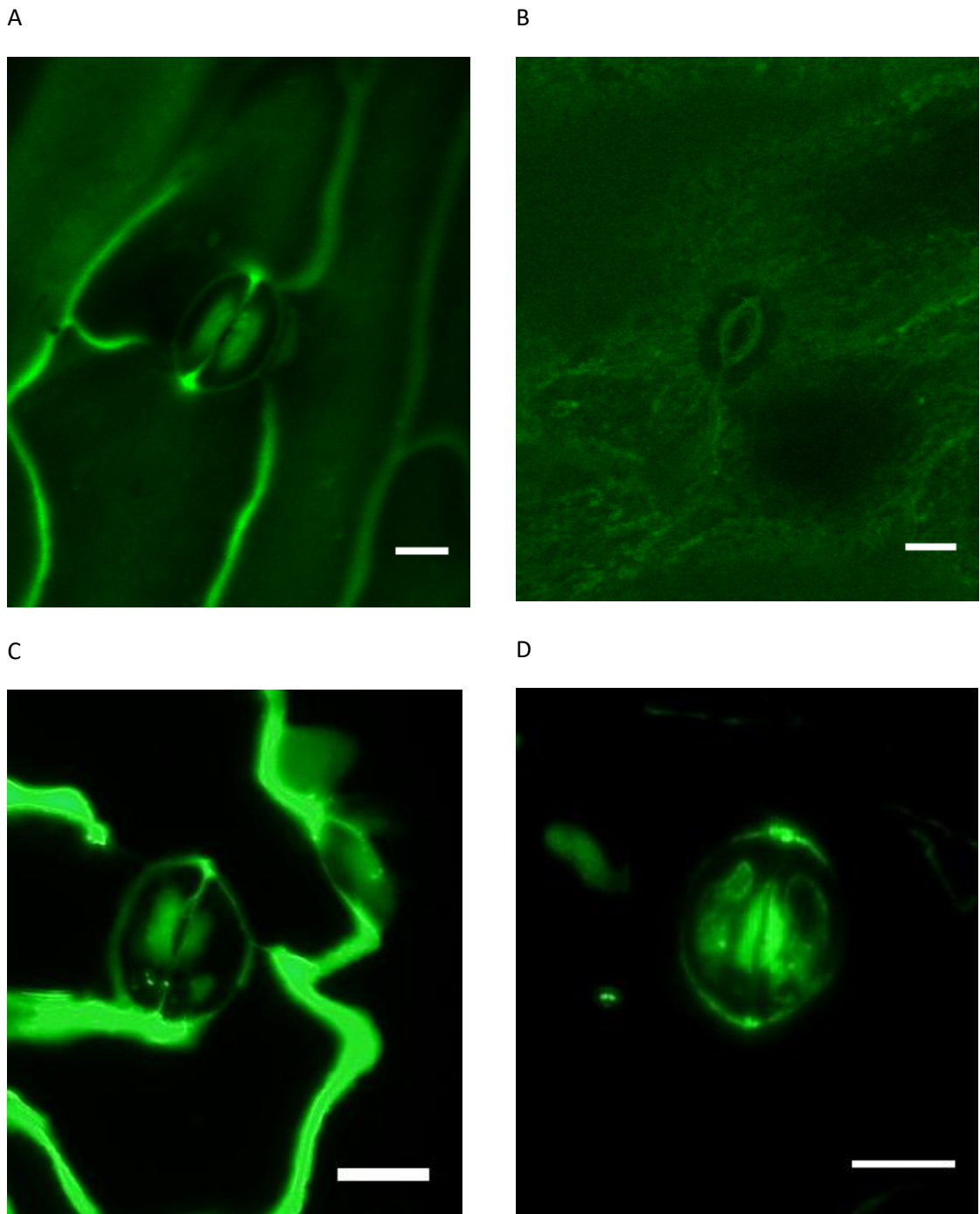


Figure 4.10: COS⁴⁸⁸ detects demethylesterified pectin in stomata

(A) The COS⁴⁸⁸ probe bound to fresh leaf tissue and gave a strong signal in pavement cell walls and stomatal poles/tip walls.

(B) Polygalacturonase (PG) treatment, conducted as for the CO₂ response bioassay, abolished all signal from the COS⁴⁸⁸ probe on fresh tissue.

(C) The COS⁴⁸⁸ probe also recognised demethylesterified pectin in fixed, resin-embedded tissue. (Note: this image was produced by Sarah Carroll)

(D) PG treatment of leaves, conducted as for the CO₂ response bioassay, prior to fixation and embedding did not abolish COS⁴⁸⁸ signal from stomatal poles in leaf sections, despite abolishing signal from epidermal pavement cell walls.

Scale bars represent 10 μm.

4.2.3 The role of callose in stomatal tip walls

4.2.3.1 Developmental changes

In the labelling and staining experiments accompanying the bioassays, we observed callose in the central walls of most divided guard mother cells, but callose appeared to be absent from many mature stomata. To investigate these differences over developmental time, we conducted a more thorough examination of changes in callose over time in compost-grown *Arabidopsis* using aniline blue staining (**Figure 4.11**). Col-0 plants were sampled each week from two to five weeks post-germination. These results clearly indicated much more staining in younger leaves of plants of all ages, and in younger stomata. In the very youngest leaves, cell plates of dividing non-stomatal cells were also apparent. Even at the two week (four-leaf) stage, the oldest stomata appeared to lack callose, and by the following week no callose was detected in the oldest leaves. However, we also observed that staining was often patchy, and that leaves of different ages stained optimally under different conditions (with/without prior ethanol fixation; different duration of aniline blue incubation). We are inclined to treat the evidence for a complete absence of staining in the oldest leaves with a degree of caution, and we plan to investigate other methods of callose detection to repeat these experiments. Decreased permeability to the aniline blue stain in more mature leaves has previously been suggested (Apostolakos et al. 2010), which could be due to development of the waxy leaf cuticle, or associated with other changes in the structure of the maturing cell wall. Furthermore, bioassays (**Figure 4.5**, **Figure 4.13**) conducted on epidermal peels from the most mature leaves of four and five week old plants did show sensitivity to callose removal, suggesting that some callose must be present.

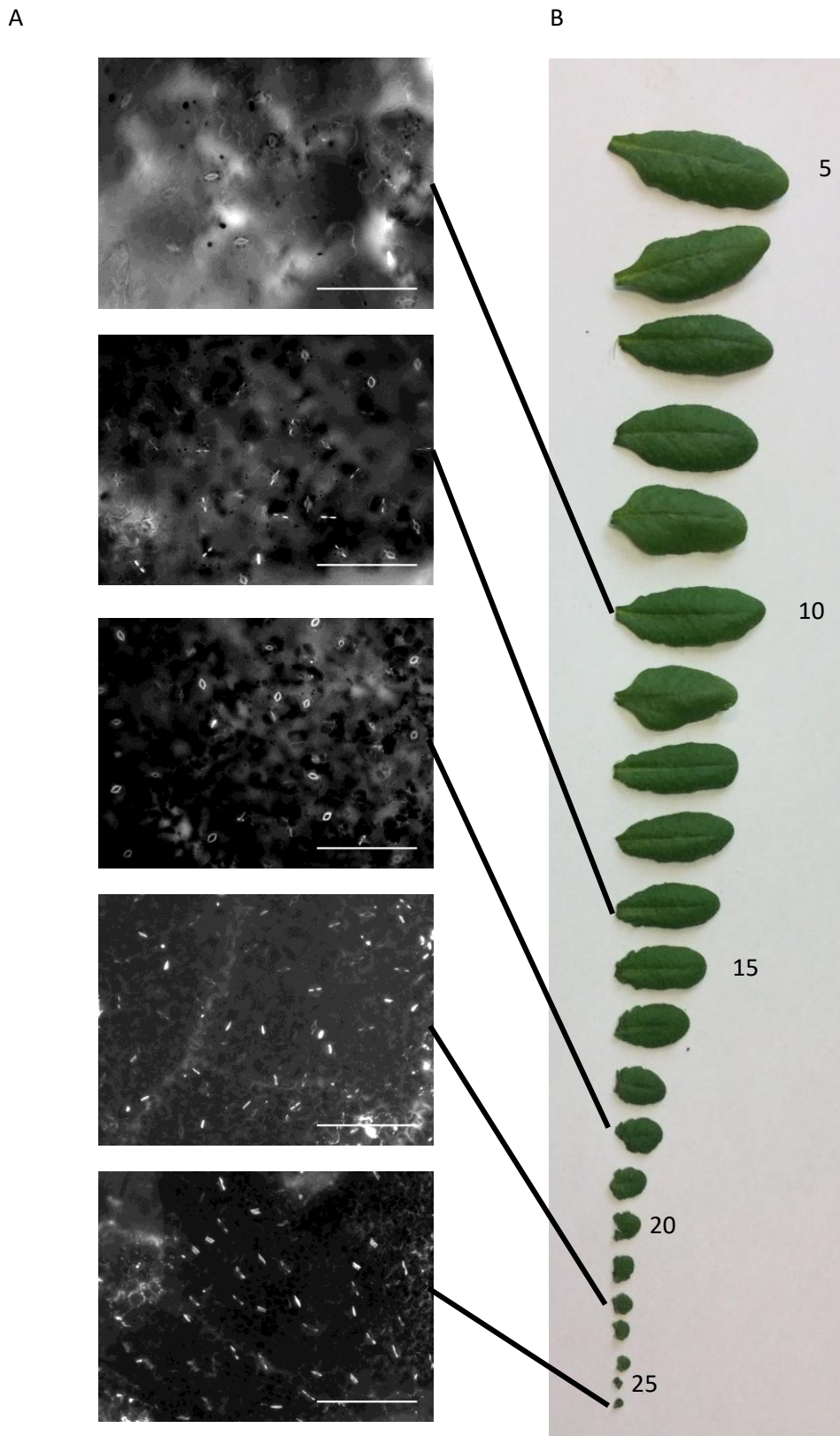


Figure 4.11: Callose localisation during leaf development

(A) Aniline blue staining of older leaves reveals almost no callose whereas younger leaves have a much higher proportion of stomata containing callose. Fresh tissue was stained overnight. Lines indicate the leaf number of each image. Scale bars represent 200 μ m.

(B) All leaves of a 5-week-old Arabidopsis, except 1-4 which were already senescing. Every 5th leaf number is indicated. (Note: these images were produced by Sarah Carroll)

4.2.3.2 Genetic manipulation of callose production

We were interested in the genetic basis of callose deposition in guard cell walls because reducing the expression of the relevant callose synthase gene(s) would allow a more refined test of the significance of callose in stomatal function than the relatively crude enzyme-treatment approach described above.

Callose synthases are encoded by *GSL* (*GLUCAN-LIKE SYNTHASE*) genes, of which there are 12 in *Arabidopsis* (Chen & Kim 2009). Sister genes *GSL8* and *GSL10* are the two most highly expressed in *Arabidopsis* (Thiele et al. 2009; Toller et al. 2008). The knockout lines that we obtained from NASC confirmed previous reports that *gsl8* and *gsl10* mutants are seedling and embryo lethal respectively (Han et al. 2014; Chen et al. 2009; Thiele et al. 2009), so knockdown mutants are a better way to examine their role in mature plants. A dexamethasone-inducible *GSL8-RNAi* mutant was obtained from the Kim lab (Han et al. 2014). In addition, we have begun making an inducible *GSL10-RNAi* construct in the pOpON2.1 vector, which is still in production.

We conducted a time series of aniline blue staining after dexamethasone induction of the *GSL8-RNAi* line to identify the time window in which the least stomatal callose was present (**Figure 4.12**). No change in staining was observed within the first four hours after application of the inducer, but after 20 hours some loss of callose was apparent, and by 24 hours very little callose remained. This low-callose state persisted for at least 10 hours, and by the final time-point, 46 hours post-induction, normal callose levels had not entirely recovered. There were insufficient seedlings available to stain further time-points. This experiment was conducted with plate-grown seedlings, 14 days post-germination, which presented some technical challenges in terms of inducing the leaves: seedlings had to be bathed in inducer, rather than painting it onto the leaves as we would to induce more mature, compost-grown plants. We intend to repeat the same test on compost-grown seedlings. Nonetheless, the loss of callose on induction of the *GSL8-RNAi* confirmed that callose is being constantly deposited and degraded at the cell wall. This is consistent with our understanding of callose dynamics in the cell plates of newly dividing plant cells.

We obtained three additional lines affected in callose synthesis (*GSL12-oex*; Vatén et al. 2011) or deposition (PdBG5/6 (Plasmodesmatal-localised β -1,3 glucanase); Benitez-Alfonso et al. 2013) but found no change in the presence of tip wall callose when these lines were examined by aniline blue staining. All three of these lines were originally reported to synthesise or regulate callose in the plasmodesmata. While the tip walls do contain these structures (unlike the outer walls of the symplastically isolated guard cells), it is perhaps unsurprising that these plants did not show a change in the level of tip wall callose.

4.2.3.3 Functional consequences of *GSL8* downregulation

Having confirmed that tip wall callose was greatly reduced 24-44 hours after induction of *GSL8-RNAi*, we conducted a bioassay to investigate the effect of this reduction in callose on stomatal function. Epidermal peels were taken 24 hours after dexamethasone induction and stomata were measured after being subjected to reduced or elevated CO₂ to trigger stomatal opening or closure respectively.

The results showed that all controls (mock-induced *GSL8-RNAi*, and induced and mock-induced Col-0) displayed a wildtype opening and closing response to high and low CO₂ respectively, but that the induced *GSL8-RNAi* stomata showed a greatly reduced closing response (**Figure 4.13**). A detailed examination of the shape changes revealed that loss of callose prevented change in all the dimensions that contribute to stomatal closure in the controls: pore length and width both failed to adjust to high CO₂ in the induced *GSL8-RNAi* line. These results are consistent with the enzyme-treated bioassay data (**Figure 4.5**).

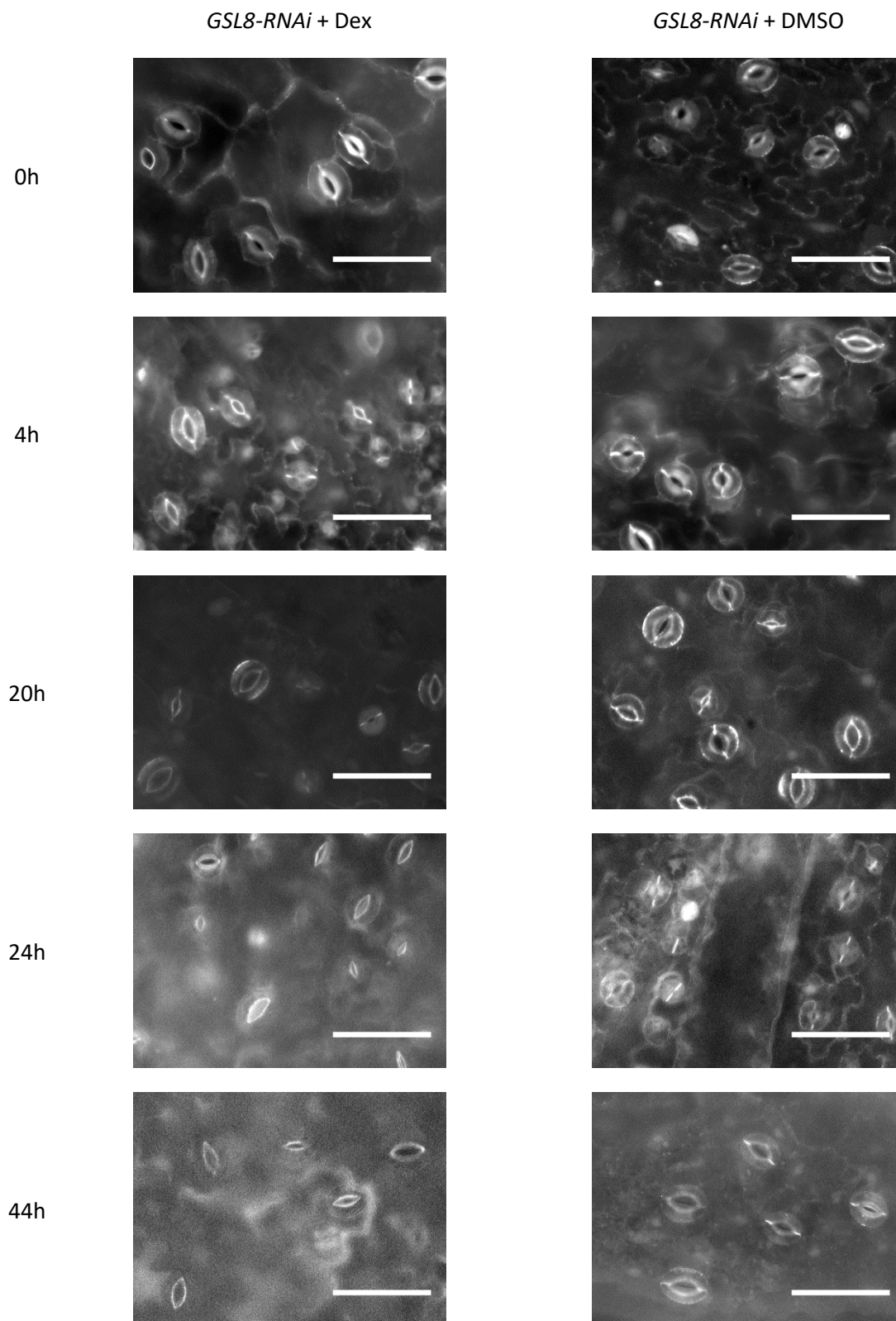


Figure 4.12 Effect of dexamethasone induction on aniline blue staining in *GSL8-RNAi*
GSL8-RNAi seedlings grown on agar plates for two weeks were induced with dexamethasone or mock-induced with DMSO and sampled periodically for aniline blue staining. A reduction in callose in the joined tip walls of the stomata was evident from 20 hours post-induction, despite persistent autofluorescence around the stomatal pore. The same treatments were applied to Col-0 leaves as a further control. These behaved the same as the mock-induced *GSL8-RNAi* plants, as expected (data not shown). Scale bars represent 50 μ m. (Note: the induction assay was carried out by Sarah Carroll)

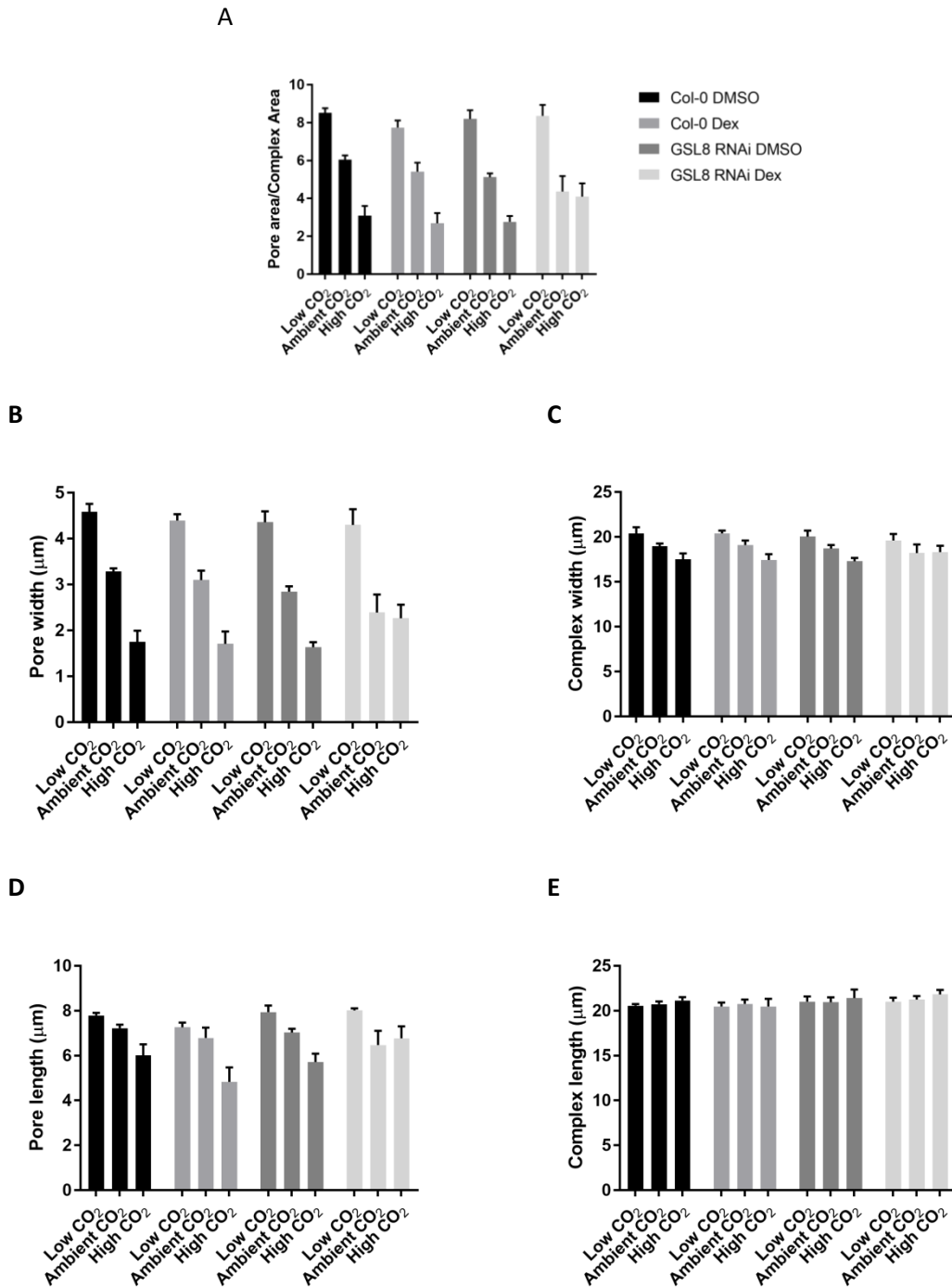


Figure 4.13: Response to CO₂ in induced *GSL8-RNAi* plants

(A) Induced *GSL8-RNAi* plants were unable to reduce their stomatal aperture in response to high CO₂, in contrast to all controls. (Two-way ANOVA: Line/treatment $F_{(3)}=0.91$ $P=0.441$; CO₂ treatment $F_{(2)}=106.56$, $P<0.001$; Interaction $F_{(6)}=1.66$, $P=0.151$). P values from the planned comparisons using Tukey HSD post-hoc tests confirmed that the difference between stomatal aperture at ambient and high CO₂ was not significant in *GSL8i-RNAi*+dex, whereas all three controls showed a significant stomatal closing effect ($P<0.05$). All lines including *GSL8-RNAi* showed a significant opening at low CO₂.

(B-E) The inability of the induced *GSL8-RNAi* stomata to close was due to a loss of ability to change both stomatal length and width. The length of the stomatal complex was constant in all lines under all treatments. (Note: these bioassays were performed by Sarah Carroll)

4.3 Discussion

In this chapter we began by describing the results of an immunological screen of paradermal leaf sections. We aimed to use this technique to identify cell wall components that may be involved in differential cell adhesion and separation at the stomatal tip walls and pore. We investigated how removal of cell wall components of interest from the guard cells affected stomatal function, and considered whether the molecules we identified were likely to be involved in adhesion, or whether they modulated guard cell function in a different way.

4.3.1 Demethylesterified pectin has multiple functions in the guard cells

Our previous work showed that demethylesterified HG generated by PME6 is required for stomatal flexibility and movement (Amsbury et al. 2016). However, in the *pme6* mutant some demethylesterified HG (detected by the LM19 mAb) remains in the tip walls and around the ends of the stomata, suggesting that at least one other *PME* gene must be expressed in stomata.

We might have expected PG enzyme treatment to remove both the PME6-generated demethylesterified HG and the demethylesterified pectin that remains at the outer ends of the tip walls in the *pme6* mutant. However, the HG that we observed around the pole of *pme6* stomata was also present in wildtype stomata treated with PG. LM19 signal was lost from all the same areas as in the *pme6* mutant, so our finding that PG-treated stomata still retained some opening response was unexpected, given that *pme6* stomata are unable to open or close in response to CO₂. One possible reason for this could be that the PG enzyme treatment was not specific to the stomata, whereas the *PME6* gene is highly stomata-specific, so the mutant was only affected in these cells. The AFM imaging showed that PG treatment drastically reduced stiffness throughout the epidermal tissue, so resistance of the epidermal cells against changing guard cell turgor pressure may have been reduced. Loss of guard cell stiffness following PG treatment could also be a factor in the reduced stomatal aperture at ambient CO₂.

Previous work in our lab sought to identify other *PME* genes with a role in stomatal function by examining knockout mutants in highly stomata-expressed *PME* genes (Amsbury et al. 2016; Schmid et al. 2005). Other than *pme6*, none of the lines examined showed differences from wildtype when immunolabelled, but as they were only examined in transverse orientation, differences at the tip walls could have been overlooked. However, it seems likely that even if the gene(s) responsible for the demethylesterification of polar pectin were knocked out, PME6 could also have activity in the same area, obscuring the phenotype of the other *pme* mutant(s). Therefore identification of the gene(s) responsible for demethylesterified HG at the stomatal poles might require *pme* gene knockouts in a *pme6* mutant background. The

downside to this approach would be the difficulty of examining functional differences given the inability of *pme6* stomata to open or close. An alternative approach could be to investigate the localisation of demethylesterified HG in greater depth, perhaps by immunogold labelling. This would allow differentiation between demethylesterified HG in the primary wall and the middle lamella, which might be products of different PME enzymes. It seems likely that PME6-generated demethylesterified HG would be localised to the primary wall, given its distribution throughout the guard cells and its role in flexibility, whereas a yet-unidentified PME might generate demethylesterified HG in the middle lamella at the tip walls, which could have a role in adhesion between the guard cell pair. In summary, identifying the *PME* gene(s) responsible for the polar deposit of demethylesterified HG, and testing the functional role of this pectin deposit, remains a significant challenge for future research.

4.3.2 Callose is localised to guard cell tip walls and is required for stomatal closure

In dividing cells, callose is laid down in the new cell plate, but it is rapidly replaced with cellulose and is not typically observed after cytokinesis (Thiele et al. 2009). We observed callose in the wall between the guard cells during the division of the guard mother cell. Callose persisted in the tip walls long after the formation of the stomatal pore, though it did not appear to be present in the oldest stomata. Callose in stomatal tip walls has previously been observed in passing, but the potential functional significance has not been investigated (Peterson et al. 1975; Guseman et al. 2010).

We initially tested the effect of callose removal on stomatal function by performing a bioassay on epidermal peels from leaves treated with β -(1,3)-D-glucanase. Callose was not observed in epidermal cells other than the stomata prior to pre-treatment, so we anticipated the results of this bioassay to be more specific to an effect on stomata than was the case for the bioassay on PG-treated samples. The results suggested that callose was not involved in stomatal opening, but was required for stomatal closure in response to high CO₂. This result was confirmed in a bioassay of the induced *GSL8-RNAi* mutant, which also had reduced stomatal callose. *GSL8* has been described as the main *GSL* gene expressed in plants, and a wide range of roles have been reported including cell plate generation for cytokinesis, and stomatal patterning via regulation of plasmodesmatal constriction (Thiele et al. 2009; Guseman et al. 2010). We are currently generating a construct to down-regulate the highly expressed sister gene *GSL10*, and it will be informative to see how any phenotypic effects on stomata in these lines compare to those we have already observed in induced *GSL8-RNAi* plants.

Callose in cell walls is constantly turned over by the antagonistic action of glucan-like synthase (*GSL*) genes and β -(1,3)-D-glucanases (Chen et al. 2009). Loss of callose in the induced *GSL8-RNAi* plants within 24 hours, and recovery within a further day, confirmed that the guard cell

tip wall callose that we observed was subject to rapid degradation and was predominantly synthesised by GSL8. This constant cycling of callose must bear some energetic cost, so is presumably functionally important, perhaps facilitating efficient re-localisation of this polymer. A potential role for dynamic callose localisation in the function of young stomata has previously been reported in the fern *Asplenidium nidus* (Apostolakos et al. 2010), but the same result was not observed in mature stomata or in other fern species. In this system callose was reported to localise in a radial pattern rather than to the tip walls, and was only apparent in closed stomata, suggesting rapid remodelling of the cell wall in this species. We did not observe any radially localised callose, but given the variable results of our aniline blue staining and mAb-localisation experiments, we cannot preclude the possibility that radial callose arrays are also associated with stomatal closure in *Arabidopsis*. The specificity of these arrays to closed stomata in *A. nidus* is intriguing given that in our callose-deficient stomata it was the stomatal closing response that was lost while the opening response was unaffected. However, if radial callose arrays were proven to be essential for stomatal closure, this would still leave the question of the function of the tip wall callose deposits. Further precise characterisation of callose accumulation patterns in open and closed angiosperm stomata is required to resolve this issue.

We discovered callose in the tip wall while searching for cell wall components potentially involved in separation and adhesion between guard cell pairs, and observed that it is lost from the wall around the pore soon after the guard cells separate in that region. Although, to our knowledge, a role for callose in cell-cell adhesion has not previously been suggested, and no obvious mechanism presents itself, we cannot rule out this possibility. Currently adhesion between the guard cells is the only obviously essential property of the tip walls. However, the localisation of callose within the cell wall makes it unlikely that it could be directly involved in adhesion. Typically the middle lamella region is considered the critical cell wall zone joining adjacent cells, but callose is usually found in the primary wall where it is generated by the membrane-bound callose synthases (Schneider et al. 2016). More detailed imaging of stomatal callose localisation, for example using super-resolution microscopy, might provide further clues to the role of tip wall callose. Another possible mechanism of adhering cells could be physical linkage by plasmodesmatal connections, but unless the density of plasmodesmata in stomatal tip walls is unusually high compared to other cell walls this would be unlikely to explain the presence of callose throughout the tip wall. We may be able to test whether callose is involved in the opening of the stomatal pore by manipulating callose synthesis during the stage of leaf development when stomata are still forming, but prolonged alteration of callose synthesis would be very likely to have side effects due to changes in plasmodesmatal transport processes, unless the manipulations were guard-cell-specific.

4.3.3 Modelling approaches to understanding stomatal movement

Envisaging the mechanical outcome of specific stomatal cell wall alterations, and explaining how they affect stomatal movement, can be challenging given the many factors involved and the three dimensional nature of the shape change. For example, by what mechanism could changes in callose localisation prevent stomata from closing, and yet have no effect on opening? Recent work has begun to develop computational models to help unpick such questions (Woolfenden et al. 2017; Shtein et al. 2017). Using the Woolfenden et al. (2017) stomatal model, we recently reported the importance of fixed stomatal complex length for stomatal movement, and showed that the thickening of the cell walls around the pore may have a much smaller bearing on stomatal movement than previously thought (Carter et al. 2017).

Such models provide a useful tool for hypothesis generation and, in return, experimental data feeds into the models to improve the accuracy of the predictions. While the data from our CO₂ response bioassays provide interesting details on the nature of the shape changes associated with stomatal movement, if we were able to measure these changes in three dimensions this could lead to a great improvement in the power and accuracy of the model. One previous study attempted to combine 3D measurements of broad bean (*Vicia faba*) stomata with a modelling approach, but contrary to all of our findings, reported significant changes in stomatal complex length (Meckel et al. 2007). Furthermore, the Woolfenden et al. (2017) model currently predicts the behaviour of an isolated stomate, but given the turgor-pressure-driven nature of stomatal movement, resistance from surrounding cells must also be an important factor. Our bioassays confirmed that stomatal complexes change in width but not in length, as the model predicts, but it is intriguing to consider how this difference is achieved. We suggested a role for the demethylesterified polar pectin in this complex length constraint (Carter et al. 2017), but have so far been unable to test this thoroughly as some demethylesterified HG remained at the poles even after PG treatment. Stiffened poles, as observed by AFM, cannot in themselves prevent the middle portion of the guard cells from lengthening, so it seems highly likely that an interaction with the surrounding cells is crucial.

4.3.4 Conclusions and future work

These experiments furthered our ongoing investigation of the likely multiple roles of pectin in the guard cells, and identified a novel role for callose as a regulator of stomatal function. It remains to be determined which *PME* gene(s) are responsible for the formation of the demethylesterified HG deposits around the stomatal poles, and why these regions are minimally affected by exogenous application of PG, in contrast to the rest of the stomatal cell walls. Finding a way to specifically reduce polar demethylesterified HG in stomata would allow

us to test whether it is functionally significant. The discovery of callose in the stomatal tip walls provides an exciting new line of enquiry for understanding the structure and function of guard cell walls. We have found that the *GSL8* gene is responsible for most if not all stomatal callose, and that enzymatic or genetic removal of callose from the guard cells prevents stomatal closure but has no effect on opening. We cannot preclude the possibility that callose other than that which we have observed in the tip wall could contribute to stomatal function. It will be intriguing to see whether the callose effect is mediated by a change in cell wall stiffness by examining induced *GSL8-RNAi* plants by AFM. These data will be used to continue to improve a computational model of stomatal movement.

Chapter 5 Coordinating stomatal and mesophyll development

5.1 Introduction

Coordination of stomatal position with the underlying mesophyll structure must be important for connectivity and gas exchange (Dow & Bergmann 2014). Both stomatal conductance and mesophyll conductance have the potential to limit photosynthesis, but stomatal conductance has the greater effect on regulating water loss. It is therefore desirable under most conditions for mesophyll conductance to match or exceed stomatal conductance (Warren 2008). Despite the clear importance of developmental coordination between these tissues, our mechanistic understanding of this process is extremely limited. In this chapter we investigate the relative importance of stomatal function and stomatal patterning in determining the cellular architecture of the leaf mesophyll.

5.1.1 Stomatal patterning

Many genes regulating the patterning of stomata on the leaf epidermis have been identified in *Arabidopsis* (**Figure 5.1**). The transcription factors *SPEECH*, *MUTE* and *FAMA* are involved in cell fate transitions in stomatal lineage cells, respectively determining entry to the stomatal lineage, asymmetric meristemoid division to produce the guard mother cell, and the final symmetrical division that produces the stomatal guard cell pair (Lau & Bergmann 2012). Proper spacing of stomata requires regulation of cell polarity to ensure that divisions separate rather than cluster new stomata (Lau & Bergmann 2012). A large number of peptide signals and receptors have been identified and implicated in stomatal pattern (Rowe & Bergmann 2010). Interestingly, some of these patterning components are expressed in the underlying mesophyll cells, providing a potential mechanism for coordination between these tissue layers.

In our study, we focussed on two signalling peptides that exert opposite effects on stomatal density. The *EPFL9* (*EPIDERMAL PATTERNING FACTOR-LIKE 9*) gene was simultaneously identified by two research groups and was named *STOMAGEN* (*STOM*) due to the stomata-promoting effect of the peptide that it encodes (Hunt et al. 2010; Sugano et al. 2010). *STOM* is expressed in the internal tissue of the leaf rather than the epidermis. Expression of the related genes *EPF1* and *EPF2* (*EPIDERMAL PATTERNING FACTOR 1 and 2*) exerts a negative effect on stomatal number. *EPF2*, produced in meristemoid cells, represses entry to the guard cell lineage while *EPF1* is mainly produced in the guard mother cell to repress adjacent cells from adopting the same developmental fate: loss of *EPF1* expression results in clustered stomata

(Hunt & Gray 2009; Hara et al. 2007). We were able to obtain lines with reduced and increased expression of both *STOM* and *EPF2* (the *epf2* knockout also lacked *epf1*).

5.1.2 Coordination of stomatal and mesophyll development

The relationships between different leaf tissue layers have received little attention and are poorly understood. This may be partly due to the difficulties of accurately visualising the 3D structure of the mesophyll prior the recent advent of new imaging technologies such as microCT (Pajor et al. 2013). This x-ray based technique measures the density of samples, and can distinguish cells from airspace on this basis, allowing many leaf architectural parameters to be quantified with relative ease and greater accuracy than traditional, histological techniques permit (Theroux-Rancourt et al. 2017). There is a small body of evidence confirming that leaf tissue layers are coordinated in their development, but whether this is a direct coordination, or whether both layers respond to the same inputs, remains uncertain. The expression of *STOM* in the mesophyll rather than in epidermal cells led Sugano et al. (2010) to speculate that this signal peptide could be involved in coordination between the leaf layers, and Kawase et al. (2015) were able to measure an increase in airspace in *STOM* overexpressing lines from confocal images. However, a more recent study found that plants lacking *STOM* were still able to maintain a relationship between the stomatal density and mesophyll structure that was comparable to wildtype plants and other lines with abnormal expression of *EPF* family genes (Dow et al. 2017). They did, however, find that loss of the TMM (TOO MANY MOUTHS) receptor broke the coordination between stomatal pattern and mesophyll cell density, suggesting that *TMM* expression is required for coordinated patterning. These insights provide intriguing clues, but still leave many questions unanswered and components yet to be identified in what seems likely to be a complex coordination system.

5.1.3 Aims

We hypothesised that mesophyll airspace could be coordinated with stomatal density either through direct cell-cell signalling from the stomata (absolute coordination), or via a direct or indirect gas-exchange-based signal through functional stomatal pores (physiological coordination), or a combination of the two. To test these ideas we examined stomatal density, mesophyll architecture and physiology in stomatal patterning mutants (*STOM-oex*, *STOM-RNAi*, *EPF2-oex*, *epf1/2*) as well as a wildtype control (*Col-2*) and the *focl1* mutant (*focl1-1* allele), which has occluded stomatal pores due to an excess of cuticular ledge material (Hunt et al. 2010; Hunt & Gray 2009; Hunt et al. 2017). While the *focl1* mutation does not affect stomatal density, we would anticipate that the stomatal coverings would impair gas exchange, thereby potentially providing a means to discriminate between the two proposed mechanisms (absolute or physiological) for coordination of stomatal and mesophyll development. We

tested these possibilities by subjecting mature leaves from plants of each genotype to both gas exchange/fluorescence analysis and microCT imaging. These paired structural and physiological measurements were taken during the fifth week post-germination, and no more than four days apart for each leaf. We investigated whether measured physiological parameters, or calculated stomatal density or index, better predicted the structural variation that we observed.

(Note: Data collection for these experiments was started by other members of the research group. These contributions are noted at the end of each section of the results.)

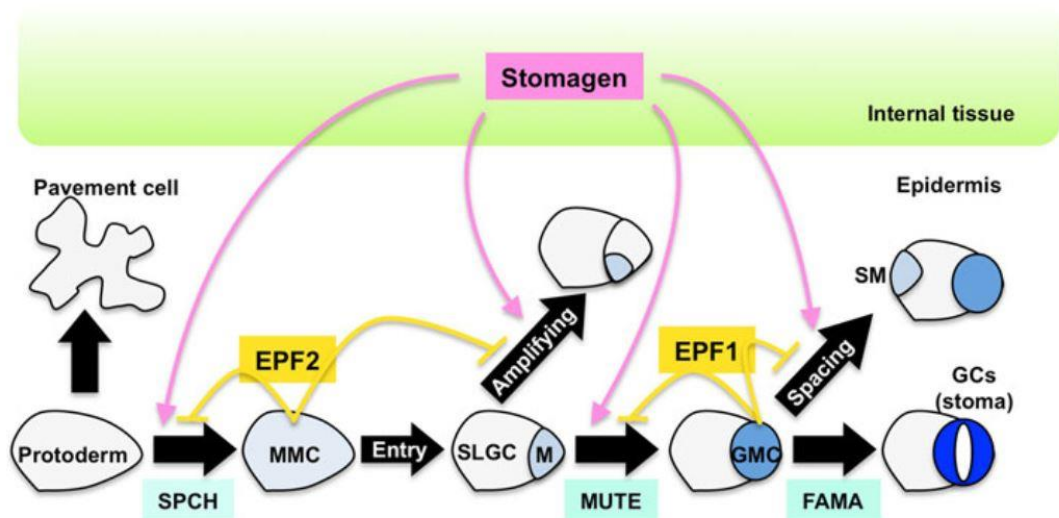


Figure 5.1: Stomatal patterning schematic

Cell fate transitions in the stomatal lineage are controlled by the transcription factors SPEECH, MUTE and FAMA. Signal peptides EPF1, EPF2 and Stomagen regulate stomatal development through cell-cell signalling.

MMC=meristemoid mother cell, SLGC=stomatal lineage ground cell, GMC=guard mother cell, SM=stomatal meristemoid

Figure from Shimada & Sugano (2011)

5.2 Results

5.2.1 Stomatal density and index

The stomatal density and index of all lines were measured to ensure that our growth conditions recapitulated the published phenotypes (**Figure 5.2**). This confirmed that *EPF2-oex* and *STOM-RNAi* had the lowest stomatal densities and indices, although these values were not statistically significantly different to the wildtype control. The *focl1* mutant was the same as Col-2 in terms of stomatal density and index, as previously reported. *STOM-oex* and *epf1/2* both showed elevation in stomatal density and index as expected, and these differences were significant compared to all four other lines. The *epf1/2* stomatal density was higher than that of *STOM-oex* whereas the stomatal index was lower, consistent with the reportedly excessive proliferation of epidermal cells in the absence of *EPF2*. These relationships held true for the abaxial and adaxial leaf surfaces, with slightly higher values on the abaxial side, as expected. The abaxial stomatal density was used for all analyses in the rest of this chapter.

Stomatal density and index measurements were collected from the same plants as the microCT and LICOR data for only two of the plant lines (Col-2 and *STOM-oex*). Data throughout this chapter were therefore treated as unpaired in the statistical analyses.

(Note: data for lines *STOM-oex*, *STOM-RNAi*, Col-2 and *focl1* were collected by Alice Mitchell)

5.2.2 Mesophyll porosity and channel distribution

Imaging revealed very little difference in overall leaf porosity between the lines, with only the highest and lowest porosity lines (*epf1/2* and *focl1*) showing any statistically significant difference from one another (**Figure 5.3-A,B**). Separating the two mesophyll layers revealed no significant differences in spongy mesophyll porosity between any of the lines, but palisade mesophyll showed more variation (**Figure 5.3-C,D**). Palisade porosity was significantly higher in the *epf1/2* line compared to *EPF2-oex*, *focl1* and *STOM-RNAi*, and *STOM-oex* was also more porous than *focl1* in this tissue. The porosity of the palisade layer was significantly, positively correlated with stomatal density (**Figure 5.3-E**; $R_2=0.75$, $P=0.027$).

We investigated whether changes in porosity were due to changes in the size (diameter) or density of the air channels, or both (**Figure 5.4**). Mean channel size was significantly lower in the *EPF2-oex* compared to the three lines with the largest channels (*focl1*, *STOM-oex*, *STOM-RNAi*), but otherwise there were no significant differences at the whole-leaf level (**Figure 5.4-A**). Examination of representative slices from the palisade and spongy mesophyll layers revealed no significant differences in spongy mesophyll channel size (**Figure 5.4-C**). In the palisade layer, *STOM-oex* had a significantly greater mean channel size than *EPF2-oex*, *STOM-RNAi* and Col-2 (**Figure 5.4-E**).

Channel density was unexpectedly high in the Col-2 control line, with significant differences from the two or three lowest-density lines in both palisade and whole-leaf analyses respectively (**Figure 5.4-B,D**). No significant differences were apparent between the spongy mesophyll channel densities, although the differences between the means followed the same pattern as in the palisade (**Figure 5.4-F**). *EPF2-oex* had significantly higher channel density than the lowest extreme (*STOM-oex*). We might expect this result, given the small mean channel size in this mutant, but more broadly, channel density and channel size were not strongly related. Only in the palisade mesophyll was a significant (negative) correlation detected between channel density and size, and even this relationship was weak ($R^2=0.68$, $p=0.043$; data not shown). Palisade channel size was also significantly but weakly correlated with stomatal index (**Figure 5.4-G**; $R^2=0.68$, $p=0.043$), but channel density was not, and neither channel size nor channel density correlated significantly with stomatal density or with palisade porosity.

Examining the surface area of mesophyll cells exposed to airspace through the depth of the leaf showed, somewhat unexpectedly, that the Col-2 control had the greatest area for CO₂ uptake, and *focl1* the least. This difference was significant, as were differences between Col-2 and *STOM-oex*, and between *focl1* and *epf1/2* (**Figure 5.5-A**). However, on separating out the spongy and palisade layers, a slightly different trend was apparent, and was consistent between the representative slices from both tissue layers. As the mesophyll cell surface area parameter is particularly sensitive to differences in certain image processing steps, this suggests that the data for whole leaves may be confounded by noise. In the analysis of separate tissue layers both halves of the *STOM-oex* leaf had a significantly greater exposed surface areas than both *EPF2-oex* and *STOM-RNAi* (**Figure 5.5-C,D**). The values for exposed cell surface area in each tissue appeared to follow the same pattern as stomatal index, and indeed a strong and significant correlation between these variables was observed in both tissues (**Figure 5.5-E,F**).

Comparisons of the two separated tissue layers were on a per-area rather than per volume basis as a single representative slice was measured (see Materials and Methods), but a comparison of leaf thickness showed no differences between the lines (**Figure 5.5-B**). This validates the comparison of area-based structural traits with leaf-level physiological measurements.

In summary, differences in porosity were mainly detected in the palisade layer, and variation in this parameter was positively correlated with stomatal density. Porosity changes could not be explained by the changes that we measured in the diameter and density of the channels, but palisade channel size was weakly related to both palisade channel density and stomatal index.

The surface area of mesophyll cells exposed to airspace in both the spongy and palisade mesophyll layers was strongly, positively correlated with stomatal index.

(Note: CT scans for lines *STOM-oex*, *STOM-RNAi*, Col-2 and *foc1* were masked and binarised by Dr Radek Pajor)

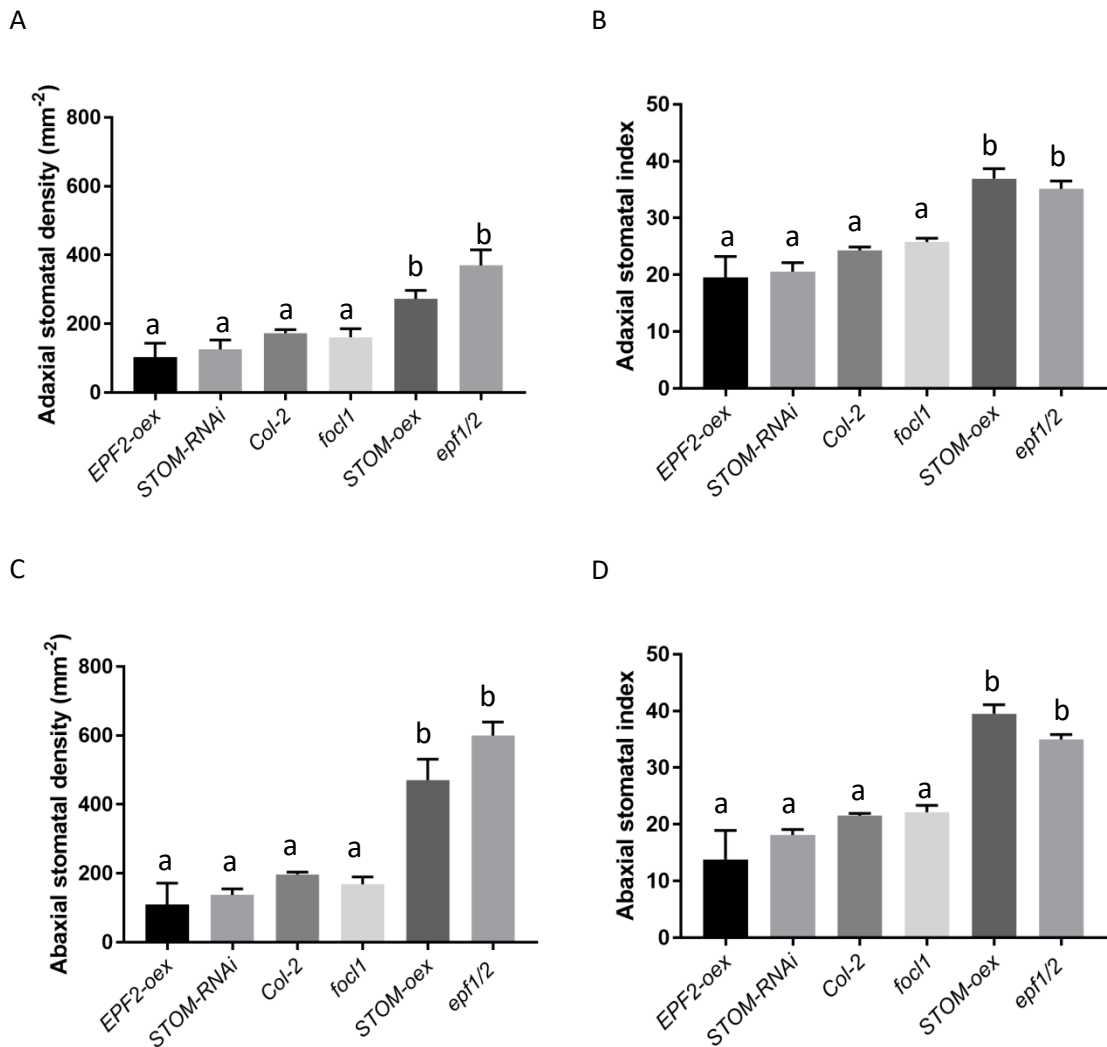
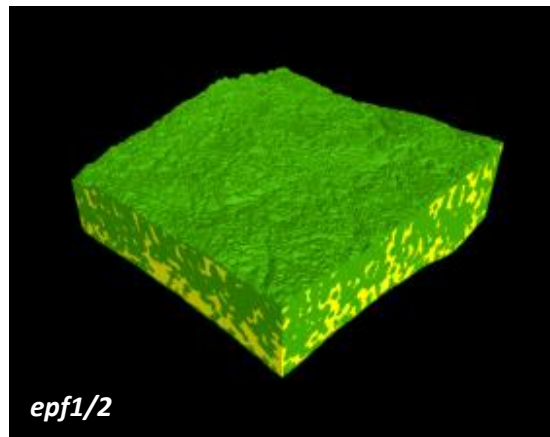
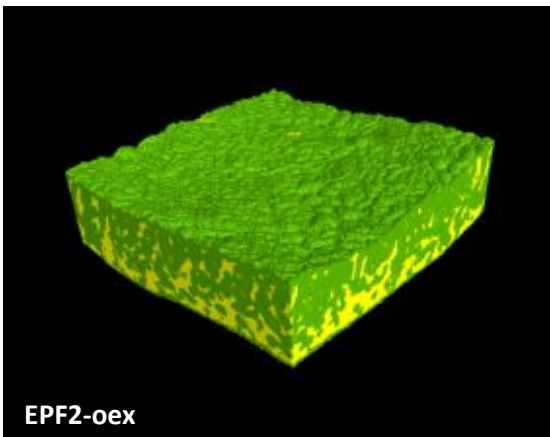
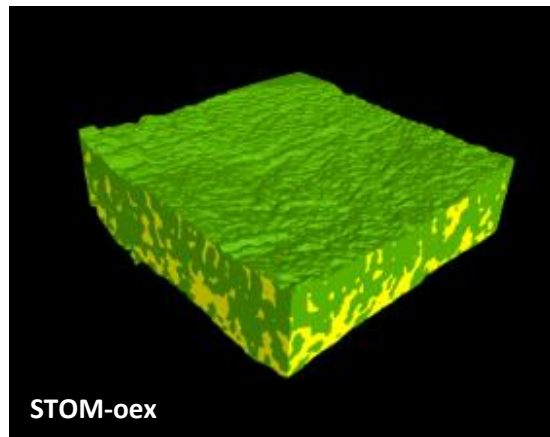
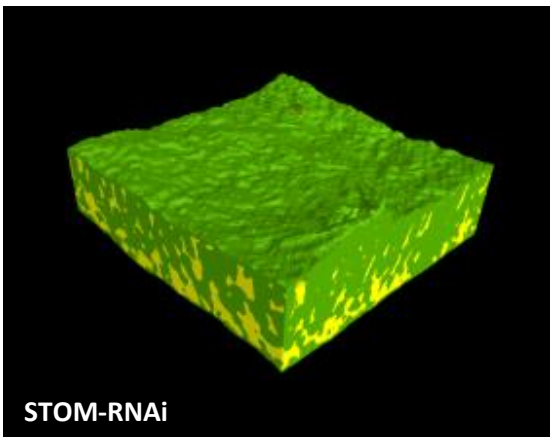
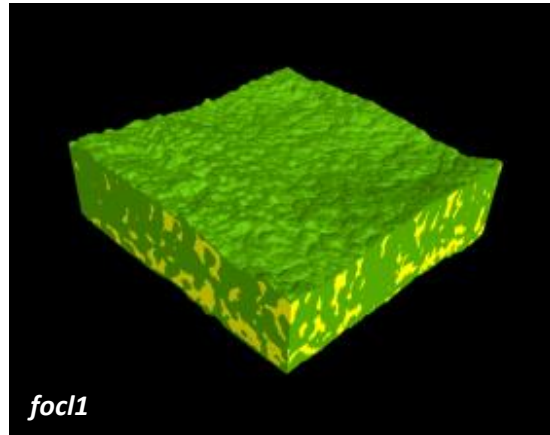
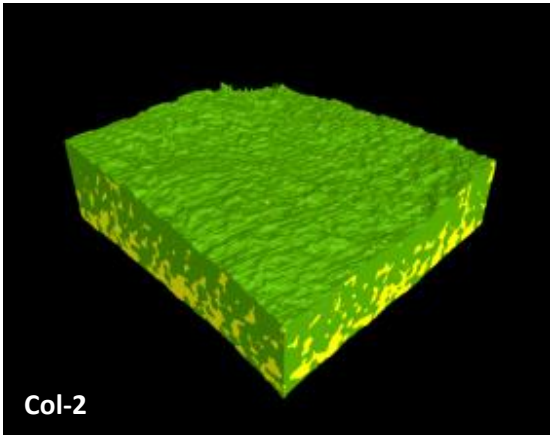


Figure 5.2: Stomatal density and index

(A-D) Adaxial stomatal density and index on both leaf surfaces was significantly higher in the STOM-oex and *epf1/2* lines than the other four lines (One-way ANOVA (A) $F_{(5,20)}=11.93$, $P<0.0001$; (B) $F_{(5,20)}=20.00$, $P<0.0001$; (C) $F_{(5,20)}=20.44$, $P<0.0001$; (D) $F_{(5,20)}=32.60$, $P<0.0001$). Leaf tissue cleared in ethanol was used for stomatal and epidermal cell counts, and samples were imaged for counting at three regions on each face of each leaf. All error bars represent the standard error of the mean. Letters indicate groups of lines that are not significantly different from one another according to post-hoc Tukey tests ($p<0.05$). N=3 for *EPF2-oex* and *epf1/2*. N=4 for *STOM-RNAi* and *foci1*. N=6 for *Col-2* and *STOM-oex*.

A



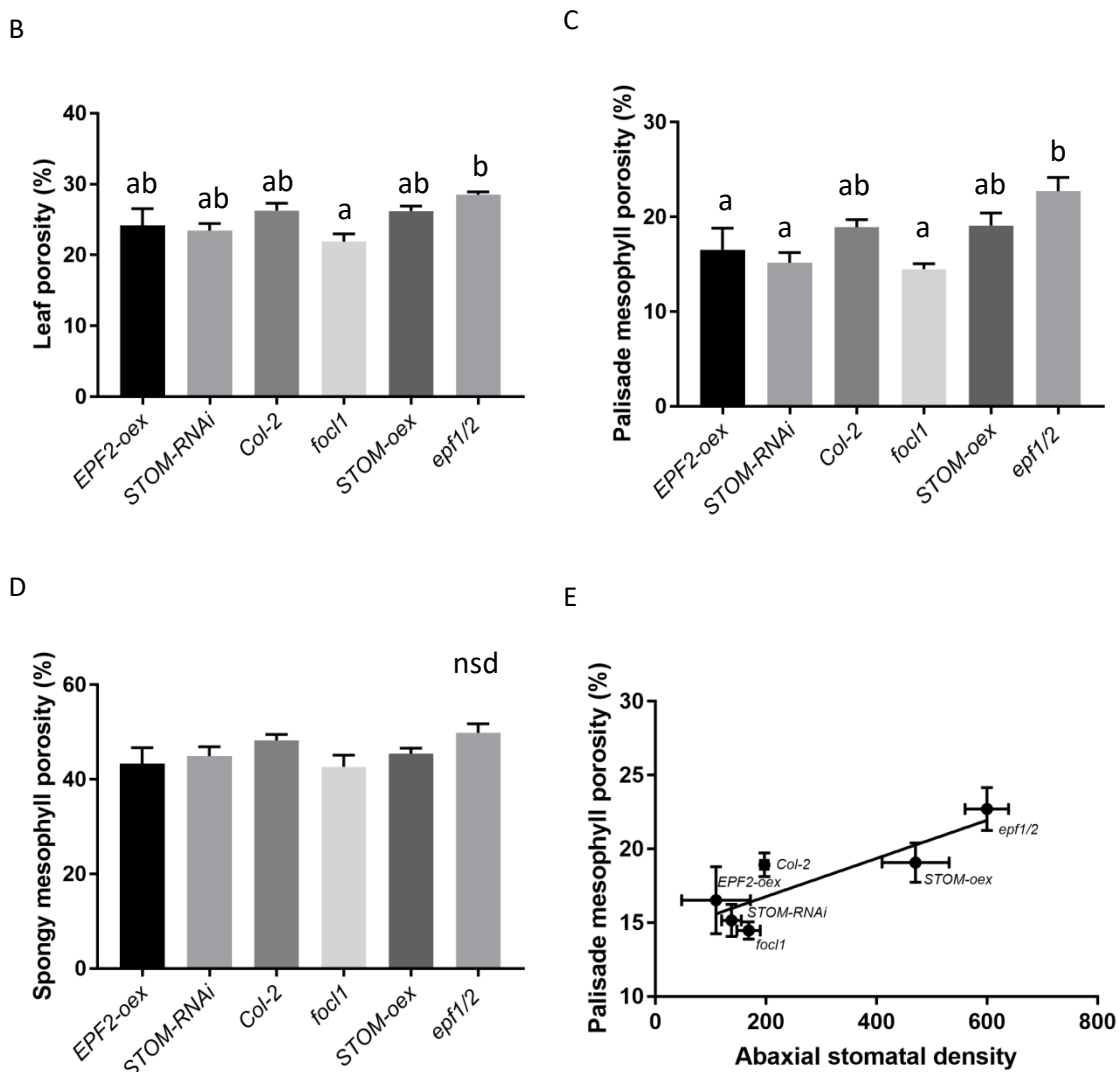


Figure 5.3: Porosity

(A) Representative 3D renderings of microCT data for each line. Green represents tissue, and air channels are indicated in yellow. It is difficult to predict the measured patterns of airspace by visual inspection. Each rendering represents the 1.1mm² areas of leaf tissue used for analysis (Note: these renderings were generated by Dr Andrew Mathers at the Hounsfield Facility, University of Nottingham)

(B) Leaf porosity (the proportion of the leaf volume occupied by airspace) was lowest in *foc1* and highest in *epf1/2* (One-way ANOVA, $F_{(5,30)}=3.51$, $P=0.013$).

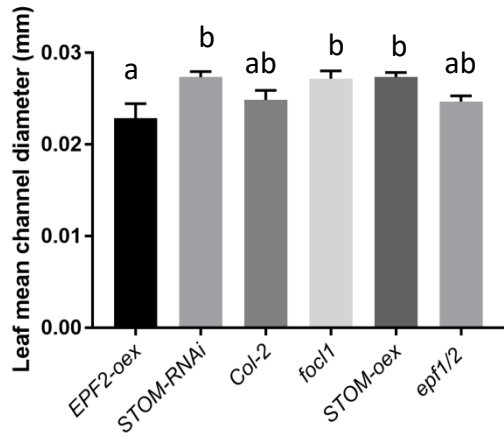
(C) Palisade mesophyll porosity was lowest in *EPF2-*oex**, *STOM-RNAi* and *foc1*, and highest in *epf1/2* (One-way ANOVA, $F_{(5,30)}=4.95$, $P=0.002$).

(D) Spongy mesophyll porosity did not differ between lines (One-way ANOVA, $F_{(5,30)}=1.68$, $P=0.169$).

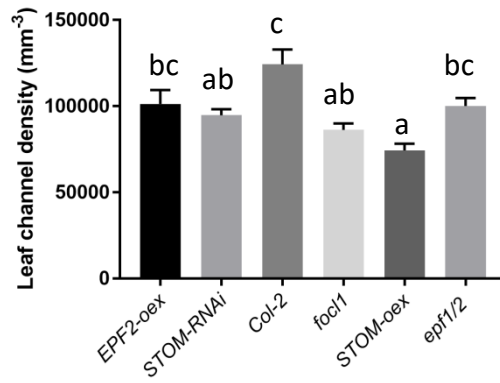
(E) There was a significant, positive correlation between abaxial stomatal density and palisade mesophyll porosity (Linear regression, $R^2=0.75$, $P=0.027$).

All error bars represent the standard error of the mean. N=6 for all lines, except for calculations of stomatal density in (E) (see **Figure 5.2**). Letters indicate groups of lines that are not significantly different from one another according to post-hoc Tukey tests ($p<0.05$). All parameters were calculated from the microCT image data, except stomatal density which was counted from different plants (data are not paired).

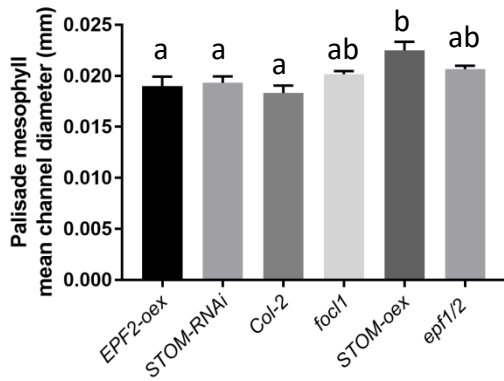
A



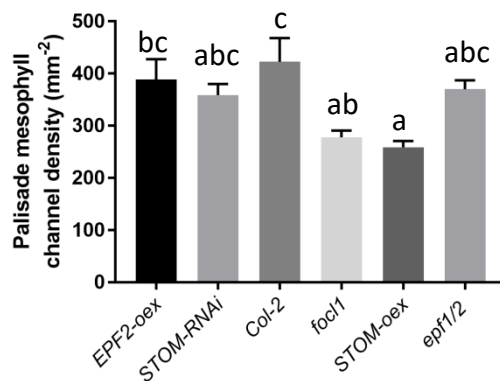
B



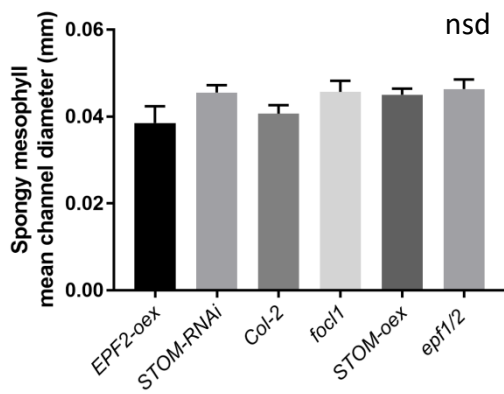
C



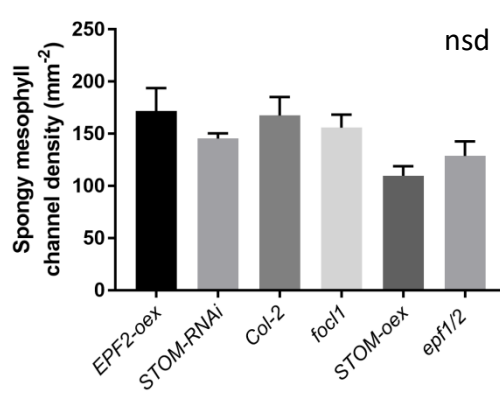
D



E



F



G

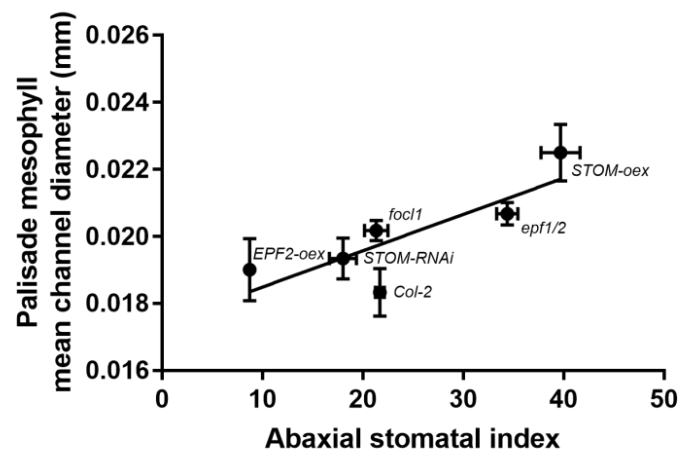


Figure 5.4: Mesophyll channel size and channel density

(A) Leaf mean channel diameter was lowest in *EPF2-oex* and highest in *STOM-RNAi*, *focl1* and *STOM-oex* (One-way ANOVA, $F_{(5,30)}=3.93$, $P=0.007$).

(B) Leaf mean channel density was lowest in *STOM-oex* and highest in *Col-2* (One-way ANOVA, $F_{(5,30)}=8.30$, $P<0.0001$).

(C) Palisade mean channel diameter was lowest in *EPF2-oex*, *STOM-RNAi* and *Col-2*, and highest in *STOM-oex* (One-way ANOVA, $F_{(5,30)}=4.91$, $P=0.002$).

(D) Palisade mean channel density was lowest in *STOM-oex* and highest in *Col-2* (One-way ANOVA, $F_{(5,30)}=5.37$, $P=0.001$).

(E) Spongy mean channel diameter did not differ significantly between lines (One-way ANOVA, $F_{(5,30)}=1.76$, $P=0.151$).

(F) Spongy mean channel density differed between lines according to the ANOVA test, but none of the individual comparisons were significant according to the post-hoc Tukey tests (One-way ANOVA, $F_{(5,30)}=2.73$, $P=0.038$).

(G) There was a significant, positive correlation between abaxial stomatal index and mean channel diameter in the palisade mesophyll (Linear regression, $R^2=0.68$, $p=0.043$).

All error bars represent the standard error of the mean. $N=6$ for all lines, except for calculations of stomatal index contributing to (G)(see **Figure 5.2**).

Letters indicate groups of lines that are not significantly different from one another according to post-hoc Tukey tests ($p<0.05$). All parameters were calculated from the microCT image data, except stomatal index which was counted from different plants (data are not paired).

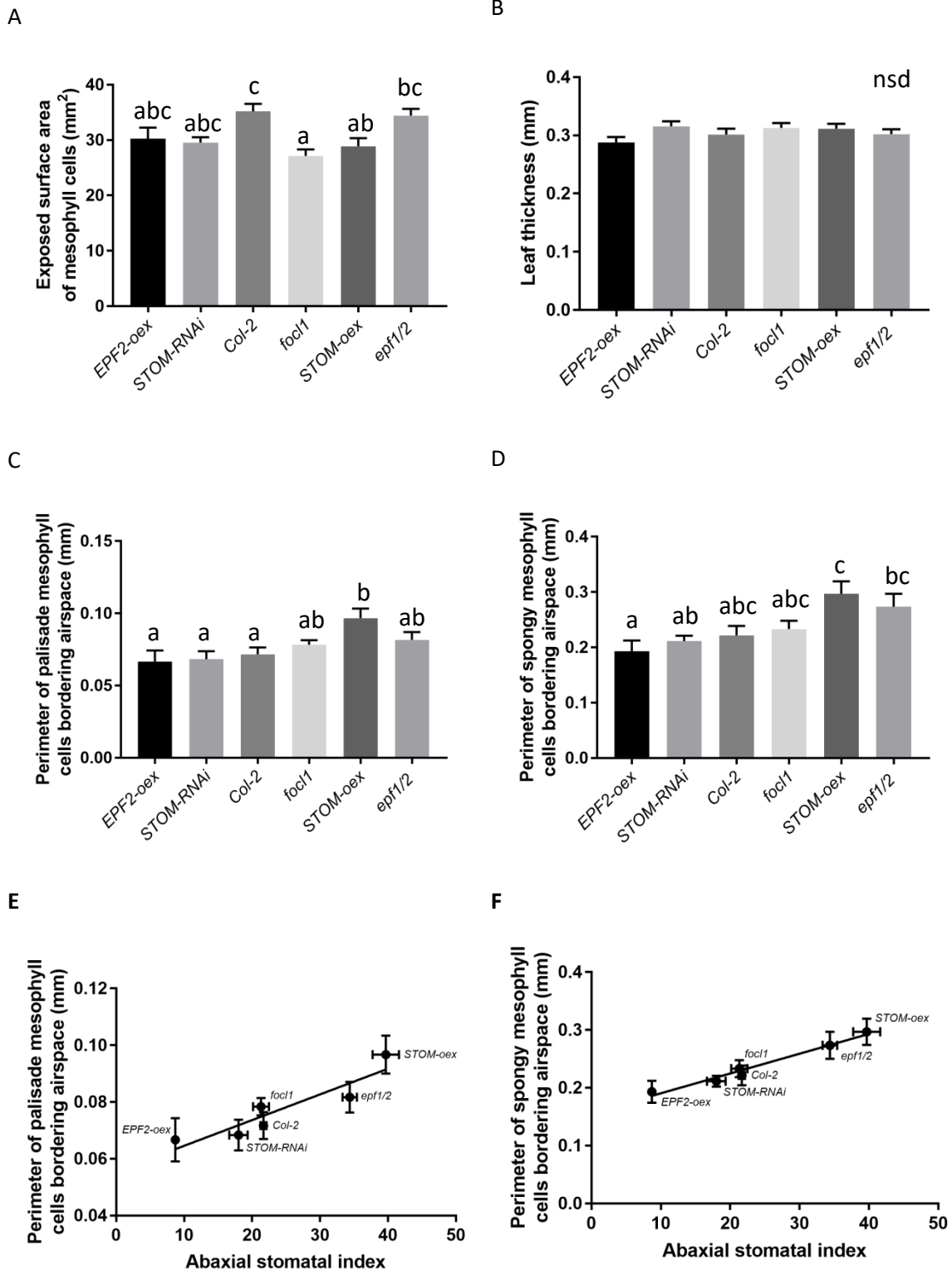


Figure 5.5: Exposed mesophyll surface area and leaf thickness

(A) The exposed surface area of mesophyll cells throughout the leaf depth differed significantly between lines, with *focl1* the lowest and Col-2 the highest (One-way ANOVA, $F_{(5,30)}=5.15$, $P=0.002$).

(B) Leaf thickness did not differ significantly between lines (One-way ANOVA, $F_{(5,30)}=1.37$, $P=0.264$).

(C) The perimeter of cells bordering airspaces in representative palisade mesophyll slices was lowest in *EPF2-oex*, *STOM-RNAi* and Col-2 and highest in *STOM-oex* (One-way ANOVA, $F_{(5,30)}=3.85$, $P=0.008$).

(D) The perimeter of cells bordering airspaces in representative spongy mesophyll slices was lowest in *EPF2-oex* and highest in *STOM-oex* (One-way ANOVA, $F_{(5,30)}=4.47$, $P=0.004$).

(E) There was a strong, significant, positive correlation between the abaxial stomatal index and the perimeter of cells bordering airspace in the representative palisade mesophyll slices (Linear regression, $R^2=0.84$, $P=0.010$).

(F) There was a strong, significant, positive correlation between the abaxial stomatal index and the perimeter of cells bordering airspace in the representative spongy mesophyll slices (Linear regression, $R^2=0.97$, $P=0.0003$).

All error bars represent the standard error of the mean. $N=6$ for all lines, except for calculations of stomatal index in (E) and (F)-(see **Figure 5.2**).

Letters indicate groups of lines that are not significantly different from one another according to post-hoc Tukey tests ($p<0.05$). All parameters were calculated from the microCT image data, except stomatal index which was counted from different plants (data are not paired).

5.2.3 Light and CO₂ response

We took simultaneous gas exchange and fluorescence measurements to compare the responses of these six lines to changes in light and internal CO₂ concentration (C_i). At first glance, the CO₂ and light response curves look very similar between lines (**Figure 5.6-A,B**), but a closer look at the CO₂ curves revealed some differences, such as variation in the measured assimilation rate under ambient CO₂ (A_{400}). Among the stomatal patterning lines, stomatal density was a strong predictor of A_{400} , but with the *focl1* line included in the comparison this relationship broke down (**Figure 5.6-C,D**). The differences in A_{400} between the *EPF2-oex* and *epf1/2* lines were less pronounced than those previously reported in the literature, although this may be partly explained by different growth conditions (Franks et al. 2015).

We used a modelling tool to fit curves to the data and generate values for key photosynthetic parameters (Bellasio et al. 2016). This confirmed that the light curves were extremely similar between all lines, with no significant differences in gross assimilation under saturating light (GA_{sat} , asymptote of modelled curve) or in the maximum quantum yield for CO₂ fixation, under light-limited conditions ($Y(CO_2)_{LL}$, initial slope of modelled curve)(data not shown). There were some differences in the light compensation point (LCP, modelled x-intercept) with *STOM-oex* requiring the most light to achieve net assimilation (significantly higher than *EPF2-oex* and *Col-2*)(**Figure 5.7-A**). This could be related to the high porosity in this mutant reducing the effectiveness of light attenuation in the leaf.

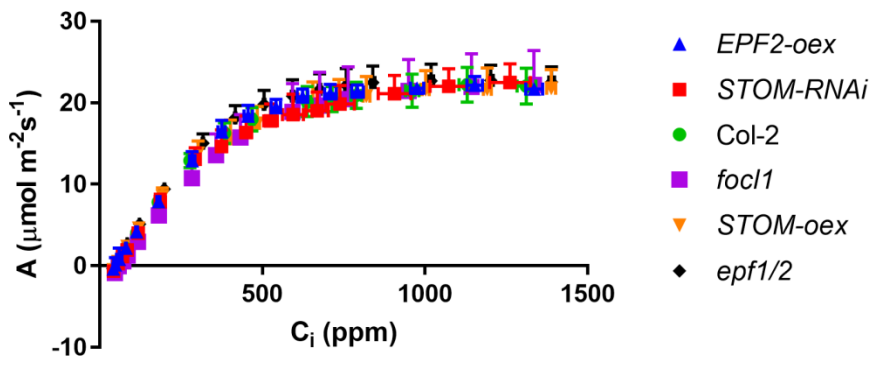
Similarly, for the fitted CO₂ response curves there were no significant differences in the maximum assimilation under saturating CO₂ (A_{sat} , asymptote of modelled curve) or in the maximum carboxylation efficiency of Rubisco (CE, initial slope of modelled curve)(data not shown). However, there were some differences in the carbon compensation point (CCP, modelled x-intercept), with the *focl1* mutant needing a significantly higher C_i to achieve net assimilation (**Figure 5.7-B**). This explains the lower measured assimilation value at ambient CO₂; despite the shape of the curve being comparable to other lines, the values are shifted. In fact CCP was a good predictor of A_{400} across the dataset (**Figure 5.7-C**; $R^2=0.84$, $P=0.010$).

The LICOR derives the stomatal conductance to CO₂ (g_s) at each logged point, as this factor contributes to controlling the assimilation rate. CO₂ response curves were conducted rapidly to minimise changes in stomatal aperture (and thus g_s) over the course of the measuring period, whereas light curves were conducted relatively slowly to allow for some stomatal adjustment. As g_s is measured on a per-area basis, we would expect lines with lower stomatal density to have the lowest g_s . We compared g_s at ambient CO₂ (from the CO₂ response curves) between lines and found that the *focl1* mutant had the lowest g_s , which can be explained by the occluded stomata in these plants (**Figure 5.8-A**). However, when we factored in the stomatal

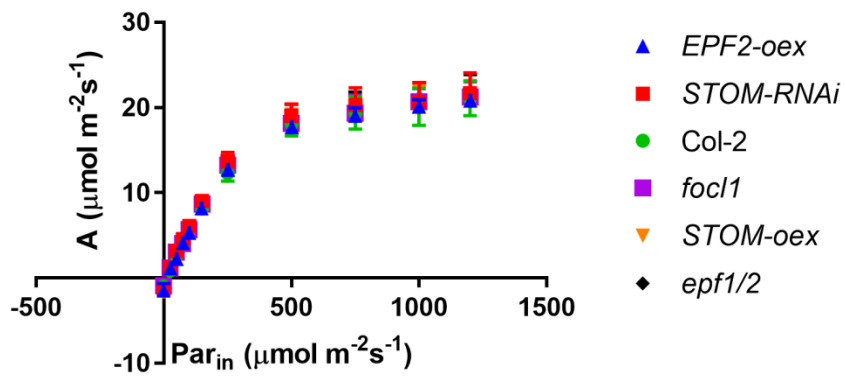
density of the mutants the *focl1* line was a good fit to the overall relationship between stomatal density and g_s (**Figure 5.8-B,C**; $R^2=0.79$, $P=0.018$ with *focl1*, $R^2=0.82$, $P=0.034$ with *focl1*). This suggests that the very low assimilation rate in the *focl1* mutant can only be partly explained by the lower g_s in this line. We also noticed that the range of g_s change in *focl1* plants, over the course of the CO_2 and light response curves, was much smaller than that of the other mutants, suggesting a reduced ability to adjust the stomatal aperture.

(Note: LICOR experiments for lines *STOM-oex*, *STOM-RNAi*, *Col-2* and *focl1* were carried out by Dr Marjorie Lundgren)

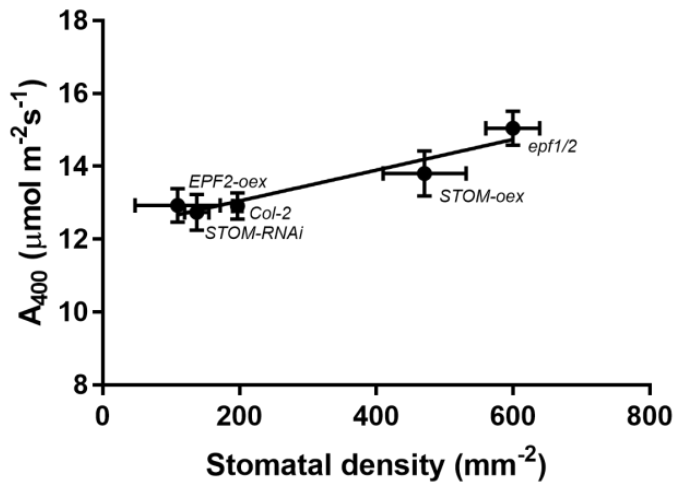
A



B



C



D

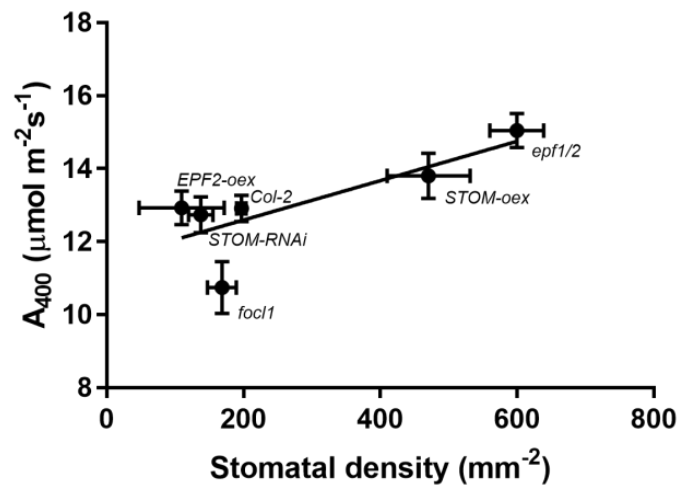


Figure 5.6: Response of photosynthetic rate to changes in CO₂ and light

(A) CO₂ response curves for all lines. N=6 for each line except *STOM-RNAi* where N=4.

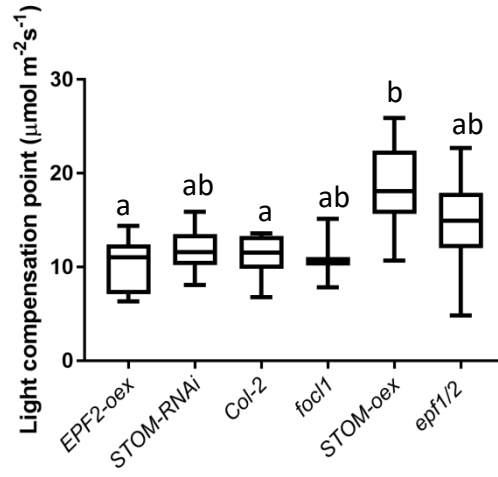
(B) Light curves for all lines. N=6 for each line except *STOM-RNAi* and *foc1* where N=3.

(C) There was a significant correlation between stomatal density and A₄₀₀ (assimilation under ambient CO₂ and saturating light) when only the stomatal patterning lines were included in the analysis (Linear regression, R²=0.91, P=0.012). N for A₄₀₀ as (A); see **Figure 5.2** for N for stomatal density.

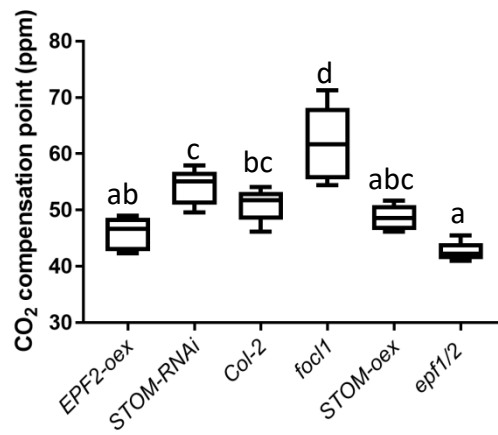
(D) When *foc1* was included in the regression analysis, no significant correlation was calculated (Linear regression, R²=0.60, P=0.07). N as for (C).

All error bars represent the standard error of the mean. Data generated using a LICOR 6800.

A



B



C

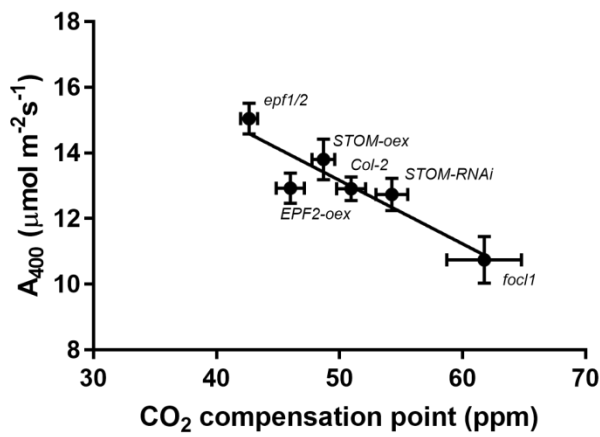


Figure 5.7: Modelled light and CO₂ compensation points

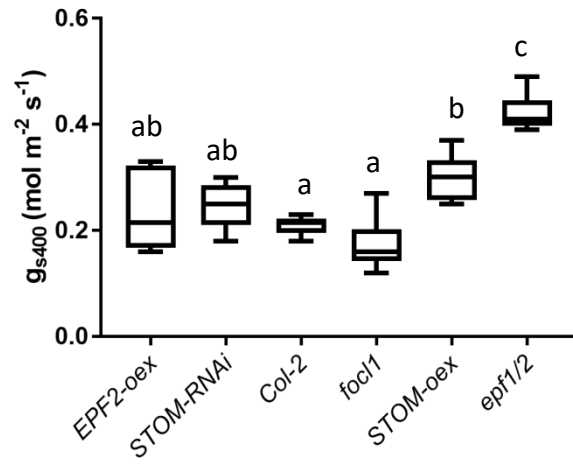
(A) The light compensation point differed significantly between lines, with *EPF2-ox* and Col-2 the lowest, and *STOM-ox* the highest (One-way ANOVA, $F_{(5,27)}=3.60$, $P=0.013$). $N=6$ for each line except *STOM-RNAi* and *foc1* where $N=3$.

(B) The CO_2 compensation point differed significantly between lines, with *epf1/2* the lowest and *foc1* the highest (One-way ANOVA, $F_{(5,29)}=20.1$, $P<0.0001$). $N=6$ for each line except *STOM-RNAi* where $N=4$.

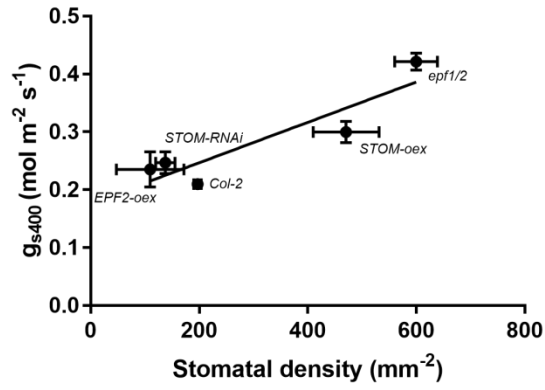
(C) There was a significant, negative correlation between the CO_2 compensation point and A_{400} (assimilation under ambient CO_2 and saturating light)(Linear regression, $R^2=0.84$, $P=0.010$).

All error bars represent the standard error of the mean. Letters indicate groups of lines that are not significantly different from one another according to post-hoc Tukey tests ($p<0.05$). Values in (A) and (B) derived from the LICOR data in **Figure 5.6** using the Excel tool described in (Bellasio et al. 2016).

A



B



C

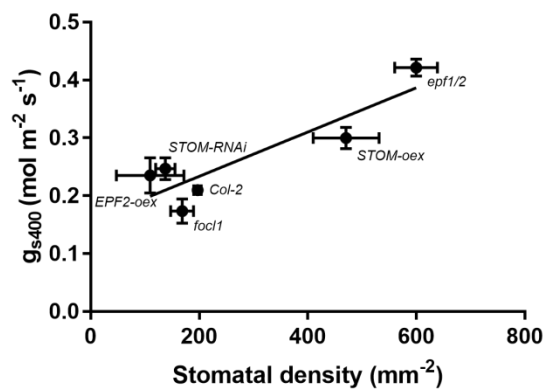


Figure 5.8: Relationship between g_{s400} and stomatal density

(A) g_{s400} , the stomatal conductance under ambient CO₂ and saturating light varies between lines (One-way ANOVA, $F_{(5,30)}=19.6$, $P<0.0001$). $N=6$ for each line except *STOM-RNAi* where $N=4$.

(B) There was a significant correlation between stomatal density and g_{s400} when only the stomatal patterning lines were included in the analysis SD vs g_s without *focl1* (Linear regression, $R^2=0.82$, $P=0.034$).

(C) Adding the *focl1* mutant to this analysis made little difference to the fit of the regression model (Linear regression, $R^2=0.79$, $P=0.018$).

All error bars represent the standard error of the mean.

Letters indicate groups of lines that are not significantly different from one another according to post-hoc Tukey tests ($p<0.05$).

5.2.4 Relating physiology to structure

As we demonstrated (**Figure 5.3-E**), stomatal density is significantly positively correlated with the porosity of the palisade mesophyll. This relationship could be driven by cell-cell communication during development, or could incorporate some environmental responsiveness, such as modulation of cell expansion or separation in response to CO₂ availability. We tried to test these possibilities by comparing the proportion of variation in palisade porosity that could be explained by stomatal density to the proportion explained by g_{s400} (**Figure 5.9**). We hypothesised that the palisade porosity would be more strongly related to g_s than to stomatal density, and that this would be primarily due to the porosity of the *focl1* mutant being better predicted by g_s . However, we found that both of these variables were able to explain the same amount of the variation in palisade porosity (g_s : $R^2=0.73$, $P=0.03$; **SD**: $R^2=0.75$, $P=0.03$), and that the *focl1* mutant was similarly well predicted by both analyses.

The most striking relationships to emerge from the structural microCT data were between the stomatal index and the exposed cell surface area for gas exchange in both the palisade and spongy layers (**Figure 5.5-E,F**). Although increased exposed surface area is thought to increase photosynthetic gas exchange, we found no significant relationship with assimilation or g_s in the palisade or spongy layer.

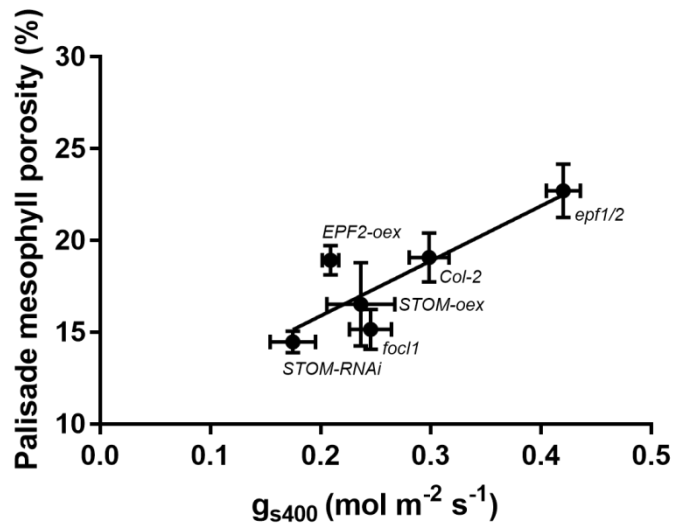


Figure 5.9: Relationship between g_{s400} and palisade porosity

There was a significant, positive correlation between g_{s400} (the stomatal conductance under ambient CO₂ and saturating light), and the porosity of the palisade mesophyll (Linear regression, $R^2=0.73$, $P=0.031$). However, the correlation between stomatal density and palisade porosity was equally strong (**Figure 5.3-E**). Error bars represent the standard error of the mean.

5.3 Discussion

A relationship between stomatal density and mesophyll cellular architecture has previously been demonstrated (Dow et al. 2017), but the mechanism of coordination between these tissues has not been elucidated. Using mutants with aberrant stomatal pattern we sought to investigate this relationship further. Additionally, a mutant with occluded stomata allowed us to test the idea that a gas-exchange-based signal via the stomata could play a role in determining mesophyll cellular architecture, instead of, or as well as, direct signals between the epidermis and underlying tissue.

5.3.1 Effect of stomatal density on mesophyll patterning

Our results showed a positive correlation between stomatal density and palisade mesophyll porosity. However, neither the mean diameter of channels nor the density of channels between cells directly explained the difference in porosity that we observed. Dow et al. (2017) examined a collection of stomatal patterning mutants including some of the same lines used in our study, but quantified structure in terms of the density of cells rather than the density of airspace, reporting a positive correlation between stomatal density and palisade mesophyll cell density. It remains unclear how these structural features in adjacent leaf layers might be coordinated (See 5.3.3).

One unexpected finding was the strong correlation between the stomatal index and the surface area of cells exposed to airspace in both the palisade and spongy mesophyll. Exposed surface area of mesophyll cells for CO₂ uptake is widely held to be a very important determinant of gas exchange properties in the leaf, but we found no correlation between exposed surface area and assimilation rate or stomatal conductance under ambient CO₂ conditions (Evans et al. 2009; Tholen et al. 2012; Tomás et al. 2013). The fact that stomatal index rather than stomatal density was the strongest predictor of exposed surface area perhaps suggests that this parameter is set primarily by genetic factors such as those that also control the division of cells in the epidermis, rather than by altered physiology.

With the exception exposed surface area, we were unable to detect significant differences between lines in the spongy mesophyll structure. This may partly due to technical constraints of the microCT image processing procedure combined with the complex and variable nature of the spongy mesophyll tissue, which is composed of large airspaces and highly irregularly shaped cells. Alternatively, changes in the palisade mesophyll may have stronger effects on physiology as this tissue is both the primary site of photosynthesis, and the more cell-dense, perhaps suggesting greater resistance to bulk flow of gasses. The large stomatal cavities adjacent to the lower epidermis are particularly interesting, but it might be challenging to test how they are reliably positioned beneath stomata as any mutants lacking such a large

proportion of their usual airspace may struggle to survive. Even an inducible approach to manipulating expression of candidate genes would be unlikely to resolve this difficulty, as these structural patterns are determined very early in development (Serna et al. 2002).

5.3.2 Effect of stomatal function on mesophyll patterning and physiology

The stomata of the *focl1* mutant are covered by cuticular material, although the degree of occlusion is variable. The plants exhibit a dwarfed growth phenotype, but are still viable as stomatal function is severely compromised rather than entirely lost (Hunt et al. 2017). *focl1* has the same stomatal density and stomatal index as wildtype plants, but due to the stomatal coverings it has lower g_s .

We hypothesised that mesophyll structure might be at least partly determined by g_s , the conductance of stomata to CO_2 . Plants grown under elevated CO_2 have lower stomatal density and index, and fewer chloroplasts per mesophyll cell, amongst other changes (Teng et al. 2006). This suggests that leaves can perceive CO_2 -based signals and adjust their development accordingly. The concentration of CO_2 inside the leaf is partly determined by g_s . If g_s were an important driver of mesophyll porosity, we would expect that the porosity of the *focl1* mutant would be more closely correlated with g_s than stomatal density, but our data showed a negligible difference between these predictors. The *focl1* mutant did have the lowest palisade mesophyll porosity, and we cannot rule out a role for g_s in determining this structure, but our analyses did not provide evidence to support this idea more strongly than the alternative hypothesis.

The assimilation rate of the *focl1* mutant under ambient CO_2 was considerably lower than all of the other lines, and very much an outlier from the group in terms of the relationship between assimilation rate and stomatal density. It seems likely that a number of factors may combine to cause reduction in assimilation rate, as *focl1* was more consistent with the other lines with respect to most of the traits we investigated. The reduction in assimilation at ambient CO_2 was related to the lower CO_2 compensation point of *focl1* rather than other differences in the CO_2 response, which suggests that this mutant has a reduced $CO_2:O_2$ ratio at the site of Rubisco activity. The slightly lower g_s could be a factor in this, perhaps combined with a lower g_m that might be caused by the reduced porosity.

5.3.3 Determination of mesophyll structure

While our *focl1* mutant data did not provide compelling evidence for gas-exchange-determined mesophyll architecture, the question of the relative importance of genetics and physiology in determining leaf cellular patterning remains wide open. Evidence to date

suggests that both the genotype of the leaf and the atmosphere in which it develops will influence the final morphology.

A large number of leaf traits have been reported to vary with environmental growth conditions. For example leaves grown under higher light tend to be thicker, and leaves grown under higher CO₂ tend to have greater stomatal density (Teng et al. 2006; Casson & Hetherington 2010). Specific understanding of the way that growth conditions influence the mesophyll structure is lacking, but changes in leaf thickness, for example, must be accompanied by an increase in mesophyll cell size and/or number. Furthermore, systemic signals from older leaves can determine the stomatal development of subsequently emerging leaves even if the new leaves are experiencing different environmental conditions (Casson & Hetherington 2010). This provides evidence that the developmental programme of the plant can be actively coordinated on wide spatial and temporal scales, rather than coordinated only through common responses to environmental stimuli across tissues and organs.

The *STOM* and *EPF2* genes that we studied both encode signalling peptides, but many more genes are known to affect stomatal patterning, either via other signalling pathways or through transcriptional regulation. Dow *et al.* (2017) examined a wide range of stomatal patterning mutants and found that different classes of patterning genes exerted effects on the mesophyll in different ways. Their examination of *epf* mutants agreed with our finding that the patterning of cells and airspaces in the palisade mesophyll was affected, but in contrast, reduction in stomata through loss of the *SPCH* (*SPEECH*) transcription factor was associated with a thickening of the leaf rather than a change in cell density. Furthermore they found that *tmm* (*TOO MANY MOUTHS*) mutants did not show the same relationship between stomatal density and palisade cell density as the other mutants, which suggests that the TMM receptor is necessary for normal coordination between the stomata and mesophyll. Sugano *et al.* (2010) suggested that the mesophyll-specific expression of *STOM* might point to a role in regulating the coordination between the epidermis and mesophyll, but our data and those of Dow *et al.* (2017) do not support this idea as the *STOM* mutant was able to maintain coordination between the tissue layers. Finally, Dow *et al.* (2017) suggest that this coordination between layers allows CO₂ supply and demand to be matched. This does imply that physiology is a driver for coordination, but also that it generates coordination mechanisms on an evolutionary timescale rather than directly influencing patterning of both tissues simultaneously during the development of individual leaves.

5.3.4 Conclusions and future work

In this chapter we investigated the relationship between stomatal patterning, leaf internal cellular architecture, and leaf-level photosynthesis. We found that stomatal density correlates

with the porosity of the palisade mesophyll layer, and that stomatal index correlates with the exposed surface area of mesophyll cells. The mechanism of this coordination between the development of different leaf layers remains an intriguing challenge for future research, but evidence to date suggests that it is likely to involve a combination of genetic determination and physiological inputs.

Chapter 6 General Discussion

6.1 Airspace in the leaf: from form to function

Photosynthesis depends on the conductance of CO₂ from the air through the stomata and intercellular spaces of the leaf to the site of fixation in the chloroplasts. We set out to better understand the fundamental relationship between the architecture of this CO₂ pathway and the potential for gas exchange and photosynthetic assimilation at the leaf level. As discussed in Chapter 1, the cellular organisation of leaves is regulated at many levels. In this study we focussed on manipulating leaf tissue structures through changes in the cell walls, and by exploiting the coordination of mesophyll airspace with stomatal density.

Formation of mesophyll airspaces, and of the stomatal openings that connect them to the air outside the leaf, must both involve the cell wall. In Chapter 2 and Chapter 4 we used an antibody labelling approach to identify cell wall components in the mesophyll and stomata of *Arabidopsis* leaves. These data provided novel insights into the spatial distribution of various cell wall epitopes. We focussed our subsequent investigations on components that were localised specifically to adhered or to separated cell walls, as we hypothesised that schizogenous cell separation at the middle lamella would be involved in the differentiation of both stomata and mesophyll. Genetic manipulation of the levels of the cell wall epitopes that we identified led to changes in mesophyll architecture and stomatal function (below). However, we do not have evidence to specifically demonstrate that these structural changes were due to a difference in cell wall adhesion, and it is possible that they were instead mediated by mechanical changes in the cell wall properties that affected cell growth.

In the stomata, we observed that callose was present in the tip walls (Chapter 4). New cell walls typically contain callose but this is rapidly replaced by cellulose after cytokinesis (Thiele et al. 2009). We found that callose in stomatal tip walls persisted long after cytokinesis, although it was lost from the walls surrounding the stomatal pore once they had separated. We investigated the functional significance of stomatal callose by enzymatic callose removal and by transiently reducing the expression of the *GSL8* callose synthase gene via induction of RNAi (Han et al. 2014). In both cases the reduction in stomatal callose resulted in stomata being unable to close in response to a high CO₂ treatment, although the stomatal opening response was unaffected. Intriguingly, radial callose arrays have previously been reported in the fern *Asplenium nidus* in closed stomata only (Apostolakos et al. 2010). It is possible that such arrays are also present, and functionally significant, in closed *Arabidopsis* stomata, but this would not explain the presence of callose in the tip wall. The callose-dependence of the stomatal closure mechanism requires further investigation (See 6.2).

Our previous work on stomatal cell walls revealed a role for pectin demethylesterification in stomatal movement (Amsbury et al. 2016). The *pme6* mutant, which lacks a pectin methyl esterase (PME) enzyme that is usually highly expressed in stomata, is unable to demethylesterify stomatal HG and is also unable to modulate its stomatal aperture in response to high or sub-ambient CO₂ levels. However, we did observe small patches of demethylesterified HG at the very ends of the stomatal complex in the *pme6* mutant, and these were also observed in wild-type stomata that we treated with polygalacturonase, a pectin-degrading enzyme. This suggests that at least one other PME enzyme acts in the cell walls of stomata to generate these polar deposits of demethylesterified pectin, and that the deposits are resistant to enzymatic degradation, which could be due either to the precise epitope present, or to its relationship to other polymers within the cell wall matrix. A model of stomatal mechanics generated by our collaborators provided evidence that fixing of the stomata poles is important for stomatal movement (Carter et al. 2017). Indeed we observed that changes in the aperture (pore area) of stomata that had been induced to open or close were always explained by changes in the pore length, pore width and complex width, but never in the complex length, supporting the idea that this dimension is somehow fixed. These same points at the poles of stomata complexes were found to be the areas of greatest stiffness in epidermal tissue when leaf explants were probed by Atomic Force Microscopy (AFM). It seems plausible that specific pectin epitopes could contribute to polar stiffening of stomata, but further work is required to provide a mechanistic explanation for how this could prevent the stomatal complex length from changing.

In the mesophyll, immunolabelling revealed that forms of pectic HG with differing degrees of methylesterification were most abundant in different cell wall regions. The LM19 monoclonal antibody (mAb), which recognises a demethylesterified HG epitope, gave a stronger signal in adhered cell walls, whereas LM20, which binds a more highly methylesterified epitope, appeared to localise to the corners of airspaces. These results, combined with a widely proposed role for HG in cell adhesion in the literature, led us to seek mutants with altered quantity or quality of pectic HG (Daher & Braybrook 2015; Jarvis et al. 2003)(Chapter 3). We anticipated that such mutants would also vary in their cellular architecture due to changes in cell adhesion and/or growth.

We examined the distribution of LM19 and LM20 signal in the leaves of a number of *pme* knockout mutants selected on the basis of their expression patterns, and found that the most highly leaf-expressed *PME* gene (*PME3*) was required for generation of the LM19 epitope, although some HG conversion was probably still taking place as the LM20 signal pattern was unchanged. This result added a spatial dimension to our existing knowledge that *pme3* plants

have reduced levels of demethylesterified pectin (Raiola et al. 2011). Unfortunately the *pme3* mutant could not be subjected to detailed structural and physiological characterisation within the timeframe of this project, but this is a clear priority for future work.

We also obtained two pectin biosynthesis mutants, *qua1* and *qua2*, which had previously been reported to be deficient in cell adhesion (Mouille et al. 2003; Bouton et al. 2002). We confirmed the increased porosity of these lines by microCT analysis, and also measured their responses to changing light and CO₂. While the consistently low rates of photosynthesis that we measured in the *qua1* mutant were unsurprising given its dwarf stature and pale leaves, we did not anticipate the enhanced physiological performance that we measured in the *qua2* mutant, and were unable to explain these observations based on the data available. As *qua2* has a reduced level of demethylesterified pectin, but the degree of esterification of HG is unchanged, comparison of this mutant to the *pme3* line could provide interesting insights into the relative importance of pectin quality and quantity in determining mesophyll cellular architecture.

Our collection of pectin-related mutants also included the *arp3* (*actin-related protein 3*) plant line, which is deficient in actin nucleation and which may have reduced levels of cell wall HG (Li et al. 2003). While this mutant did not show any differences from Col-0 in the structure of the mesophyll, we did notice some unusual stomatal behaviour including a smaller stomatal aperture under ambient conditions, an increased aperture under low CO₂ accompanied by a distinctive, bowed-out shape. Changes in stomatal behaviour of *arp3* and other mutants in the same complex have previously been reported and attributed to changes in vacuolar fusion events in the guard cells but we propose that changes in cell wall properties may also play a role in determining the behaviour of the *arp3* stomata (Li et al. 2003; Jiang et al. 2012).

In addition to investigating the structure and function of these cell wall mutants, we conducted a paired microCT/gas exchange experiment on lines that varied in their stomatal density or stomatal function (Chapter 5). These lines provided a greater range of variation in porosity than the cell wall mutants, which was useful for testing ideas about leaf structure-function relationships. Among the stomatal patterning lines, we confirmed previous reports that stomatal density is correlated with mesophyll porosity in the palisade layer (Dow et al. 2017). We also observed an unexpected correlation between stomatal index and the exposed surface area of mesophyll cells, which held true in both the palisade and spongy layers. We propose that this relationship may be genetically determined, and could be linked to cell division control, but this idea requires further testing. The *focl1* mutant, which has normal stomatal density but reduced stomatal function due to cuticle-based stomatal coverings, was also included in our comparison. We hypothesised that gas exchange, most likely CO₂ flux, might

have a quantitative effect on the palisade mesophyll porosity, and we anticipated that this would lead to palisade porosity being better predicted by stomatal conductance (g_s) than by stomatal density. However, we found that both predictors were similarly effective, so we were unable to provide evidence either in support of this hypothesis or against it. The *focl1* mutant had a much lower assimilation rate than the other lines, which could only be partially explained by the lower g_s in this mutant, and could be the result of many combined small changes including the structural differences that we observed in the mesophyll. Other recent research suggested that the *tmm* receptor is essential for coordination of stomatal density and mesophyll tissue structure, but the signal was not identified (Dow et al. 2017). Much remains to be learned about how these tissues develop together, including, for example, how stomata are aligned with large cavities in the abaxial portion of the leaf.

6.2 Future work

The results of this project lead on to further critical questions. In this final section, experiments are proposed to directly follow up on the work in this thesis. In addition, the potential to apply the conclusions of this work to systems beyond the Arabidopsis leaf is evaluated.

Our investigation of the stomata cell wall is currently focussed on the functional role of callose in the tip walls and of demethylesterified HG at the poles of the complex. It is difficult to envisage how callose localised to the tip walls could be involved in stomatal closure, particularly given that dependence on callose for stomatal opening was not observed. One possible explanation, mentioned above, is that we have thus far failed to observe other potential callose deposits, such as those reported in the closed stomata of *A. nidus* (Apostolakos et al. 2010). Examining callose localisation in closed Arabidopsis stomata in greater detail would be a logical next step in this investigation. If radial callose arrays are found to be responsible for stomatal closure, the question of the function of tip wall callose remains. An adhesive role between the guard cells seems unlikely based on our current understanding of callose deposition, though some mechanical effect is possible. If no radial callose arrays can be observed, we may return to trying to understand how callose in the tip wall could effect stomatal closure without affecting stomatal opening.

Our data suggest that pectic HG has additional functions in stomata alongside the flexibility role that we reported previously (Amsbury et al. 2016). The polar deposits of demethylesterified HG co-localise with the points of greatest stiffness observed by AFM, and may be related to constraining the length of the stomatal complex, though the mechanism by which this might take place is unclear. Pinning of the stomatal poles to underlying tissue seems unlikely given the position of many stomata over large air cavities. Balancing turgor pressure against the surrounding epidermal cells is also a problematic explanation as the stomatal

complex is able to change in width. Perhaps the thickened inner walls of the stomata help to prevent the complex from stretching in that direction. Further development of computational models could help us to simulate such effects (Carter et al. 2017; Woolfenden et al. 2017). However, testing these ideas is particularly challenging given the persistent nature of the pectin deposit in question, which resists enzyme degradation, or at the very least is less readily degraded than other surrounding pectins.

We conducted an antibody labelling screen to help us select which cell wall components to target in our reverse genetics work. However, our observations of epitope distributions, and particularly of various forms of HG, raise questions about the precise mechanism by which large airspaces open up in the mesophyll. Parenchyma cells, including those of the mesophyll, separate early in development to form small airspaces. As cells tend towards a sphere, the lowest energy shape, reinforcing zones at the corners of the airspace are required to provide the mechanical strength to prevent uncontrolled cell separation (Jarvis 1998). Growth of airspaces could involve deposition of new cell wall material on either side of static reinforcing zones (delivery of material to adhered and separated walls), or could be mediated by 'unzipping' of the middle lamella, with a gradually shifting reinforcing zone progressing along the adhered wall by cell wall remodelling. We observed strong LM20 signal (highly methylesterified HG) at the airspace corners, which is unexpected given the reported abundance of less methylesterified epitopes in reinforcing zones (Jarvis et al. 2003). Perhaps these sites could also be foci for delivery of new wall material. Labelling of reinforcing zones with additional mAbs not included in our screen, such as LM7, might provide further insights (Willats et al. 2001). Fully resolving these questions would be most readily achieved by real-time imaging of cell wall dynamics (Altartouri & Geitmann 2015).

We collected mutants in pectin biosynthesis, delivery and modification with the intention of investigating structure-function relationships in the leaf. However, the limited number of mutants that we identified provided a relatively small range of structural variation. The *pme3* mutant is yet to be structurally characterised, but comparison of this line to the *qua2* line could provide new insights into the relative importance of HG methylesterification pattern and HG abundance in the context of mesophyll development.

Finally, structure-function data from our panel of mutants in stomatal patterning and function did not provide clear evidence for g_s -based modulation of palisade porosity as we hypothesised, but neither did they disprove this idea. Performing similar experiments under stress conditions (e.g. drought) might reveal effects that were not apparent under ambient conditions. The relationship between stomatal index and cell surface area in the spongy and palisade layers also requires further attention. Growing plants under different environmental

conditions, such as different light levels, to generate a wider range of mesophyll structures would allow us to test whether this relationship holds more broadly.

It is difficult to predict which aspects of this work can be applied to other plant species. The specific cell wall components involved in mesophyll differentiation are likely to be less relevant in less closely related clades. The monocotyledons are well known to have very distinct cell wall composition, but *Arabidopsis* is thought to be a reasonable model for a wide range of dicotyledonous species (Zabackis et al. 1995). Observations on the relationship between cellular architecture and physiological function are also likely to be most relevant to the most structurally similar species. Our conclusions are unlikely to apply to plants with non-C3 metabolism, but C3 species including monocotyledons may show a similar fundamental relationship between the amount and distribution of airspace and their gas exchange and photosynthesis. Projects on monocotyledonous crop species are already underway in our research group using the same approach of paired microCT and LICOR measurements. This perhaps begs the question of the value of such studies in non-crop plants such as *Arabidopsis*. Besides its close relationship to a number of non-cereal crops, the rapid generation time and unrivalled genetic resources available for this species still make it an excellent choice for addressing fundamental questions in developmental biology.

Chapter 7 Materials and Methods

7.1 Plant material

The Col-0 ecotype of *Arabidopsis thaliana* was used for agrobacterium transformations, descriptive work and controls for comparison to mutant lines.

qua1 (At3G25140) and *qua2* (At1G78240) mutants were obtained from Gregory Mouille (INRA, Versailles), *arp3* (At1G13180) from Firas Bou Daher (Sainsbury Laboratory, Cambridge) and all of the lines in Chapter 5 (*Col-2*, *focl1-1*, *Stomagen overexpression*, *Stomagen RNAi*, *EPF2 overexpression* and *epf1/2* double knockout) from Lee Hunt (University of Sheffield).

The *GSL8* (At2G36850) inducible knockout line was obtained from Jae-Yean Kim, (Gyeongsang National University, Chinju). Plants were induced 24h prior to their use in any experiment by painting 10µm dexamethasone in DMSO onto both surfaces of the leaf. Control plants were mock induced with DMSO only. Col-0 plants were also treated with inducer and mock-inducer as a further control.

Knockout lines in nine pectin methylesterase (*PME*) genes were obtained from NASC (**Table 3-1**) and were verified by genotyping (below). Seeds of heterozygous plants were propagated and selfed, and the following generation genotyped again to identify plants homozygous for the mutation. Plants grown for characterisation were also genotyped to re-confirm their identity given the absence of any obvious visual phenotypes at the whole-plant level.

Novel transgenic lines generated during this project were characterised at the T₃ generation. A segregating sister line was available as a control for each of the homozygous mutants.

7.2 Plant growth

7.2.1 Growth on agar plates

Arabidopsis seeds for selection, for the immuno-labelled development series, and for seed collection were sterilised in a 1/5 dilution of economy bleach in water, with a drop of tween-20 (Sigma) for large aliquots of seed. After stratification in the dark at 4°C for 5-9 days they were sown on 1/2 MS agar (0.22% (w/v) MS salts (Sigma), 1% (w/v) sucrose (Sigma), 0.8% (w/v) plant agar (Duchefa Biochemie), 0.05% (w/v) MES (Sigma), pH5.8), supplemented with antibiotics as required (20µg/mL hygromycin for selection, plus 25µg/mL cefotaxime for selection of T₁ plants generated by floral dip) in 120x120x17mm plates. Plants were germinated in a controlled environment chamber (Snijders, Netherlands) under long day conditions (16h

light/8h dark, 22°C, 150 $\mu\text{mol m}^{-2} \text{s}^{-1}$ PPFD) and maintained on plates for two weeks before survival counts, characterisation or transfer to compost.

7.2.2 Growth on compost

Arabidopsis grown for seed were transplanted from plates 14 days after germination into 50x50x50mm pots of damp, lightly compressed compost (3:1 Levington M3 compost:perlite) and placed in a controlled environment chamber (Conviron, Canada) under long day conditions (16h-light, 22°C, 150 $\mu\text{mol m}^{-2} \text{s}^{-1}$ PPFD, 60% humidity). Newly transplanted seedlings were placed under a transparent, ventilated lid for two days to elevate humidity and aid establishment. Seed was collected using aracons and aratubes to avoid cross-pollination and seed contamination (Arasystem, Belgium).

Arabidopsis for floral dipping were grown as above but in 100mm diameter round pots with 4-5 plants per pot. Bolting stems were cut to encourage bushy growth with many flowers.

Arabidopsis for phenotypic analysis were sown directly into 60x60x80mm pots of damp, lightly compressed compost (3:1 Levington M3 compost:perlite, except Chapter 5, M3 only) and stratified at 4°C for 5-7days before transfer into a controlled environment chamber (Conviron, Canada) under short day conditions (12h-light 22°C/12h dark 15°C, 200 $\mu\text{mol m}^{-2} \text{s}^{-1}$ PPFD, 60% humidity). Plants remained under a transparent lid or in a transparent bag to elevate humidity and aid germination and establishment for seven days, after which the lid was propped, or the bag opened, for a further two days before complete removal. Seedlings were thinned to one plant per pot nine days after germination. Plants were watered regularly and lines were mixed within trays to minimise effects of any watering variation between trays. Plants were typically characterised five weeks after germination unless otherwise specified.

7.3 Genotyping

7.3.1 Extraction of genomic DNA

Flash-frozen leaf tissue was ground in liquid nitrogen, suspended in 500 μl shorty buffer (0.2M Tris/HCl pH9, 0.4M LiCl, 0.025M EDTA, 1% (w/v) SDS) then pelleted by centrifugation (10min, 13000rpm). The supernatant was mixed with an equal volume of isopropanol and centrifuged again. This supernatant was discarded, and the pelleted DNA washed with 70% ethanol and centrifuged once more. DNA was re-suspended in TE buffer (0.01M Tris/HCl pH 7.5, 0.01M EDTA) and stored at 4°C for at least 24 hours before use.

7.3.2 PCR reaction

All genotyping PCR reactions were conducted using Taq DNA polymerase (NEB) in its standard buffer, according to manufacturer's instructions. 2µl of extracted gDNA was used as the template.

Primers for genotyping seed lines ordered from NASC were designed using the online t-DNA express tool. Primers used for genotyping transgenic lines generated during this project are listed in **Table 7-1**.

7.3.3 Agarose gel electrophoresis

5µl PCR product was mixed with 1µl loading dye (0.25% (w/v) bromophenol blue, 0.025% (w/v) xylene cyanol, 30% (v/v) glycerol) and run on a gel of 1.5% (w/v) agarose dissolved in TAE buffer (40mM Tris, 20mM acetic acid, 1mM EDTA) with 0.5µg/mL ethidium bromide. Gels were visualised and imaged with a Uvitec gel documentation system.

7.4 Generation of tissue-specific PME1 overexpression lines

7.4.1 Amplification of PME1 coding sequences

Q5 polymerase (NEB) was used for all cloning PCR reactions. The full length coding sequences of *AdPME1*, *AtPME1* and *AtPME2* were amplified from gDNA of kiwifruit (*Actinidia deliciosa*)/Arabidopsis respectively, extracted from fruit/leaf tissue respectively as described (7.3.1). Primers used in the cloning process are listed in **Table 7-1**. The forward primers included the 5' CACC modification to allow cloning into the pENTR/D-TOPO Gateway entry vector. The PCR products were purified from 1.5% agarose gel (7.3.3) using a Quiagen spin kit, according to the manufacturer's instructions. As there are a number of *AdPME1* genes with very similar sequences it was not possible to design non-redundant primers, so the specific gene was identified from the sequence of the entry clone.

7.4.2 Cloning

PCR products were combined into the pENTR/D-TOPO Gateway entry vector (Invitrogen) then transformed into DH5α *E. coli* cells (Invitrogen) by heat shock according to the manufacturer's instructions. Cells were plated on LB media (1% (w/v) Bacto-trypton (Fluka), 0.5% (w/v) Bacto-yeast-extract (Melford), 1% (w/v) NaCl (BDH), 1.5% (w/v) Bacto-agar (Melford), pH 7) containing kanamycin (50µg/mL) and incubated overnight at 37°C. Colonies were checked for presence of the insert by PCR with same primers initially used to amplify the insert, and positive colonies were cultured overnight in 5mL LB liquid containing kanamycin (50µg/mL).

Plasmid DNA was extracted by miniprep (Quiagen spin kit) according to manufacturer's instructions and verified by sequencing with both insert primers (GATC sequencing).

As the entry and destination vectors were both kanamycin resistant, the entry vector was digested with Nsi1 (NEB) and gel purified (Quiagen spin kit) before carrying out the LR reaction. Inserts were transferred from the pENTR/D-TOPO Gateway entry vector into the pMDC32 destination vector (Curtis & Grossniklaus 2003) using Gateway LR Clonase II according to manufacturer's instructions (Invitrogen). Transformation into *E. coli*, PCR checks, overnight cultures and minipreps were as described above. Inserts were sequenced using the original insert-cloning primers.

Table 7-1: Primers used during the cloning process

Primer	Purpose	Sequence (5' – 3')
AtPMEI1_F	Cloning Arabidopsis PMEI1 gene	CACCATGGCTGCGAATC
AtPMEI1_R	Cloning Arabidopsis PMEI1 gene	TTAATTACGTGGTAACATGTTAGAG
AtPMEI2_F	Cloning Arabidopsis PMEI2 gene	CACCATGGCAGCATACTGACGAACAGAG
AtPMEI2_R	Cloning Arabidopsis PMEI2 gene	TCACATCATGTTTGAGATGAC
AdPMEI_F	Cloning Kiwi PMEI1 gene	CACCATGGCCTTTTCCTATTG
AdPMEI_R	Cloning Kiwi PMEI1 gene	CTATTTTGATCCAGGCAAAG
pCA1_F_Pme1	Cloning pCA1 promoter with restriction site	CCGTTTAAACAAGGACTCACCAGGACAGGA
pCA1_R_BamH1	Cloning pCA1 promoter with restriction sites	GGCGGATCCTACTCACACCCTTGCTTAAT
pCA1_sequencing_F	Reads through the promoter- insert join	TTCATAGGAAAGCGGACGAG

7.4.3 Promoter swap

A promoter specific to the mesophyll (pCA1; (Gowik et al. 2004)) was amplified by PCR (see **Table 7-1** for primers) from a vector that was already available in the lab (pAMPAT-GW+pCA1). The PCR product was extracted from a 1.5% agarose gel (Quiagen spin kit). The primers incorporated restriction enzyme sites to facilitate subsequent steps. The gel-extracted PCR product was sequentially digested with Pme1 and BamH1 enzymes (NEB) but failed to ligate directly into the pMDC32 derivative vectors after direct digestion of the PCR product. Instead it was polyadenylated by incubation with 0.2mM dATP and standard taq in its buffer for 15 mins at 72°C and sub-cloned into the TOPO-TA Gateway vector (Invitrogen), from which it was digested with Pme1 and BamH1. The modified pMDC32 vectors containing each *PMEI* gene were cut with the same enzymes to remove the 35S promoter, and dephosphorylated with shrimp alkaline phosphatase according to manufacturer's instructions (NEB) to prevent re-ligation. The pCA1 promoter was ligated into each *PMEI*-containing vector with T4 DNA ligase according to manufacturer's instructions (NEB) and the resulting plasmids were amplified in *E. coli* as described above and verified by sequencing with the promoter-forward primer and the insert reverse primer.

7.4.4 Transformation of agrobacteria

Plasmids were transformed into agrobacteria strain C58C1 (lab stocks) by electroporation and plated on half-salt LB medium containing rifampicin (50µg/mL) and kanamycin (25µg/mL). Plates were incubated at 28°C. After 2-3 days a single colony was picked per construct with which to inoculate a 5mL overnight culture in half-salt LB liquid containing antibiotics as described above.

Samples were taken from the large culture used for dipping (below) to make glycerol stocks (200µl culture in 800µl 80% glycerol), for long-term storage at -80°C, and for minipreps (Quiagen spin kit), which were sent for sequencing with the 'promoter sequencing forward' and 'insert reverse' primers (**Table 7-1**).

7.4.5 Plant transformation

Col-0 Arabidopsis plants were grown on ½ MS agar for two weeks then transferred to compost for a further 2-3 weeks before transformation by the floral dip method (Clough & Bent 1998). 15-20 plants were transformed with each construct. Existing siliques were removed from the plants before dipping to increase the proportion of transformed seed. 200mL cultures (half-salt LB liquid and antibiotics as above) were inoculated from minicultures and incubated overnight (28°C, 200rpm). Cells were pelleted for 30 mins at 4°C, then re-suspended in MS solution (0.22% (w/v) MS salts, 5% (w/v) sucrose, 0.05% (w/v) MES, 0.05% (v/v) Silwet L-77). Shoots were immersed in the solution then laid in trays of damp tissue and covered with cling-film to

elevate humidity. After 24h, plants were stood up, enclosed in aratubes and watered as normal.

7.4.6 Generation of homozygous lines

T₁ seeds were sterilised (10min in 20% (v/v) economy bleach then three rinses in sterile water), stratified (7days, 4°C) and plated on plant MS agar with antibiotics (7.2.1). After 14 days, 15-20 surviving plants per line were potted on. A leaf sample was taken from each T₁ plant for genotyping with the 'promoter sequencing forward' primer and the 'insert reverse' primer (**Table 7-1**). The minipreps from the cultures used for transformation were used as positive controls.

T₁ plants with a positive genotyping result were grown for seed. At least 50 seeds were plated on ½ MS agar with antibiotics to examine the germination ratio. Plant lines with a 60-80% survival rate on antibiotics were taken forward; plants with higher survival may deviate from the expected Mendelian 3:1 ratio due to multiple insertions. The antibiotic-grown seedlings were discarded and more T₂ seed sown on ½ MS agar so that segregating sister lines could also be grown. For each line, 12 plants were potted on and grown for seed.

T₃ seeds were sown on ½ MS agar with antibiotics (~20 seeds/line) to identify homozygous mutants (100% survival) and segregating sister lines (0% survival). T₃ seeds of chosen lines were sown on compost for characterisation.

7.5 Enzymatic degradation of cell walls of intact tissue

Leaf tissue from compost-grown Col-0 Arabidopsis was treated in a buffer solution (10mM MES pH6.2, 10mM KCl, 0.1mM CaCl₂) containing 5% (v/v) endo-polygalacturonase M2 (Megazyme), 5% (v/v) endo-cellulase EGII (Megazyme), 5% (v/v) β(1,3)-D-glucanase (Sigma) or no enzyme, for four hours at room temperature. For immunolabelling, 6mm discs were submerged in the enzyme treatment or buffer control then embedded whole. For bioassays, whole leaves were floated onto the treatment or buffer abaxial side down, and epidermal peels were taken post-treatment.

7.6 Immunohistochemistry

7.6.1 Fixing, embedding and sectioning

Samples were fixed in 4% (w/v) formaldehyde in PEM buffer (1.5% (w/v) Pipes, 0.19% (w/v) EGTA, 0.124% (w/v) MgSO₄, pH 7) by vacuum infiltration. After three 10-min rinses in PEM, samples were stored at 4°C until dehydration in an ascending ethanol series (10%, 30%, 50%, 70%, 100% (v/v) EtOH – 1h in each). Samples were then infiltrated with LR white resin (London Resin Company) in an ascending resin series (10%, 20%, 30%, 50%, 70%, 90%, 100% (v/v) resin

in EtOH – 1h each and 3x 8+ hours in 100%). Samples were stored at 4°C between resin changes. Finally samples were stood vertically in gelatine capsules filled with resin and left to polymerise for at least 5 days at 37°C. 2µm sections were cut using the Reichert-Jung Ultracut E ultramicrotome and allowed to dry onto vectabond-coated multi-well slides.

7.6.2 Immunolabelling

Sections were incubated for 30 mins with 3% (w/v) milk protein ('Marvel', Premier Beverages, UK) solution in PBS buffer (8% (w/v) NaCl, 0.2% (w/v) KCl, 1.44% (w/v) Na₂HPO₄, 0.24% (w/v) KH₂PO₄) to block non-specific antibody binding. After a 5min incubation in PBS, sections were incubated with a 1/10 dilution of the chosen primary monoclonal antibody in the milk protein solution (1h). Milk protein solution without added antibody was used as a negative control. After three further PBS washes (5min each) the sections were incubated with a 1/100 dilution of the secondary antibody, anti-rat FITC (Sigma-Aldrich) in milk protein solution. From this point onward slides were kept in the dark. Following three further PBS washes (5 mins each) the sections were incubated with a 1/10 dilution of 0.25% Calcofluor white (Fluorescent brightener 28; Sigma-Aldrich) in PBS (5 mins): this counterstain allows visualisation of all cell walls. After three successive PBS washes the glycerol-based anti-fade solution Citifluor AF1 (Agar Scientific) was used to mount the coverslips.

7.6.3 Chemical and enzymatic pre-treatments

Sections were incubated for 2h in 0.1M sodium carbonate solution (pH 11.4) then washed twice in PBS buffer (10 mins each). Pectate lyase (10µg/mL; Megazyme) in CAPS buffer (0.221% (w/v) CAPS, 10% (v/v) methanol, pH 11) was then applied (2h incubation). After three further PBS washes, the slides were immunolabelled as described above. Control slides were incubated in CAPS buffer without the enzyme. Untreated slides and slides subjected only to the NaCO₃ treatment were included as further controls.

7.6.4 Imaging

The initial screening of small and mature leaf sections was imaged using an Olympus BX61 microscope equipped with a Hamamatsu ORCA 285 digital camera, and images were captured using Velocity Imposition software. All other imaging of immunolabelled sections was carried out using an Olympus BX51 microscope and Olympus DP71 camera equipped with a COOLED fluorescence system, and images were captured using Cell B software. All labelling experiments were replicated at least in duplicate both technically and biologically.

7.7 Stomatal density and index

Leaf tissue was fixed in 9:1 EtOH: acetic acid solution by vacuum infiltration, then rinsed in 90% EtOH (v/v) in H₂O. Tissue was cleared by immersion in chloral hydrate (2.5g/mL) in 30% (v/v)

glycerol and mounted in the same solution. Slides were viewed on an Olympus BX51 microscope with Olympus DP71 camera, set up for Nomarski imaging, and images were captured using Cell B software. Four areas were imaged per leaf. Stomata and epidermal cells were counted using the Image J Cell Counter plugin for the calculation of stomatal density and index:

$$\text{Stomatal density} = \frac{N^{\circ} \text{ Stomata}}{\text{Area}}$$

$$\text{Stomatal index} = \frac{N^{\circ} \text{ Stomata}}{(N^{\circ} \text{ Stomata} + N^{\circ} \text{ Epidermal cells})} \times 100$$

7.8 Aniline blue imaging

Fresh leaf tissue was immersed in aniline blue solution (0.05% (w/v) aniline blue in 0.07M sodium phosphate buffer, pH9) overnight. Samples were viewed on a Leica DM6 fluorescence microscope using 365nm excitation from the CoolLED system and a DAPI filter, and imaged using Leica Application Suite X Software.

7.9 COS⁴⁸⁸ probe imaging

Intact, enzyme-treated leaf tissue or sections of tissue embedded after enzyme treatment were immersed in a 1/1000 dilution of the COS⁴⁸⁸ probe (Mravec et al. 2014) in 0.5% MES pH8.5 for 15 mins in the dark. Images were obtained on an Olympus BX51 microscope with a DP71 digital camera and CoolLED fluorescence system and cell B software or an Olympus FV1000 confocal microscope with Olympus Fluoview software (488nm laser excitation, 515-550nm emission recorded).

7.10 Response of stomatal aperture to CO₂

Epidermal peels were taken from the abaxial surface of six leaves per treatment or genotype (except *GSL8-RNAi* bioassay, five leaves per treatment), five weeks after germination unless otherwise specified, and at least two hours into the photoperiod. Peels were floated onto a buffer to induce opening (50mM KCl, 10mM MES pH6.2) and maintained at 22°C with 200µmolm⁻²s⁻¹ PPFD. CO₂ free, CO₂ ambient or 1000ppm CO₂-enriched air was bubbled through the buffer. After 2.5 hours, epidermal peels were imaged on an Olympus BX51 microscope with a DP71 digital camera with Cell B Software. 14 mature stomata (length/width>1) were measured per plant using Image J software. Pore area and complex area were estimated from their respective width and length measurements according to the following equation. Pore area is divided by complex area to account for any differences in stomatal size.

$$\text{Area} = \frac{\pi \times \text{width} \times \text{length}}{2}$$

For statistical analyses, see 7.14.

7.11 Gas exchange/fluorescence measurements

7.11.1 *qua1*, *qua2*, *arp3* and Col-0

The measurements presented in Chapter 3 were taken in the growth chamber to minimise acclimation time, using a LI-6800XT portable photosynthesis system (LICOR, USA) equipped with a fluorescence head. Large, mature leaves from five-week-old plants were selected for measurement. Plants were acclimated for at least 20 mins at the start condition for each response curve. CO₂ response curves were performed in two sections, with 150µmol s⁻¹ flow and 90-180s wait time for the initial descending part (CO₂ reference = 400, 300, 200, 150, 100, 75, 50, 25, 0ppm) and 300µmol s⁻¹ flow with 180-300s wait for the ascending part (CO₂ reference = 400, 500, 600, 700, 900, 1200, 1500ppm). Light response curves were performed at least one day later with descending irradiance (PPFD = 1400, 1200, 1000, 800, 600, 500, 400, 300, 200, 100, 75, 50, 25, 0 µmol m⁻² s⁻¹, 10% blue light) with 420-900 secs wait time and 400µmol s⁻¹ flow rate. All measurements were taken at leaf chamber RH 60% with block temperature 21°C and fan speed 10000rpm.

7.11.2 Stomatal patterning and covering mutants

Measurements presented in Chapter 5 for lines Col-2, *focl1-1*, *STOM-RNAi* and *STOM-oex* were collected previously by Dr Marjorie Lundgren, and lines *EPF2-oex* and *epf1/2* were a novel addition to that data set. Measurements were taken in a laboratory, not inside the growth chamber, using a LI-COR-6400 portable photosynthesis system (LI-COR, USA) equipped with fluorescence head. Large, mature leaves from five-week-old plants were selected for measurement. Fluorescence and gas-exchange data were collected simultaneously. Plants were acclimated for at least 20 mins at 400ppm CO₂ sample, 1200µmol m⁻² s⁻¹ PPFD and 250µmol s⁻¹ flow rate. CO₂ response curves were conducted in two parts, first descending (CO₂ reference = 400, 250, 150, 100, 80, 60, 40ppm) with a wait time of 120-180 secs and a flow rate of 200µmol s⁻¹, then ascending (CO₂ reference = 500, 600, 700, 800, 900, 1000, 1200, 1400, 1600ppm) after re-acclimation at 400ppm with a wait time of 180-300 secs and a flow rate of 300µmol s⁻¹. Plants were then acclimated at CO₂ sample 1000ppm. A descending irradiance light response curve was conducted (PPFD = 1200, 1000, 750, 500, 250, 150, 100, 75, 50, 25, 0 µmol m⁻² s⁻¹, 10% blue light) with a wait time of 180-360 secs and flow rate of 300µmol s⁻¹. Humidity was maintained at around 60% and leaf temperature was controlled at 21°C throughout measuring, with the 'fast' leaf fan speed option selected. A₄₀₀ and g_{s400}(assimilation and stomatal conductance) were based on the acclimated values at CO₂ reference = 400 and other photosynthetic parameters were extracted using a curve-fitting tool (Bellasio et al. 2016).

7.12 Micro Computed Tomography

7.12.1 Image capture

Leaves used for gas exchange analysis were subsequently imaged using an X-ray microCT scanner (Nanotom General Electric Company, USA) at the Hounsfield Facility, University of Nottingham. MicroCT imaging was performed as described in Dorca-Fornell et al. (2013) and data were processed according to a slightly modified protocol described in full below.

A 5mm diameter leaf disc from one side of the midrib was scanned according to the settings in **Table 7-2**.

Table 7-2: Settings used for microCT scanning of Arabidopsis leaf discs

Settings	Chapter 4 <i>(qua1, qua2, arp3 and Col-0)</i>	Chapter 5 <i>(Stomatal patterning and covering mutants)</i>
Voltage (kV)	65	65
Current (μ A)	140	140
Projections	2400	2400
Exposure (mSec)	750	750
Acquisition time (mins)	30	30
Bin	1/1	1x1
Avg/Skip	1/0	1/0
Resolution (μ m)	2.75	2.75

7.12.2 Image analysis

Radiographs acquired by scanning were horizontally aligned in Volume Graphics software (V2.2) and cropped to remove areas at the edge of the leaf damaged by the leaf borer. A mask was generated in Aviso Fire (V6.0) to define the boundaries of the leaf volume.

Horizontally aligned image stacks were thresholded in Image J using the 'ISODATA' or 'IJ_ISODATA' algorithm and outliers were removed from both the dark and the bright areas, with the threshold value for outlier size selected by manual comparison to the greyscale stack. The mask was used to remove the background from the image, resulting in a binary representation of the leaf material and internal air channel space. A 400px square selection

(1.1x1.1mm) was made for analysis, being careful to exclude damaged areas of tissue and, as far as possible, larger veins.

The mask area, the air channel number and area, and the perimeter of each airspace, were calculated for each z-slice by running the 'Analyse Particles' function in Image J. Area measurements are converted to volumes by multiplying them by the resolution. Porosity was calculated as the proportion of the mask volume accounted for by air channels in each slice and averaged across the leaf to give mean porosity:

$$Porosity = \left(\frac{Volume_{pores}}{Volume_{mask}} \right) \times 100$$

The surface area of cells exposed to airspace was calculated per unit leaf volume by summing the perimeter of all channels, multiplied by the scan resolution, and dividing by the mean total mask volume:

$$Exposed\ cell\ surface\ area = \frac{\sum Pore\ perimeter}{Total\ mask\ volume}$$

Channel diameter was calculated using the Bone J plugin (Doubé et al. 2010). This provides the maximum channel diameter and the mean with standard deviation for the whole leaf volume, and a heat mapped representation of channel sizes. Heat maps were normalised across each experiment to produce comparative images using a custom macro but are not presented here.

3D renderings of the cell and airspace were constructed in VG software (V2.2) by Dr Andrew Mathers.

Channel density was calculated by summing the total number of channels, reported by the 'Analyse Particles' function, and dividing by the leaf volume.

Where separate spongy and palisade mesophyll values are reported, these are based on a single representative slice. Despite aligning the leaves horizontally, there were always very few slices that were both clearly composed exclusively of one mesophyll tissue type, and entirely within the masked volume. Representative palisade slices were selected by visual inspection according to these criteria, though occasionally a slice had to be included that did not fill the full area inside the mask. For the spongy mesophyll, the slice with the maximum porosity value was selected since plots of porosity over the depth of the leaf consistently showed a pronounced peak in the spongy mesophyll.

7.13 Atomic Force Microscopy

Atomic Force Microscopy (AFM) of leaf tissue was performed as described (Carter et al. 2017). 5mm square explants of buffer or enzyme-treated leaf tissue were plasmolysed in 0.55M mannitol for at least 45 mins before measuring with a Neon Wizard 3 AFM (JPK Instruments, Germany). Samples were probed with a 5nm diameter pyramidal indenter (Windsor Scientific, UK) on a cantilever of 45N/m stiffness, determined by thermal tuning. Tip sensitivity varied between experiments so was calibrated by performing indentations on a clean glass slide. In each sampled region, 128x128 points were indented over a 100 μm^2 area. All sampled areas were on the adaxial leaf surface. Samples were indented with 1000nN of force, resulting in indentation depths of 100-1000nm. JPKSPM Data Processing software (V. spm. 5.0.69) was used to analyse the force-indentation curves by the following steps: conversion of voltage readings to force using calibrated sensitivity and cantilever stiffness values; baseline subtraction and tilt correction; vertical displacement offset adjustment; indentation calculation (subtraction of cantilever bending from piezo position), and indentation modulus calculation by fitting a Hertzian indentation model to the approach curve. Results are quoted as apparent modulus (E_a) because the leaf surface does not fulfil the heterogeneity assumption of the Hertzian model. All AFM images are displayed as heat maps with a scale bar to indicate the range of E_a represented in the image.

7.14 Statistical Analyses

One-way ANOVA was performed to test for differences in stomatal density, structural parameters measured by microCT and gas-exchange/fluorescence values. If significant differences were detected, this was followed by multiple comparisons by Tukey's Honest Significant Difference test. These tests were carried out using Graphpad Prism software (V7).

Stomatal aperture changes in response to different CO₂ concentrations were analysed by two-way ANOVA followed by a set of planned comparisons (Tukey's Honest Significant Difference tests) using the 'Multcomp' package in R software (RStudio V3.4.2). Within each plant line or enzyme treatment, values at low and high CO₂ were compared to values at ambient CO₂. Within each CO₂ treatment, values for each plant line or treatment were compared to the control (Col-0 plant line (mock-induced where applicable)/buffer-treated plants in enzyme-treatment experiment). P values were adjusted to account for the number of comparisons.

Linear regression analyses (Chapter 5) were carried out in Graphpad Prism software (V7).

Bibliography

- Altartouri, B. & Geitmann, A., 2015. Understanding plant cell morphogenesis requires real-time monitoring of cell wall polymers. *Current Opinion in Plant Biology*, 23, pp.76–82.
- Amsbury, S. et al., 2016. Stomatal function requires pectin de-methyl-esterification of the guard cell wall. *Current Biology*, 26(21), pp.1–8.
- Anderson, C.T., 2016. We be jammin': an update on pectin biosynthesis, trafficking and dynamics. *Journal of Experimental Botany*, 67(2), pp.495–502.
- Apostolakos, P. et al., 2010. Callose implication in stomatal opening and closure in the fern *Asplenium nidus*. *New Phytologist*, 186(3), pp.623–635.
- Assmann, S.M. & Jegla, T., 2016. Guard cell sensory systems: recent insights on stomatal responses to light, abscisic acid, and CO₂. *Current Opinion in Plant Biology*, 33, pp.157–167.
- Atmodjo, M.A., Hao, Z. & Mohnen, D., 2013. Evolving views of pectin biosynthesis. *Annual Review of Plant Biology*, 64, pp.747–79.
- Balestrieri, C. et al., 1990. A glycoprotein inhibitor of pectin methylesterase in kiwi fruit (*Actinidia chinensis*). *European Journal of Biochemistry*, 193(1), pp.183–187.
- Bellasio, C., Beerling, D.J. & Griffiths, H., 2016. An Excel tool for deriving key photosynthetic parameters from combined gas exchange and chlorophyll fluorescence: theory and practice. *Plant, Cell and Environment*, 39(6), pp.1180–1197.
- Benitez-Alfonso, Y. et al., 2013. Symplastic intercellular connectivity regulates lateral root patterning. *Developmental Cell*, 26(2), pp.136–147.
- Bergmann, D.C. & Sack, F.D., 2007. Stomatal development. *Annual review of plant biology*, 58, pp.163–181.
- Bethke, G. et al., 2014. Arabidopsis PECTIN METHYLESTERASEs contribute to immunity against *Pseudomonas syringae*. *Plant Physiology*, 164(2), pp.1093–1107.
- Bosch, M., Cheung, A.Y. & Hepler, P.K., 2005. Pectin methylesterase, a regulator of pollen tube growth. *Plant Physiology*, 138(3), pp.1334–1346.
- Bosch, M. & Hepler, P.K., 2005. Pectin methylesterases and pectin dynamics in pollen tubes. *The Plant Cell*, 17(12), pp.3219–3226.
- Bouton, S. et al., 2002. QUASIMODO1 encodes a putative membrane-bound

glycosyltransferase required for normal pectin synthesis and cell adhesion in Arabidopsis. *The Plant Cell*, 14(10), pp.2577–2590.

- Braybrook, S.A. & Jonsson, H., 2016. Shifting foundations: the mechanical cell wall and development. *Current Opinion in Plant Biology*, 29, pp.115–120.
- Braybrook, S. & Kuhlemeier, C., 2010. How a plant builds leaves. *The Plant Cell*, 22(4), pp.1006–1018.
- Caffall, K. & Mohnen, D., 2009. The structure, function, and biosynthesis of plant cell wall pectic polysaccharides. *Carbohydrate Research*, 334(14), pp.1879–1900.
- Carter, R. et al., 2017. Stomatal opening involves polar, not radial, stiffening of guard cells. *Current Biology*, 27(19), pp.1–10.
- Casson, S. a & Hetherington, A.M., 2010. Environmental regulation of stomatal development. *Current Opinion in Plant Biology*, 13, pp.90–5.
- Chen, X.-Y. & Kim, J.-Y., 2009. Callose synthesis in higher plants. *Plant Signaling & Behavior*, 4(6), pp.489–492.
- Chen, X.-Y.Y. et al., 2009. The Arabidopsis callose synthase gene *GSL8* is required for cytokinesis and cell patterning. *Plant Physiology*, 150(1), pp.105–113.
- Clausen, M.H. et al., 2004. A monoclonal antibody to feruloylated-(1->4)-beta-D-galactan. *Planta*, 219(6), pp.1036–41.
- Clough, S.J. & Bent, A.F., 1998. Floral dip: a simplified method for *Agrobacterium*-mediated transformation of *Arabidopsis thaliana*. *The Plant Journal*, 16(6), pp.735–743.
- Cosgrove, D.J., 2014. Re-constructing our models of cellulose and primary cell wall assembly. *Current Opinion in Plant Biology*, 22, pp.122–131.
- Curtis, M.D. & Grossniklaus, U., 2003. A Gateway cloning vector set for high-throughput functional analysis of genes in planta. *Plant Physiology*, 133(2), pp.462–469.
- Daher, F.B. & Braybrook, S. a., 2015. How to let go: pectin and plant cell adhesion. *Frontiers in Plant Science*, 6(523).
- Dorca-Fornell, C. et al., 2013. Increased leaf mesophyll porosity following transient retinoblastoma-related protein silencing is revealed by microcomputed tomography imaging and leads to a system-level physiological response to the altered cell division pattern. *The Plant Journal*, 76(6), pp.914–929.
- Dorokhov, Y.L. et al., 2006. Role of the leader sequence in tobacco pectin methylesterase secretion. *FEBS Letters*, 580(13), pp.3329–3334.

- Doube, M. et al., 2010. BoneJ: Free and extensible bone image analysis in ImageJ. *Bone*, 47(6), pp.1076–1079.
- Dow, G.J. & Bergmann, D.C., 2014. Patterning and processes: how stomatal development defines physiological potential. *Current Opinion in Plant Biology*, 21, pp.67–74.
- Dow, G.J., Berry, J.A. & Bergmann, D.C., 2017. Disruption of stomatal lineage signaling or transcriptional regulators has differential effects on mesophyll development, but maintains coordination of gas exchange. *New Phytologist*, 216(1), pp.69–75.
- Dyachok, J. et al., 2008. Plasma membrane-associated SCAR complex subunits promote cortical F-actin accumulation and normal growth characteristics in Arabidopsis roots. *Molecular plant*, 1(6), pp.990–1006.
- Efroni, I. et al., 2008. A protracted and dynamic maturation schedule underlies Arabidopsis leaf development. *The Plant Cell*, 20(9), pp.2293–2306.
- Efroni, I., Eshed, Y. & Lifschitz, E., 2010. Morphogenesis of simple and compound leaves: a critical review. *The Plant Cell*, 22(4), pp.1019–1032.
- Ellis, M. et al., 2010. Arabinogalactan-proteins: key regulators at the cell surface? *Plant Physiology*, 153(2), pp.403–19.
- Evans, J.R. et al., 2009. Resistances along the CO₂ diffusion pathway inside leaves. *Journal of Experimental Botany*, 60(8), pp.2235–2248.
- Fleming, A.J., 2005. The control of leaf development. *New Phytologist*, 166(1), pp.9–20.
- Flexas, J. et al., 2008. Mesophyll conductance to CO₂: current knowledge and future prospects. *Plant, cell & environment*, 31(5), pp.602–21.
- Francocci, F. et al., 2013. Analysis of pectin mutants and natural accessions of Arabidopsis highlights the impact of de-methyl-esterified homogalacturonan on tissue saccharification. *Biotechnology for Biofuels*, 6(163).
- Frank, M. et al., 2002. TUMOROUS SHOOT DEVELOPMENT (TSD) genes are required for coordinated plant shoot development. *The Plant Journal*, 29(1), pp.73–85.
- Franks, P.J. et al., 2001. Guard Cell Volume and Pressure Measured Concurrently by Confocal Microscopy and the Cell Pressure Probe. *Plant Physiology*, 125(4), pp.1577–1584.
- Franks, P.J. et al., 2015. Increasing water-use efficiency directly through genetic manipulation of stomatal density. *New Phytologist*, 207(1), pp.188–195.
- Gao, X. et al., 2009. Dynamics of vacuoles and actin filaments in guard cells and their roles in stomatal movement. *Plant, Cell and Environment*, 32(8), pp.1108–1116.

- Gilbert, H.J., Knox, J.P. & Boraston, A.B., 2013. Advances in understanding the molecular basis of plant cell wall polysaccharide recognition by carbohydrate-binding modules. *Current Opinion in Structural Biology*, 23(5), pp.669–677.
- Giovane, A. et al., 2004. Pectin methylesterase inhibitor. *Biochimica et Biophysica Acta (BBA) - Proteins and Proteomics*, 1696(2), pp.245–252.
- Gowik, U. et al., 2004. cis-Regulatory elements for mesophyll-specific gene expression in the C4 plant *Flaveria trinervia*, the promoter of the C4 phosphoenolpyruvate carboxylase gene. *The Plant Cell*, 16(5), pp.1077–1090.
- Griffiths, H. & Helliker, B.R., 2013. Mesophyll conductance: internal insights of leaf carbon exchange. *Plant, Cell & Environment*, 36(4), pp.733–735.
- Guseman, J.M. et al., 2010. Dysregulation of cell-to-cell connectivity and stomatal patterning by loss-of-function mutation in *Arabidopsis* CHORUS (GLUCAN SYNTHASE-LIKE 8). *Development*, 137(10), pp.1731–1741.
- Han, X. et al., 2014. Auxin-callose-mediated plasmodesmal gating is essential for tropic auxin gradient formation and signaling. *Developmental Cell*, 28(2), pp.132–146.
- Hara, K. et al., 2007. The secretory peptide gene EPF1 enforces the stomatal one-cell-spacing rule. *Genes & Development*, 21, pp.1720–1725.
- Harholt, J., Suttangkakul, A. & Scheller, H.V., 2010. Biosynthesis of pectin. *Plant Physiology*, 153(2), pp.384–395.
- Hunt, L. et al., 2017. Formation of the stomatal outer cuticular ledge requires a guard cell wall proline-rich protein. *Plant Physiology*, 174(2), pp.689–699.
- Hunt, L., Bailey, K.J. & Gray, J.E., 2010. The signalling peptide EPFL9 is a positive regulator of stomatal development. *New Phytologist*, 186(3), pp.609–614.
- Hunt, L. & Gray, J.E., 2009. The signaling peptide EPF2 controls asymmetric cell divisions during stomatal development. *Current Biology*, 19(10), pp.864–869.
- Jarvis, M.C., 1998. Intercellular separation forces generated by intracellular pressure. *Plant, Cell and Environment*, 21(12), pp.1307–1310.
- Jarvis, M.C., Briggs, S.P.H. & Knox, J.P., 2003. Intercellular adhesion and cell separation in plants. *Plant, Cell and Environment*, 26(7), pp.977–989.
- Jeffree, C.E., Dale, J.E. & Fry, S.C., 1986. The genesis of intercellular spaces in developing leaves of *Phaseolus vulgaris* L. *Protoplasma*, 132(1–2), pp.90–98.
- Jiang, K. et al., 2012. The ARP2/3 complex mediates guard cell actin reorganization and

- stomatal movement in Arabidopsis. *The Plant Cell*, 24(5), pp.2031–2040.
- Johnson, K.L. et al., 2003. The fasciclin-like arabinogalactan proteins of Arabidopsis. A multigene family of putative cell adhesion molecules. *Plant Physiology*, 133(4), pp.1911–1925.
- Jolie, R.P. et al., 2010. Pectin methylesterase and its proteinaceous inhibitor: a review. *Carbohydrate Research*, 345(18), pp.2583–2595.
- Jones, L. et al., 2003. Cell wall arabinan is essential for guard cell function. *PNAS*, 100(20), pp.11783–11788.
- Jones, L., Seymour, G.B. & Knox, J.P., 1997. Localization of pectic galactan in tomato cell walls using a monoclonal antibody specific to (1->4)-beta-D-galactan. *Plant Physiology*, 113(4), pp.1405–1412.
- Kawase, T. et al., 2015. A direction-selective local-thresholding method, DSLT, in combination with a dye-based method for automated three-dimensional segmentation of cells and airspaces in developing leaves. *The Plant Journal*, 81(2), pp.357–366.
- Kim, M. et al., 1995. Actin filaments in mature guard cells are radially distributed and involved in stomatal movement. *Plant Physiology*, 109(3), pp.1077–1084.
- Kim, S.-J. et al., 2015. CGR2 and CGR3 have critical overlapping roles in pectin methylesterification and plant growth in Arabidopsis thaliana. *The Plant Journal*, 82(2), pp.208–220.
- Knox, J.P., 1992. Cell adhesion, cell separation and plant morphogenesis. *The Plant Journal*, 2(2), pp.137–141.
- Knox, J.P. et al., 1991. Developmentally regulated epitopes of cell surface arabinogalactan proteins and their relation to root tissue pattern formation. *The Plant Journal*, 1(3), pp.317–326.
- Knox, J.P. et al., 1990. Pectin esterification is spatially regulated both within cell walls and between developing tissues of root apices. *Planta*, 181(4), pp.512–21.
- Knox, J.P., 2008. Revealing the structural and functional diversity of plant cell walls. *Current Opinion in Plant Biology*, 11(3), pp.308–313.
- Kolloffel, C. & Linssen, P.W.T., 1984. The formation of intercellular spaces in the cotyledons of developing and germinating pea seeds. *Protoplasma*, 120(1–2), pp.12–19.
- Krupková, E. et al., 2007. The TUMOROUS SHOOT DEVELOPMENT2 gene of Arabidopsis encoding a putative methyltransferase is required for cell adhesion and co-ordinated

- plant development. *The Plant Journal*, 50(4), pp.735–750.
- Lau, O.S. & Bergmann, D.C., 2012. Stomatal development: a plant's perspective on cell polarity, cell fate transitions and intercellular communication. *Development*, 139(20), pp.3683–3692.
- Lehmeier, C. et al., 2017. Cell density and airspace patterning in the leaf can be manipulated to increase leaf photosynthetic capacity. *The Plant Journal*, 92(6), pp.981–994.
- Levesque-tremblay, G. et al., 2015. Tuning of pectin methylesterification: consequences for cell wall biomechanics and development. *Planta*, 242(4), pp.791–811.
- Li, L.-J. et al., 2013. The reorganization of actin filaments is required for vacuolar fusion of guard cells during stomatal opening in Arabidopsis. *Plant, Cell and Environment*, 36(2), pp.484–497.
- Li, S. et al., 2003. The putative Arabidopsis Arp2/3 complex controls leaf cell morphogenesis. *Plant Physiology*, 132(4), pp.2034–2044.
- Li, Y. et al., 2007. Identification of acyltransferases required for cutin biosynthesis and production of cutin with suberin-like monomers. *PNAS*, 104(46), pp.18339–18344.
- Liners, F. et al., 1989. Monoclonal antibodies against pectin: recognition of a conformation induced by calcium. *Plant physiology*, 91(4), pp.1419–1424.
- Lionetti, V. et al., 2007. Overexpression of pectin methylesterase inhibitors in Arabidopsis restricts fungal infection by *Botrytis cinerea*. *Plant Physiology*, 143(4), pp.1871–1880.
- Lionetti, V., Cervone, F. & De Lorenzo, G., 2014. A lower content of de-methylesterified homogalacturonan improves enzymatic cell separation and isolation of mesophyll protoplasts in Arabidopsis. *Phytochemistry*, 112, pp.188–194.
- Manabe, Y. et al., 2011. Loss-of-function mutation of REDUCED WALL ACETYLATION2 in Arabidopsis leads to reduced cell wall acetylation and increased resistance to *Botrytis cinerea*. *Plant Physiology*, 155(3), pp.1068–78.
- Marcus, S.E. et al., 2008. Pectic homogalacturonan masks abundant sets of xyloglucan epitopes in plant cell walls. *BMC Plant Biology*, 8(60).
- Marcus, S.E. et al., 2010. Restricted access of proteins to mannan polysaccharides in intact plant cell walls. *The Plant Journal*, 64(2), pp.191–203.
- Mathur, J. et al., 2003. Mutations in ACTIN-RELATED PROTEINS 2 and 3 affect cell shape development in Arabidopsis. *The Plant Cell*, 15(7), pp.1632–1645.
- Mauseth, J.D. & Fujii, T., 1994. Resin-casting: a method for investigating apoplastic spaces.

- American Journal of Botany*, 81(1), pp.104–110.
- McCartney, L., Marcus, S.E. & Knox, J.P., 2005. Monoclonal antibodies to plant cell wall xylans and arabinoxylans. *The Journal of Histochemistry and Cytochemistry*, 53(4), pp.543–546.
- Meckel, T. et al., 2007. Guard cells elongate: relationship of volume and surface area during stomatal movement. *Biophysical Journal*, 92(3), pp.1072–1080.
- Michelli, F., 2001. Pectin methylesterases: cell wall enzymes with important roles in plant physiology. *Trends in Plant Science*, 6(9), pp.414–419.
- Mohnen, D., 2008. Pectin structure and biosynthesis. *Current Opinion in Plant Biology*, 11(3), pp.266–277.
- Moller, I. et al., 2008. High-throughput screening of monoclonal antibodies against plant cell wall glycans by hierarchical clustering of their carbohydrate microarray binding profiles. *Glycoconjugate Journal*, 25(1), pp.37–48.
- Mouille, G. et al., 2003. Classification and identification of Arabidopsis cell wall mutants using Fourier-Transform InfraRed (FT-IR) microspectroscopy. *The Plant Journal*, 35(3), pp.393–404.
- Mouille, G. et al., 2007. Homogalacturonan synthesis in Arabidopsis thaliana requires a Golgi-localized protein with a putative methyltransferase domain. *The Plant Journal*, 50(4), pp.605–614.
- Mravec, J. et al., 2014. Tracking developmentally regulated post-synthetic processing of homogalacturonan and chitin using reciprocal oligosaccharide probes. *Development*, 141(24), pp.4841–4850.
- Ngouémazong, D.E. et al., 2012. Stiffness of Ca(2+)-pectin gels: combined effects of degree and pattern of methylesterification for various Ca(2+) concentrations. *Carbohydrate Research*, 348, pp.69–76.
- Orfila, C. et al., 2005. QUASIMODO1 is expressed in vascular tissue of Arabidopsis thaliana inflorescence stems, and affects homogalacturonan and xylan biosynthesis. *Planta*, 222(4), pp.613–622.
- Pajor, R. et al., 2013. Seeing space: visualization and quantification of plant leaf structure using X-ray micro-computed tomography. *Journal of Experimental Botany*, 64(2), pp.385–390.
- Palin, R. & Geitmann, A., 2012. The role of pectin in plant morphogenesis. *Bio Systems*, 109(3), pp.397–402.
- Parker, C.C. et al., 2001. Pectin distribution at the surface of potato parenchyma cells in

relation to cell-cell adhesion. *Journal of Agricultural and Food Chemistry*, 49(9), pp.4364–4371.

Paynel, F. et al., 2014. Kiwi fruit PME1 inhibits PME activity, modulates root elongation and induces pollen tube burst in *Arabidopsis thaliana*. *Plant Growth Regulation*, 74(3), pp.285–297.

Peaucelle, A. et al., 2008. *Arabidopsis* phyllotaxis is controlled by the methyl-esterification status of cell-wall pectins. *Current Biology*, 18(24), pp.1943–1948.

Peaucelle, A., Braybrook, S. & Höfte, H., 2012. Cell wall mechanics and growth control in plants: the role of pectins revisited. *Frontiers in Plant Science*, 3(121).

Pedersen, H.L. et al., 2012. Versatile high resolution oligosaccharide microarrays for plant glycobiology and cell wall research. *The Journal of Biological Chemistry*, 287(47), pp.39429–39438.

Pennell, R.I. et al., 1989. A family of abundant plasma membrane-associated glycoproteins related to the arabinogalactan proteins is unique to flowering plants. *The Journal of Cell Biology*, 108(5), pp.1967–1977.

Peterson, R.L., Firminger, M.S. & Dobrindt, A.N.D.L.A., 1975. Nature of the guard cell wall in leaf stomata of three *Ophioglossum* species. *Canadian Journal of Botany*, 53(16), pp.1698–1711.

Raiola, A. et al., 2011. Pectin methylesterase is induced in *Arabidopsis* upon infection and is necessary for a successful colonization by necrotrophic pathogens. *Molecular Plant-Microbe Interactions*, 24(4), pp.432–440.

Ralet, M. et al., 2008. Reduced number of homogalacturonan domains in pectins of an *Arabidopsis* mutant enhances the flexibility of the polymer. *Biomacromolecules*, 9(5), pp.1454–1460.

Raven, J.A., 1996. Into the voids: the distribution, function, development and maintenance of gas spaces in plants. *Annals of botany*, 78(2), pp.137–142.

Röckel, N. et al., 2008. Elaborate spatial patterning of cell-wall PME and PME1 at the pollen tube tip involves PME1 endocytosis, and reflects the distribution of esterified and de-esterified pectins. *The Plant Journal*, 53(1), pp.133–43.

Rowe, M.H. & Bergmann, D.C., 2010. Complex signals for simple cells: the expanding ranks of signals and receptors guiding stomatal development. *Current Opinion in Plant Biology*, 13(5), pp.548–555.

- Savaldi-Goldstein, S., Peto, C. & Chory, J., 2007. The epidermis both drives and restricts plant shoot growth. *Nature*, 446, pp.199–202.
- Scarpella, E., Francis, P. & Berleth, T., 2004. Stage-specific markers define early steps of procambium development in *Arabidopsis* leaves and correlate termination of vein formation with mesophyll differentiation. *Development*, 131(14), pp.3445–3455.
- Scheller, H.V. & Ulvskov, P., 2010. Hemicelluloses. *Annual review of Plant Biology*, 61, pp.263–289.
- Schmid, M. et al., 2005. A gene expression map of *Arabidopsis thaliana* development. *Nature Genetics*, 37(5), pp.501–506.
- Schneider, R. et al., 2016. Cellulose and callose synthesis and organization in focus, what's new? *Current Opinion in Plant Biology*, 34, pp.9–16.
- Seago, J.L. et al., 2005. A re-examination of the root cortex in wetland flowering plants with respect to aerenchyma. *Annals of Botany*, 96(4), pp.565–579.
- Seifert, G.J. & Roberts, K., 2007. The biology of arabinogalactan proteins. *Annual review of plant biology*, 58, pp.137–161.
- Sénéchal, F. et al., 2014. Homogalacturonan-modifying enzymes: structure, expression, and roles in plants. *Journal of Experimental Botany*, 65(18), pp.5125–5160.
- Serna, L., Torres-contreras, J. & Fenoll, C., 2002. Specification of stomatal fate in *Arabidopsis*: evidences for cellular interactions. *New Phytologist*, 153(3), pp.399–404.
- Shimada, T., Sugano, S.S. & Hara-Nishimura, I., 2011. Positive and negative peptide signals control stomatal density. *Cellular and Molecular Life Sciences*, 68(12), pp.2081–2088.
- Showalter, A.M., 1993. Structure and function of plant cell wall proteins. *The Plant Cell*, 5(1), pp.9–23.
- Shtein, I. et al., 2017. Stomatal cell wall composition: distinctive structural patterns associated with different phylogenetic groups. *Annals of Botany*, 119(6), pp.1021–1033.
- Sifton, H.B., 1945. Air-space tissue in plants. *Botanical Review*, 11(2), pp.108–143.
- Smallwood, M. et al., 1996. Immunochemical comparison of membrane-associated and secreted arabinogalactan-proteins in rice and carrot. *Planta*, 198(3), pp.452–459.
- Smallwood, M. et al., 1994. Localization of cell wall proteins in relation to the developmental anatomy of the carrot root apex. *The Plant Journal*, 5(2), pp.237–246.
- Smallwood, M., Martin, H. & Knox, J.P., 1995. An epitope of rice threonine- and hydroxyproline-rich glycoprotein is common to cell wall and hydrophobic plasma-

membrane glycoproteins. *Planta*, 196(3), pp.510–522.

Smith, J.A.C. & Heuer, S., 1981. Determination of the volume of intercellular spaces in leaves and some values for CAM plants. *Annals of Botany*, 48(6), pp.915–917.

Smith, L.G., 2001. Plant cell division: building walls in the right places. *Nature Reviews Molecular Cell Biology*, 2, pp.33–39.

Sterling, J.D. et al., 2006. Functional identification of an Arabidopsis pectin biosynthetic homogalacturonan galacturonosyltransferase. *PNAS*, 103(13), pp.5236–5241.

Sugano, S.S. et al., 2010. Stomagen positively regulates stomatal density in Arabidopsis. *Nature*, 463, pp.241–244.

Teng, N. et al., 2006. Elevated CO₂ induces physiological, biochemical and structural changes in leaves of Arabidopsis thaliana. *New Phytologist*, 172(2), pp.92–103.

Terashima, I. et al., 2011. Leaf functional anatomy in relation to photosynthesis. *Plant Physiology*, 155(1), pp.108–116.

Theroux-Rancourt, G. et al., 2017. The bias of a two-dimensional view: comparing two-dimensional and three-dimensional mesophyll surface area estimates using noninvasive imaging. *New Phytologist*.

Thiele, K. et al., 2009. The timely deposition of callose is essential for cytokinesis in Arabidopsis. *The Plant Journal*, 58(1), pp.13–26.

Tholen, D. et al., 2008. The chloroplast avoidance response decreases internal conductance to CO₂ diffusion in Arabidopsis thaliana leaves. *Plant, Cell & Environment*, 31(11), pp.1688–1700.

Tholen, D. et al., 2012. Variable mesophyll conductance revisited: theoretical background and experimental implications. *Plant, Cell and Environment*, 35(12), pp.2087–2103.

Tilsner, J. et al., 2016. Staying tight: plasmodesmal membrane contact sites and the control of cell-to-cell connectivity in plants. *Annual Review of Plant Biology*, 67, pp.337–364.

Toller, A. et al., 2008. Dual function of Arabidopsis glucan synthase-like genes GSL8 and GSL10 in male gametophyte development and plant growth. *The Plant Journal*, 54(5), pp.911–923.

Tomás, M. et al., 2013. Importance of leaf anatomy in determining mesophyll diffusion conductance to CO₂ across species: quantitative limitations and scaling up by models. *Journal of Experimental Botany*, 64(8), pp.2269–2281.

Tsukaya, H., 2005. Leaf shape: genetic controls and environmental factors. *International*

- Journal of Developmental Biology*, 49, pp.547–555.
- Tsukaya, H., 2006. Mechanism of leaf-shape determination. *Annual Review of Plant Biology*, 57, pp.477–496.
- Vatén, A. et al., 2011. Callose biosynthesis regulates symplastic trafficking during root development. *Developmental Cell*, 21(6), pp.1144–1155.
- Verger, S. et al., 2016. Cell adhesion in plants is under the control of putative O-fucosyltransferases. *Development*, 143, pp.2536–2540.
- Verhertbruggen, Y. et al., 2017. A comparative study of sample preparation for staining and immunodetection of plant cell walls by light microscopy. *Frontiers in Plant Science*, 8(1505).
- Verhertbruggen, Y., Marcus, S.E., Haeger, A., Ordaz-Ortiz, J.J., et al., 2009. An extended set of monoclonal antibodies to pectic homogalacturonan. *Carbohydrate research*, 344(14), pp.1858–1862.
- Verhertbruggen, Y., Marcus, S.E., Haeger, A., Verhoef, R., et al., 2009. Developmental complexity of arabinan polysaccharides and their processing in plant cell walls. *The Plant Journal*, 59(3), pp.413–25.
- De Veylder, L., Beeckman, T. & Inzé, D., 2007. The ins and outs of the plant cell cycle. *Nature Reviews Molecular Cell Biology*, 8, pp.655–665.
- Volkman, D. & Baluska, F., 1999. Actin cytoskeleton in plants: from transport networks to signaling networks. *Microscopy Research and Technique*, 47(2), pp.135–154.
- Wang, M. et al., 2013. A comparative genome analysis of PME and PME1 families reveals the evolution of pectin metabolism in plant cell walls. *PLoS One*, 8(8), p.e72082.
- Wang, M. et al., 1995. The monoclonal antibody JIM19 modulates abscisic acid action in barley aleurone protoplasts. *Planta*, 196(2), pp.271–276.
- Warren, C.R., 2008. Stand aside stomata, another actor deserves centre stage: the forgotten role of the internal conductance to CO₂ transfer. *Journal of Experimental Botany*, 59(7), pp.1475–1487.
- Weraduwege, S.M. et al., 2016. Pectin methylesterification impacts the relationship between photosynthesis and plant growth in *Arabidopsis thaliana*. *Plant Physiology*, 171(3), pp.833–848.
- Willats, W.G. et al., 2001. Modulation of the degree and pattern of methyl-esterification of pectic homogalacturonan in plant cell walls: implications for pectin methyl esterase

- action, matrix properties, and cell adhesion. *The Journal of Biological Chemistry*, 276(22), pp.19404–19413.
- Willats, W.G., Marcus, S.E. & Knox, J.P., 1998. Generation of a monoclonal antibody specific to (1->5)-alpha-L-arabinan. *Carbohydrate Research*, 308(1–2), pp.149–52.
- Willats, W.G.T. et al., 2004. A xylogalacturonan epitope is specifically associated with plant cell detachment. *Planta*, 218(4), pp.673–81.
- Willmer, C.M. & Sexton, R., 1979. Stomata and Plasmodesmata. *Protoplasma*, 100(1), pp.113–124.
- Wolf, S., Mouille, G. & Pelloux, J., 2009. Homogalacturonan methyl-esterification and plant development. *Molecular Plant*, 2(5), pp.851–860.
- Wolf, S., Rausch, T. & Greiner, S., 2009. The N-terminal pro region mediates retention of unprocessed type-I PME in the Golgi apparatus. *The Plant Journal*, 58(3), pp.361–375.
- Woolfenden, H.C. et al., 2017. A computational approach for inferring the cell wall properties that govern guard cell dynamics. *The Plant Journal*, 92(1), pp.5–18.
- Wuyts, N. et al., 2010. High-contrast three-dimensional imaging of the Arabidopsis leaf enables the analysis of cell dimensions in the epidermis and mesophyll. *Plant Methods*, 6(17).
- Yang, J. et al., 2011. Expression analyses of AtAGP17 and AtAGP19, two lysine-rich arabinogalactan proteins, in Arabidopsis. *Plant biology (Stuttgart, Germany)*, 13(3), pp.431–8.
- Yang, W. et al., 2016. Regulation of meristem morphogenesis by cell wall synthases in Arabidopsis. *Current Biology*, 26(11), pp.1404–1415.
- Zablackis, E. et al., 1995. Characterization of the cell-wall polysaccharides of Arabidopsis thaliana leaves. *Plant Physiology*, 107(4), pp.1129–1138.
- Zhao, L. & Sack, F., 1999. Ultrastructure of stomatal development in Arabidopsis (Brassicaceae) leaves. *American Journal of Botany*, 86(7), pp.929–939.
- Zhu, X.-G., Long, S.P. & Ort, D.R., 2010. Improving photosynthetic efficiency for greater yield. *Annual Review of Plant Biology*, 61, pp.235–261.

Appendix 1

Full list of PME genes included in the comparison of expression in leaf tissue in **Figure 3.1**.

AT1G02810.1	AT1G05310.1
AT1G09360.1	AT1G11370.1
AT1G11580.1	AT1G11590.1
AT1G23200.1	AT1G44980.1
AT1G53830.1	AT1G53840.1
AT1G56100.1	AT2G19150.1
AT2G21610.1	AT2G26440.1
AT2G26450.1	AT2G36700.1
AT2G36710.1	AT2G43050.1
AT2G45220.1	AT2G47040.1
AT2G47280.1	AT2G47550.1
AT3G05610.1	AT3G05620.1
AT3G06830.1	AT3G10710.1
AT3G10720.1	AT3G14300.1
AT3G14310.1	AT3G17060.1
AT3G17140.1	AT3G24130.1
AT3G27980.1	AT3G29090.1
AT3G42160.1	AT3G43270.1
AT3G47400.1	AT3G49220.1
AT3G59010.1	AT3G60730.1
AT3G62170.1	AT4G00190.1
AT4G02300.1	AT4G02320.1
AT4G02330.1	AT4G03930.1
AT4G15980.1	AT4G33220.1
AT4G33230.1	AT5G04960.1
AT5G04970.1	AT5G07410.1
AT5G07420.1	AT5G07430.1
AT5G09760.1	AT5G18990.1
AT5G19730.1	AT5G20860.1
AT5G27870.1	AT5G47500.1
AT5G49180.1	AT5G51490.1
AT5G51500.1	AT5G53370.1
AT5G55590.1	AT5G64640.1